

AD A138198

AFWAL-TR-83-1110

DIODE PUMPED FIBER LASER



Edward L. Ginzton Laboratory
Stanford University
Stanford, California 94305

July 1983

Interim Report for Period April 1982 - May 1983

Approved for public release; distribution unlimited.

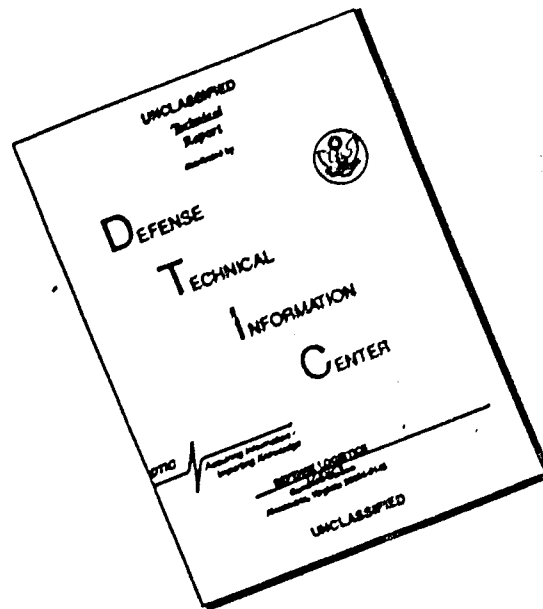
DTIC FILE COPY

AVIONICS LABORATORY
AIR FORCE WRIGHT AERONAUTICAL LABORATORIES
AIR FORCE SYSTEMS COMMAND
WRIGHT-PATTERSON AIR FORCE BASE, OHIO 45433

DTIC
ELECTE
S FEB 23 1984
E

84 02 21 118

DISCLAIMER NOTICE



THIS DOCUMENT IS BEST QUALITY AVAILABLE. THE COPY FURNISHED TO DTIC CONTAINED A SIGNIFICANT NUMBER OF PAGES WHICH DO NOT REPRODUCE LEGIBLY.

NOTICE

When Government drawings, specifications, or other data are used for any purpose other than in connection with a definitely related Government procurement operation, the United States Government thereby incurs no responsibility nor any obligation whatsoever; and the fact that the government may have formulated, furnished, or in any way supplied the said drawings, specifications, or other data, is not to be regarded by implication or otherwise as in any manner licensing the holder or any other person or corporation, or conveying any rights or permission to manufacture use, or sell any patented invention that may in any way be related thereto.

This report has been reviewed by the Office of Public Affairs (ASD/PA) and is releasable to the National Technical Information Service (NTIS). At NTIS, it will be available to the general public, including foreign nations.

This technical report has been reviewed and is approved for publication.

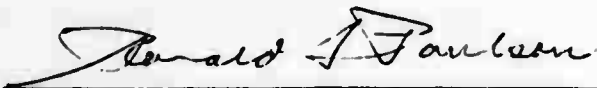


DR. W. K. SCHUEBEL, Project Engineer
E-O Sources Group
Electro-Optics Technology Branch



JAMES M. HEITMAN, Chief
E-O Sources Group
Electro-Optics Technology Branch

FOR THE COMMANDER



DR. RONALD F. PAULSON, Chief
Electro-Optics Technology Branch
Electronic Technology Division

"If your address has changed, if you wish to be removed from our mailing list, or if the addressee is no longer employed by your organization please notify AFWAL/AADO, W-PAFB, OH 45433 to help us maintain a current mailing list".

Copies of this report should not be returned unless return is required by security considerations, contractual obligations, or notice on a specific document.

REPORT DOCUMENTATION PAGE		READ INSTRUCTIONS BEFORE COMPLETING FORM
1. REPORT NUMBER AFWAL-TR-83-1110	2. GOVT ACCESSION NO. AD-A138 198	3. RECIPIENT'S CATALOG NUMBER
4. TITLE (and Subtitle) DIODE PUMPED FIBER LASER		5. TYPE OF REPORT & PERIOD COVERED Interim Report April 1982 - May 1983
		6. PERFORMING ORG. REPORT NUMBER G. L. 3582
7. AUTHOR(s) Michel J. F. Digonnet and H. J. Shaw		8. CONTRACT OR GRANT NUMBER(s) F33615-82-C-1749
9. PERFORMING ORGANIZATION NAME AND ADDRESS Edward L. Ginzton Laboratory Stanford University Stanford, CA 94305		10. PROGRAM ELEMENT, PROJECT, TASK AREA & WORK UNIT NUMBERS 2001-01-99
11. CONTROLLING OFFICE NAME AND ADDRESS Avionics Laboratory (AFWAL-AADO) AF Wright Aeronautical Laboratories Wright-Patterson AFB, OH 45433		12. REPORT DATE July 1983
		13. NUMBER OF PAGES 214
14. MONITORING AGENCY NAME & ADDRESS (if different from Controlling Office)		15. SECURITY CLASS. (of this report) Unclassified
		15a. DECLASSIFICATION/DOWNGRADING SCHEDULE
16. DISTRIBUTION STATEMENT (of this Report) Approved for public release; distribution unlimited.		
17. DISTRIBUTION STATEMENT (of the abstract entered in Block 20, if different from Report)		
18. SUPPLEMENTARY NOTES		
19. KEY WORDS (Continue on reverse side if necessary and identify by block number) Laser Source LD-to-Optical Fiber Coupling Nd:YAG Single Crystal Optical Fiber Optical Waveguides Optical Fiber Laser Crystal Fiber Growth Laser Diodes neodymium Single-Mode Fiber Systems		
20. ABSTRACT (Continue on reverse side if necessary and identify by block number) The objective of this program was the study and exploratory development of a miniature solid state laser source as a potential signal source in a variety of fiber optic sensors and systems. The specific source to be studied was composed of a single-crystal Nd-YAG optical fiber end-pumped with a single semiconductor laser diode. This program called for goals of an 8 mm maximum length and 80 μ m maximum diameter Nd:YAG fiber laser, with an anticipated 5 mW cw output in a single transverse mode at 1.064 μ m. The fiber lasers under		

20. Abstract (continued)

investigation consisted of short Nd:YAG fibers with carefully polished ends placed in an external optical cavity made of two miniature flat mirrors, and end-pumped either at 514.5 nm (argon-ion laser) or near 818 nm (laser diode). Coherent laser emission was observed in a variety of fibers, with diameters and lengths ranging from 78 to 250 μm , and 4 to 12 mm, respectively. With a 514.5 nm pump, a maximum output power of nearly 10 mw was observed (~31% energy conversion efficiency) with a threshold of oscillation of only a few mW. With an 818 nm pump source, efficient coupling to crystal fibers was obtained (up to 100% in 100 μm fibers) and threshold of oscillations as low as 3.9 mw observed. The maximum observed power, limited by the low available LD power and residual fiber loss, was then approximately 200 μW . The fiber laser output was in all cases linearly polarized, single transverse (fundamental) mode, and showed good short and long term stability. An investigation of the source of residual loss observed in fiber laser cavities showed that the main loss mechanism is signal aperturing by the fiber, whose surface defects scatter small amounts of the signal into higher order modes. This effect resulted also in a high signal mode confinement, a large gain per unit pump power, and led to the first demonstration of an optical guiding effect in this type of fiber lasers.

FOREWORD

This twelve-month investigation of laser diode-pumped fiber lasers was supported by the United States Air Force, AFSC, Aeronautical Systems Division, Wright-Patterson AFB, under contract F33615-82-C-1749 and was technically monitored by Dr. Wolfgang K. Schuebel of the Avionics Laboratory (AFWAL/AADO) under Project 2001 01 99.

The authors are indebted to C. Gaeta for his work on laser cavity design and laser diode measurements, and for his contribution to the development of the theoretical fiber laser model. They would like to thank D. O'Meara for the growth of the Nd:YAG single-crystal fibers used in this work, and for his constant efforts toward improving their quality. They also thank G. Kotler and J. Vrhel for the processing and polishing of these fibers. They would like to acknowledge the Xerox Palo Alto Research Center for supplying experimental laser diodes without cost, and for their help with the evaluation of their laser diodes. Finally they would like to express their thanks to J. Stone of the Bell Telephone Laboratories for his helpful suggestions.

Accession For	
NTIS GRA&I	<input checked="" type="checkbox"/>
DTIC TAB	<input type="checkbox"/>
Unannounced	<input type="checkbox"/>
Justification	
By	
Distribution/	
Availability Codes	
Dist	Avail and/or Special
A-1	



TABLE OF CONTENTS

<u>SECTION</u>	<u>PAGE</u>
I. INTRODUCTION.....	1
A. BACKGROUND.....	1
B. OBJECTIVES.....	2
C. SUMMARY OF RESULTS.....	3
D. GENERAL PLAN.....	5
II. Nd:YAG FIBER PREPARATION.....	7
A. FIBER GROWTH.....	7
B. PHYSICAL PROPERTIES OF Nd:YAG FIBERS.....	12
C. FIBER PROCESSING.....	15
1. End-Polishing.....	15
2. Cladding Single Crystal Fibers.....	18
III. THEORY OF MODAL OVERLAPS IN LASERS.....	25
A. INTRODUCTION.....	25
B. GENERAL FORMALISM.....	26
C. FREE-SPACE LASERS.....	35
D. FIBER LASERS.....	43
1. Fiber Laser Configuration.....	43
2. $F_{\nu\mu nm}$ Coefficients	44
3. Threshold.....	55
4. Slope Efficiency.....	59
5. Fiber Laser Design.....	62
6. Summary.....	63

<u>SECTION</u>	<u>PAGE</u>
IV. ARGON-LASER PUMPED Nd:YAG LASERS.....	65
A. MINIATURE BULK LASERS.....	65
1. Laser Configuration.....	65
2. Laser Characterization.....	67
(a) Nd:YAG Crystals.....	67
(b) Output Measurements.....	69
(c) Transverse Mode Structure.....	77
(d) Mode Overlap Measurements.....	78
B. FIBER LASERS.....	83
1. Experimental Arrangement.....	83
2. 100 μ m Diameter Fiber Lasers.....	87
3. Short Fiber Lasers.....	104
4. Guided Fiber Lasers.....	114
V. LASER-DIODE-PUMPED FIBER LASERS.....	117
A. LD CHARACTERIZATION.....	119
1. Hitachi Laser Diodes.....	119
2. Xerox Laser Diodes.....	121
B. LD-TO-OPTICAL FIBER COUPLING.....	123
1. LD #H-2.....	124
2. LD #X-2.....	130
C. LD-PUMPED FIBER LASERS.....	132
1. Fiber Lasers.....	132
2. Comparison between LD and Argon Laser Pumping..	137
3. LD-Pumped Bulk Nd:YAG Lasers.....	141
4. Discussion.....	144
5. LD-Array-Pumped Lasers.....	146

<u>SECTION</u>	<u>PAGE</u>
VI. FIBER LASER LOSS ANALYSIS.....	149
A. OPTICS-RELATED LOSS MECHANISMS.....	150
1. End-Face Scattering.....	150
2. Mirror Defects.....	150
3. Cavity Alignment.....	151
4. Mode Coupling.....	152
B. MATERIAL-RELATED LOSS MECHANISMS.....	153
1. Solarization.....	153
2. Pump Quantum Efficiency.....	154
3. Nd: Concentration.....	154
(a) Mass-Spectroscopy Analysis.....	155
(b) Fluorescence Lifetime.....	155
(c) Fluorescence Spectra.....	160
(d) Discussion.....	162
C. FIBER-RELATED LOSS MECHANISMS.....	163
1. Evidence of Aperturing.....	163
2. Fiber Scattering.....	166
D. SUMMARY.....	168
VII. CONCLUSIONS.....	169
APPENDICES:	
A. EXPANSION OF THE OVERLAP INTEGRAL $J_1(S_1)$	171
B. CALCULATION OF GAUSSIAN MODE SPATIAL OVERLAP INTEGRALS...	173
C. LP_{nm} FIBER MODES.....	175
D. EFFECT OF A RELATIVE PUMP OFFSET IN FIBER LASERS.....	179
E. GUIDING MECHANISMS IN FIBER LASERS.....	188

<u>SECTION</u>	<u>PAGE</u>
APPENDICES (continued)	
F. EFFECT OF PUMP ASTIGMATISM ON LASER CHARACTERISTICS.....	197
REFERENCES.....	200

LIST OF ILLUSTRATIONS

FIGURE		PAGE
1	Schematic of the Floating-Zone Technique used to grow Single-Crystal Nd:YAG Fibers	8
2	Single Crystal Fiber Pulling System	10
3	Nd:YAG Fiber End-Face Polishing Fixture	17
4	(a) Photograph of Polished Fiber Ends (Array #16). (b) Photograph of the Polished End of a Nd:YAG Fiber Clad with SF-57 Glass (Array #8)	19
5	Schematic of the Gaussian Pump Beam inside the Laser Crystal	36
6	Dependence of the Effective Pump Radius on Actual Pump Waist Radius	40
7	Dependence of the Slope Efficiency on the Pump Waist Radius for a Nd:YAG Bulk Laser pumped at $\lambda = 514.5 \text{ nm}$ ($T_1 = 1\%$, $\delta_0 = 5\%$, $W_0 = 25 \text{ }\mu\text{m}$); (a) Exact Solution; (b) Approximate Solution given by Eq. 25	42
8	Variation of a few $F_{\nu n m}$ Coefficients with the Fiber V-Number (at the Signal Frequency)	46
9	Evaluation of Overlap Coefficients $F_{01 n m}$ for Increasing Value of the Modal Number m	50
10	Fractional Modal Energy Contained between $r = 0$ and $r = r_0$ as a Function of r_0 for a few LP-Modes	51
11	Evolution of a few Overlap Coefficients $F_{n m n m}$ for Increasing Values of the Modal Number m	53
12	Dependence of the Fiber Laser Threshold on Core Radius in the LP_{01}/LP_{01} Mode Configuration	58
13	Exact (Solid Curves) and Approximate (Dashed Curves) Theoretical Dependence of the Output Power of a Fiber Laser on Absorbed Pump Power for Increasing Round Trip Cavity Loss. Signal and Pump Modes are LP_{01} , Fiber V-Number is 40	60
14	Slope Efficiency Dependence on the Fiber V-Number for an LP_{01} Signal Mode and Various Pump Modes	61

FIGURE		PAGE
15	Schematic of the 514.5 nm End-Pumped Miniature Nd:YAG Laser Experimental Arrangement	66
16	Miniature Nd:YAG Laser Cavity	68
17	Laser Output Power Versus Absorbed Pump Power in Crystal #3	71
18	Laser Output Power Versus Absorbed Pump Power in Crystal #1	72
19	Photographs of a Few of the Transverse Modes Observed in Miniature Nd:YAG Lasers (Crystal #3)	79
20	Experimental Verification of the Dependence of the Threshold of a Miniature Nd:YAG Laser on the Pump Waist Radius (Crystal #3). Theoretical Curve was fitted with $\delta_0 = .026$ and $W_s = 64.5 \mu\text{m}$	80
21	Experimental Verification of the Dependence of the Slope Efficiency of a Miniature Nd:YAG Laser on the Pump Waist Radius (Crystal #3). The fitting Parameters are the same as in Figure 20	82
22	Schematic of the Fiber Laser Cavity	86
23	Output Power Versus Absorbed Pump Power for Fiber #1-4 ($T_1 = 1\%$)	88
24	Output Power versus Absorbed Pump Power for Fiber #1-4 ($T_1 = 5\%$)	89
25	(a) Far-Field Profile of the Fundamental Pump Mode (.5145 μm , Fiber #1-4). (b) Far Field Profile of the Fiber Signal Output Mode (1.064 μm , Fiber #1-4)	93
26	(a) Near-Field Profile of the Fundamental Pump Mode (.5145 μm , Fiber #1-4). (b) Near-Field Profile of the Fiber Signal Output Mode (1.064 μm , Fiber #1-4)	94
27	Threshold versus Loss Coefficient in Fiber Lasers of Array #1	99
28	Measured Threshold versus Measured Fiber Diameter Fluctuations for 10 Fiber Lasers (Array #1)	100
29	Output Power Curve of Fiber Laser #2-3	107
30	(a) Interferogram of Nd:YAG Fiber #5-9. (b) Interferogram of Nd:YAG Fiber #5-11	112

FIGURE		PAGE
31	Absorption Spectrum of ~1% Doped Nd:YAG in the 810 nm Region, measured on a Perkin-Elmer Model 330 Spectrophotometer (Resolution ~.7 Å). Sample Thickness is 6 mm. Full Vertical Scale represents ~100% Absorption	118
32	Characteristics of Laser Diode HLP-1400 provided by Manufacturer	120
33	Power versus Current Curve for High-Power Laser Diode Array #X-2 (from Xerox Research Center, Palo Alto, California)	122
34	Absolute and Relative Power carried by Collimated Laser Diode Beam as a Function of the Objective Numerical Aperture (Hitachi HLP 1400 Diode)	127
35	Experimental Arrangement used to Pump Nd:YAG Fiber Lasers with a Laser Diode and/or an Argon-Ion Laser	134
36	Output Power Curve of Fiber Laser #2-11 pumped with a Single cw Laser Diode	136
37	Same as Figure 36, after Calibration	138
38	Output Power Curves of a Miniature Nd:YAG Laser (Crystal #4) pumped with a Single cw Laser Diode	143
39	(a) Upper Trace: Pump Pulse fed into Single Crystal Fiber. Lower Trace: Fiber Fluorescence. Horizontal Scale: 1 msec/div. (b) Typical Decay of the Fluorescence emitted by a Fiber after Pump Turn-off (Fiber #3-4). Horizontal Scale: 100 msec/div	156
40	Nd-Concentration Measurements for In-House grown Nd:YAG Fibers	159
41	Fluorescence Spectra of Nd:YAG Fiber #2-7 excited with ~40 mw at 514.5 nm. (a) $4F_{3/2} \rightarrow 4I_{9/2}$ Transition ($\lambda \sim 900$ nm), (b) $4F_{3/2} \rightarrow 4I_{11/2}$ Transition ($\lambda \sim 1060$ nm)	161
42	Experimental Evidence of the Cavity Loss Increase with Fiber Aspect Ratio in 514.5 nm pumped Fiber Lasers	165
C.1	Intensity Radial Profiles of a Few LP-Modes (Far from Cut-Off)	178

D.1	Effect of an Offset or a Tilt between Pump and Signal Modes on the Laser Threshold	182
D.2	Effect of an Offset or a Tilt between Pump and Signal Beam on the Laser Slope Efficiency	185
D.3	Effect of an Offset or Tilt between Pump and Signal Beam on the Measured Cavity Round-Trip Loss	186
E.1	Normalized Gain Profile in a Nd:YAG Fiber Laser at increasing Levels of Saturation (η = Number of Times above Threshold). Fiber Parameters are $a = 50 \mu\text{m}$, $\eta_1 - \eta_2 = 0.005$ (LP_{01} Pump and Signal Modes)	190
E.2	Plots of the Real and Imaginary Parts of the Susceptibility $\tilde{\chi}(\nu)$ of a Gain Medium (Unsaturated)	192

LIST OF TABLES

TABLE		PAGE
1	List of Single Crystal Fibers Grown to Date (CMR)	13
2	Physical and Optical Properties of Nd:YAG	27
3	Asymptotic Values ($V \rightarrow \infty$) of the Modal Overlaps $F_{\nu\mu nm}$ for a Few Low Order Signal and Pump Modes	48
4	Nd:YAG Crystals Data	69
5	Summary of Laser Performance for Two Nd:YAG Crystals pumped at $\lambda_p = .5145 \mu m$	74
6	List of Fiber Arrays and Characteristics as Available at the Moment	85
7	Measured Data for Fiber Lasers of Array #1	97
8	Characteristics of Fibers in Array #7	102
9	Mode Measurements in Fiber Laser #2-5	109
10	Diameter Data of Fiber Array #4	116
11	Recollimation Measurement Data for Laser Diode #H-2 (Hitachi HLP-1400)	126
12	Coupling Data for Laser Diode #X-2	131
13	Measured Parameters of Bulk and Fiber Nd:YAG Lasers ($\lambda_p \sim 820 \text{ nm}$)	145
14	Summary of Fluorescence Lifetime Measurement Results	158
E-i	Magnitude of the Index Gradient Provided by the Guiding Mechanisms Present in a Hot Fiber Laser Cavity ($P_p = 300 \text{ mW}$, $a = 50 \mu m$, $l = 8 \text{ mm}$)	196

A. BACKGROUND

The development of a variety of single-mode fiber systems has been the subject of much effort during the last few years. These systems include sensors for the detection of various environmental parameters such as rotation (Reference 1), pressure or acoustic waves (Reference 2), electric or magnetic currents, as well as high-speed signal processors, such as notch and bandpass filters, transient memories and delay lines (Reference 3). Passive forms of these optical systems have been successfully demonstrated in our own as well as other laboratories, and await the development of active components for improved performance.

Of all active devices, miniature lasers compatible with the round optical fiber geometry are among the most strongly needed. The only miniature sources currently available are laser diodes, but they present several intrinsic problems, the most serious one being their poor optical coupling to single mode fibers resulting from their strong beam astigmatism. As an alternative, fiber lasers combine the advantages of potentially high energy confinement and of a geometry perfectly matched to that of optical fibers.

A class of active fibers which has received much attention in the last few years is single crystal fibers. As waveguides they allow one to transmit energy at higher density over much longer distances than is the case with their traditional bulk optic counterparts, which should yield tremendous improvements in the efficiency of active and nonlinear optical devices. For reasons of crystal growth dynamics associated with the small crystal diameters, it may be possible to grow in fiber form the most perfect crystals

yet made, including crystals which cannot be usefully grown in bulk or epitaxial form. Crystal fibers can also be grown much faster than bulk crystals, so that a large variety of fiber crystals can be grown and characterized on a much shorter time scale than allowed by more conventional growth methods. These properties make single crystal fibers particularly attractive for a number of applications in the fields of optics and acoustics.

Single crystal fibers were first grown at the Bell Telephone Laboratories using a laser-heating pedestal growth technique (Reference 4). Nd:YAG fibers grown by this method were pumped with LED's and made into cw lasers (References 4 and 5). More recently a growth station operating on the same principle was developed in the Center for Materials Research (CMR) at Stanford University, and a large number of materials were grown in a single crystal fiber form. Under a previous program, fibers of Nd:YAG grown at CMR were made into optical pulse amplifiers with as much as 5.3 dB of gain (Reference 6). For obvious reasons it was interesting to pursue this work and attempt developing Nd:YAG fiber oscillators.

B. OBJECTIVE

The objective of this program was to study miniature solid-state laser sources composed of a single-crystal Nd:YAG fiber (active medium) and of a semiconductor injection laser diode (pump). The use of laser diode pumps was proposed to achieve higher pump-to-fiber coupling efficiencies than obtained by other authors with LED's (Reference 5). This program involved the growth, processing, mirror coating and characterization of high quality single crystal fibers of various dimensions, the demonstration of a practical arrangement for efficient optical pumping of fiber lasers, and the evaluation of the resulting fiber lasers. The program goal was the demonstration of a compact, LD-pumped

C. SUMMARY OF RESULTS

The results of the work performed under this contract and described in this report may be summarized as follows:

1. For the purpose of laser research a large number of Nd:YAG fibers were grown, with diameters ranging from 15 μm to 250 μm . Under another program (Reference 7), major improvements were performed on the CMR growth station, which yielded higher quality fibers and better diameter control.
2. A new type of holder was designed to receive the fibers. It provides easy handling and mechanical protection of the fibers.
3. Using in-house facilities, it was shown that fibers mounted in this fashion could be routinely polished to a flatness of $\lambda/4$ or better over the entire cross-section of the fibers.
4. A theoretical model of end-pumped lasers was developed. It describes the output of a laser in terms of its threshold and energy conversion efficiency, and expresses these two parameters as a function of pump and signal mode spatial overlap. By introducing the concept of filling factor, the effect of the modal structures of the interacting waves on the laser threshold was simplified to a single additional parameter.
5. Applied to the case of guided fiber lasers, this theory provides a simple and clear description of the dependence of the laser output characteristic on the pump and signal modes and on the fiber parameters (V-number). It also predicts that a fiber laser has an optimum energy conversion efficiency for a V in the range of 5-25.

Nd:YAG fibers end-pumped at 514.5 nm and placed in an external cavity made of miniature mirrors. Thresholds as low as 2.6 mW were observed in $\sim 100 \mu\text{m}$ diameter fibers, corresponding to round-trip losses of only a few percent.

7. In the lowest loss fiber lasers ($\sim 230 \mu\text{m}$ in diameter) a maximum slope efficiency of 31% and a maximum output power of 9 mW were measured.

8. Similarly, laser action was successfully demonstrated in Nd:YAG fibers end-pumped with a single cw laser diode emitting near 820 nm. Again the output was linearly polarized and single-mode. Thresholds as low as 3.9 mW were obtained.

9. The finite transverse size of the gain medium was found to induce a strong signal mode confinement and actual guiding in most cases. This resulted in a single transverse mode laser output (TEM_{00}). All lasers also showed the same degree of polarization as the pump beam.

10. All fibers were uncooled and yet exhibited a good short term stability. To the best of our knowledge this result constitutes the first demonstration of uncooled Nd:YAG devices at such relatively high output power.

11. Under similar conditions, miniature crystals of Nd:YAG were tested in a laser environment, both with 514.5 nm and 820 nm pump beams. Results showed excellent laser behavior and were conveniently used throughout this work for comparison to fiber laser behavior.

12. Measurements on fiber lasers with diameters ranging from 80 to $230 \mu\text{m}$ were in excellent agreement with our theoretical model. They were consistent with a value of the material stimulated emission cross-section of $\sigma = 2.3 \times 10^{-19} \text{ cm}^2$.

13. Comparison of bulk and fiber laser operations indicated that fiber lasers exhibited a somewhat higher cavity loss, as well as a higher gain per unit power .

14. No measurable differences were found in the spectroscopic parameters of bulk crystals versus fibers of Nd:YAG.

15. An extensive loss mechanism analysis was performed which clearly demonstrated that these two differences (see item 13) were due to signal aperturing by the fiber. Aperturing was found to be caused by residual crystal bulk defects in larger diameter fibers, and surface scattering in smaller diameter fibers. This provides additional proof that these are actually the first guided Nd:YAG fiber lasers demonstrated so far.

16. Work was initiated on the characterization and use as a pump source of a high-power laser diode array with an output power of ~ 140 mW at ~ 820 nm. When implemented in Nd:YAG fiber lasers it should yield several tens of milliwatts of $1.064 \mu\text{m}$ output power.

17. Future work will concentrate on fiber quality and loss reduction. The recent completion of a new fiber growth station in the Ginzton Laboratory should speed up this process.

D. GENERAL PLAN

The research activities under this program have followed several directions, and for the sake of clarity this report addresses them in six sections numbered II through VII. The content of these sections is as follows:

Section II. Nd:YAG fiber preparation and characterization.

Section III. Theory of modal overlaps in fiber lasers.

- Section IV. Experimental work on 814.9 nm pumped bulk and fiber Nd:YAG lasers.
- Section V. Experimental work on 820 nm pumped bulk and fiber Nd:YAG lasers.
- Section VI. Experimental analysis of residual loss in fiber laser cavities.
- Section VII. Conclusions of this work and future directions.

SECTION II

Nd:YAG FIBER PREPARATION

In this section we describe the growth process of the Nd:YAG single crystal fibers used in the present work. The growth station is described in some detail, together with the major improvements that it underwent since this program began. As an introduction to the development of fiber lasers we also summarize the physical properties of the Nd:YAG fibers grown with this station. The last section is devoted to the work done under this as well as other programs on the subject of fiber processing, which includes fiber end preparation and fiber cladding.

A. FIBER GROWTH

The single crystal fibers used in this work were grown at the Center for Materials Research (CMR) at Stanford University using a growth station developed two years ago (References 4,8). It implements the so-called floating-zone pedestal growth technique, related to the more widely known Czochralski method. The crystal fiber is grown from a melt produced by a high-power cw CO₂ laser (Reference 8). In the configuration of the CMR growth station, the laser beam is split into two beams which are redirected and focused from opposite directions on a small rod of material to produce a molten bead held by surface tension (Figure 1) (Reference 8). A platinum wire, or a seed crystal, is dipped into the melt, and the fiber is grown by translating the parent rod and seed upward with different velocities (V_s and V_f , respectively). The diameter of the new crystal d_f (fiber) is determined by mass conservation according to $d_f = (V_s/V_f)^{1/2} d_s$, where d_s is the source rod diameter. Since the source rod diameter is on the order of 0.5 - 1.0 mm, while typical diameter reductions are in the range of 2 - 4:1, a

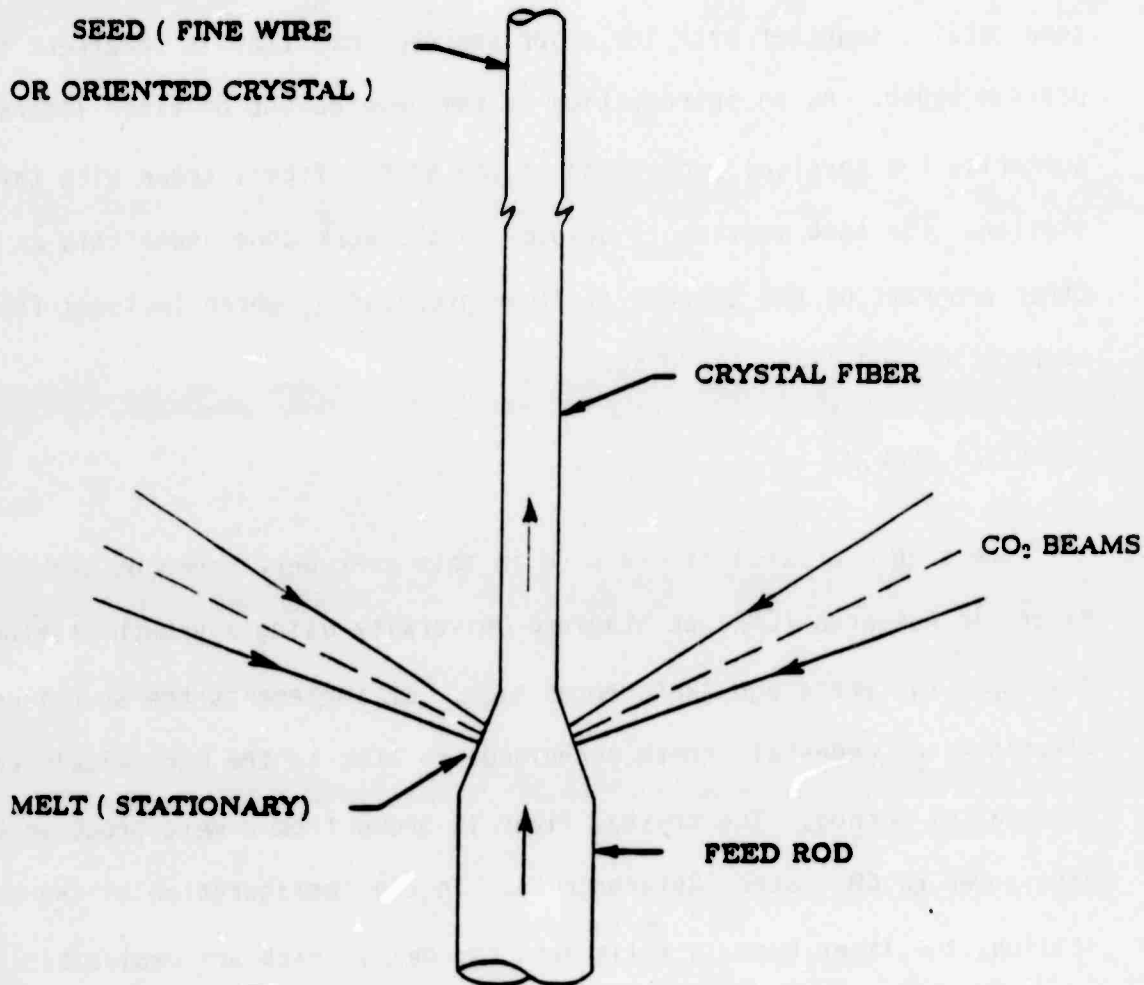


Figure 1--Schematic of the Floating-Zone Technique used to grow Single-Crystal Nd:YAG Fibers.

few iterations of the above growth process are required to achieve fiber diameters in the 10-100 micron range of interest for optical device applications. In iterative steps the previously grown fiber is used as a parent to grow the next generation fiber.

A schematic of the optical circuit and associated systems is shown in Figure 2. The laser output power is monitored with a thermal power meter and is stabilized by feedback to the tube current based on the monitor signal. A 50/50 beam splitter divides the beam into two parts which are delivered through a series of mirrors to two focusing lenses ($f = 12.5$ cm) arranged diametrically opposed to one another to illuminate the melt zone with the desired bilateral symmetry. The minimum focal spot size produced is $250\text{ }\mu\text{m}$.

The source rod and the fiber are held by means of miniature three-jaw-chucks connected to independently driven lead screws. Motor speed control is based on a feedback system with approximately 1% stability. Both chucks are provided with variable rate rotation about their axes. Rotating either the feed or the fiber during the growth process helps homogenization of the heat distribution in the melt when growing from large parent rods (1 mm or more).

The laser-heated pedestal growth presents several features that make it unique in the single crystal growth technology. The use of tightly focused laser beams makes possible very high temperature gradients and unusually high growth rates, on the order of millimeters per minute. Because of the small molten zone involved, very rapid heating and cooling can be achieved, and

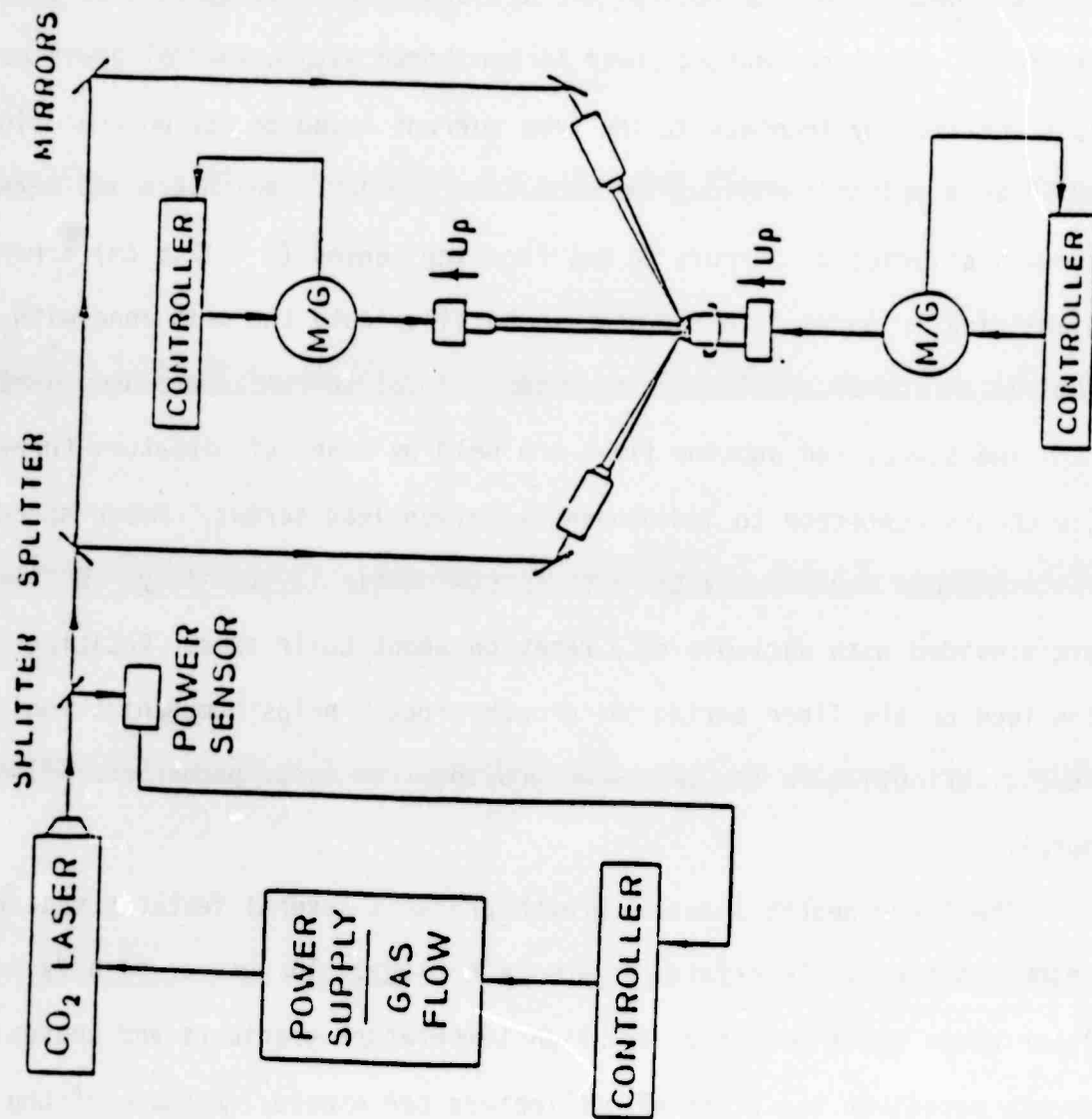


Figure 2--Single Crystal Fiber Pulling System.

uniform dopant concentrations are possible. Very high temperatures can be reached at relatively low laser power. Another advantage is that the quantity of starting material required is minimal, and sample preparation can be very quick. The parent material can be in any solid form, including polycrystalline or amorphous forms, which makes possible the synthetization of new crystals. Finally, this process does not require the use of a container, and contamination problems are reduced. On the other hand, one of the major limitations of this station is that in its present form it can only be used to grow congruently-melting materials, i.e., materials whose liquid and solid phases are in equilibrium with identical stoichiometric compositions. However, this limitation is relatively minor as a large number of optically active and nonlinear materials, such as refractory oxides, and in particular Nd:YAG, do melt congruently. Also, it may be possible to broaden this spectrum of materials by implementing alternative edge-defined growth methods, such as a capillary method.

Several major improvements, performed under another program (Reference 7), were implemented in the CMR growth station during the course of the present work. Motors and motor gear driving the feed and pull mechanisms were upgraded for a larger range of operation and better performance. Also, ambient laboratory air currents, which were identified as a major source of instability during the growth of smaller diameter fibers, were eliminated by enclosing the growth area in an air-tight chamber. The chamber is equipped with two lateral ZnSe windows for the transmission of the CO₂ beams, and with glass windows for visual observation and control of the fiber during growth with a variable magnification binocular microscope. The chamber also offers the possibility of growing fibers under a controlled atmosphere, such as

argon, oxygen or vacuum, depending on the requirements of the material grown.

A commercial diameter measurement unit was also acquired for control of the fiber diameter as it is being grown. It provides measurements of the diameter of the fiber, molten zone and source rod at different points to a precision of 0.1 - 0.5 μm depending on operating conditions. When interfaced with a newly acquired computer, this unit will feed error signals back to the laser power supply and/or to the motor drives to automatically compensate for any departure of the fiber diameter from a pre-selected value.

A major improvement in crystal fiber diameter control has been observed by implementing a variable CO_2 laser power attenuator in the growth station. The attenuator is particularly useful when growing smaller diameter fibers ($< 200 \mu\text{m}$), which normally requires operation of the laser at low power with a resulting increase in the laser output fluctuations. This addition also significantly improved growth stability while reducing the frequency of adjustments required during the growth of several inch long fibers.

Finally, fiber diameter control was further improved by using 500 μm ground rods as a source material (instead of 1 mm square rods) prepared in-house with a newly acquired centerless-grinder.

B. PHYSICAL PROPERTIES OF Nd:YAG FIBERS

To illustrate the potential of this crystal growth method, we have listed in TABLE 1 some of the most important crystals grown to date with CMR facilities together with the fiber characteristics (diameter, crystal orientation) and their potential applications. LiNbO_3 was grown in a variety of diameters and crystal orientations. It has many applications which involve its excellent electro-optic, nonlinear and ferroelectric properties. Single

TABLE 1
LIST OF SINGLE CRYSTAL FIBERS GROWN TO DATE (CMR)

MATERIAL	ORIENTATION	DIAMETER	APPLICATIONS
Nd:YAG	(111),(100)	600-15 μ m	Laser, Amplifier
Sapphire	a,c	600-50 μ m	Combustion Analysis
LiNbO ₃	a,c	800-150 μ m	Electro-Optic Acousto-Optic
Gd ₂ (MoO ₄) ₃	(110)	600-200 μ m	Ferroelastic
CaSc ₂ O ₄	a,c	600-100 μ m	Model
SrSc ₂ O ₄		600 μ m	Model
YIG		600-100 μ m	Isolator
Y ₂ O ₃ :EU	c	600-800 μ m	
Li ₂ GeO ₃	a,c	600-100 μ m	Raman Device
Nd:CaSc ₂ O ₄	c	600 μ m	Laser
BaF ₂ /CaF ₂	a,c	600-200 μ m	IR
AgBr	a	750 μ m	IR guiding
KRS-5		750 μ m	IR guiding

phase fibers of GdO were also grown successfully, and are currently being characterized for the development of acoustic devices. Calcium and strontium scandates were also grown from hot-pressed rods. By doping CaSc_2O_4 with ~ 1% of neodymium with a novel and simple technique (Reference 9), good quality, ~ 400 μm diameter crystals were obtained, to the best of our knowledge for the first time in this country. Other crystal fibers grown include YIG with potential applications as optical isolators and circulators, $\text{Eu:Y}_2\text{O}_3$, Li_2GeO_3 (LGO) for use as a Raman optical frequency shifter, and composite materials such as $\text{BaF}_2/\text{CaF}_2$ for the study of the morphological control of ferro-electric domains in multiphase structures. Silver Bromide (AgBr) and KRS-5 fibers were also grown recently for their good far infrared guiding properties.

However, Nd:YAG is the material which has been grown and studied most extensively, mainly for optical evaluation of amplifiers and oscillators under the present as well as other programs (References 6,7). Nd:YAG fibers are typically grown at a rate of 1 mm/min, and with diameter reduction ratios of 2:1. A typical sequence of diameters obtained from successive growth of Nd:YAG fibers is therefore 500 μm (ground rod), 250 μm , 120 μm and 60 μm . The crystallographic orientation of these fibers is determined by the seed crystal orientation. Although growth in other orientation directions have been demonstrated (see TABLE 1), Nd:YAG has been customarily grown in the (111) direction for easier end cleavage. This directionality is confirmed by the hexagonal cross-section observed.

Fibers grown with this technique, pulled in lengths of about 3 - 4 inches, show shiny faces, and all display single crystal character as confirmed by X-ray diffraction analysis. Unscratched fibers are surprisingly

flexible and can tolerate relatively small radius bends before breaking.

Slight diameter fluctuations are also observed along the fiber length, resulting from nonuniformities in the feed and pull drive mechanisms occurring during the growth process. Typical diameter variations are 5% to 10%, while they can be as low as a few percent along 5 - 10 mm long portions of the fiber. The spatial period of these surface ripples was measured to vary from 250 μm to 600 μm depending on the sample diameter and growth conditions. Growth and diameter instabilities were, however, far lower than previously reported (Reference 6) as a consequence of the various improvements implemented in the growth station during the last year. This situation allowed us in particular to grow Nd:YAG fibers with diameters as small as 15 μm . These new samples, grown from 100 μm fibers in length of 1 - 3 cm, show only 5 - 10% average diameter variations, which is actually satisfactory since only very short ($l \approx 2$ mm) fibers are needed in this range of diameter. This new result constitutes an improvement of the previous state of the art by a factor of 2, and opens the way to the exciting domain of single-mode single-crystal fibers.

C. FIBER PROCESSING

(1) End-Polishing

The physical quality of the end of a fiber, and in particular its flatness, is important for most optical device applications. Surface quality reflects on the phase front of the signal coupled into the fiber as well as on the launching efficiency. It was therefore important to develop suitable techniques to prepare the ends of single crystal fibers in a reliable and repeatable manner.

In an earlier program we showed that cleaved ends, obtained by breaking a Nd:YAG fiber after scoring it with a diamond blade, yielded fairly nice end faces perfectly suitable for the study of this type of fiber as a multimode waveguide (Reference 6). However, in the present work it was important to preserve the phase front of the optical signal as it travels back and forth through the fiber laser, and more accurate preparation methods were sought.

Under the present contract, a number of polishing methods were evaluated. In order to achieve a uniform, flat polish over the entire cross-section of a fiber, it is preferable to provide the fiber with a holder that increases its rigidity and prevents it from moving during the grinding and polishing operations. One of our earliest attempts involved mounting one or several fibers inside a glass capillary tube (O.D. ~ 5 mm). It appeared that this method does not provide enough support to the fibers as the bonding agent (epoxy) and the holder itself (glass) grind down faster than the harder Nd:YAG fibers.

To match the hardness of the holder to that of the fiber, subsequent polishing jigs were made of Nd:YAG rods. Capillary tubes of this material being difficult to fabricate, a slot is machined along the length of the rod with a circular diamond saw. The slot, from ~ 220 μm to 500 μm wide, has a flat bottom and runs to the center of the rod, as shown in Figure 3. The holder outside diameter is typically 6 to 8 mm, while its length is tailored to the desired fiber length. To assure rigidity and minimize the amount of softer bonding agent, several fibers (5 - 15) are laid in the groove and bonded into place. In the current embodiment the bonding agent used is a uv-curing epoxy glue (Reference 10), which is cured overnight under a low power uv lamp. After curing the fiber ends protruding from the edges of the holder

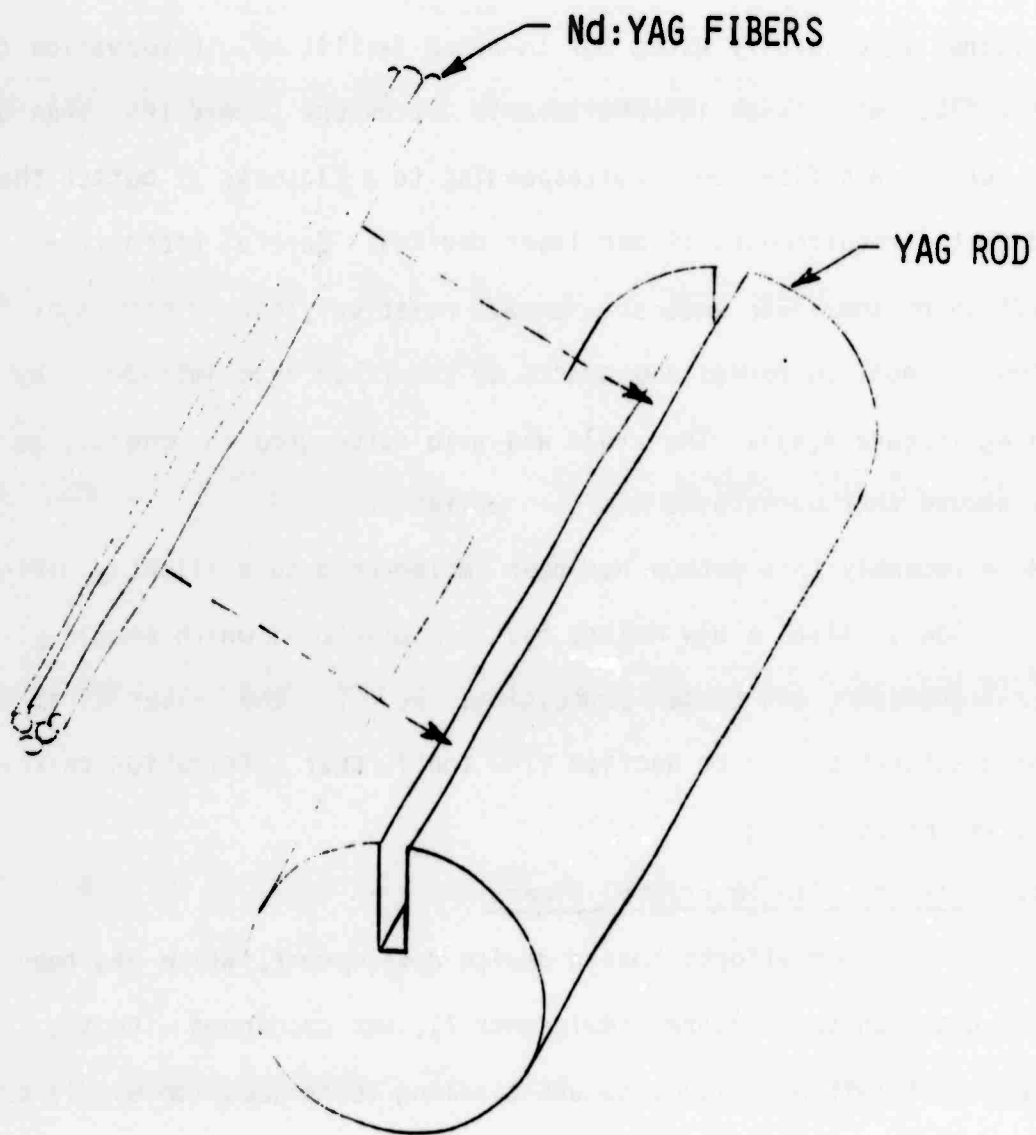


Figure 3--Nd:YAG Fiber End-Face Polishing Fixture.

are cut with a saw, and each end face is first ground, then polished, until all fibers show flat smooth ends. The fibers (and holder) can then be optionally retrieved by removing the epoxy with an appropriate solvent.

Throughout this work, over one dozen such arrays of fibers were assembled and polished successfully using our in-house facilities. Observation of the polished fiber ends in an interferometric microscope showed less than one fringe across each fiber end, corresponding to a flatness of better than $\lambda/4$ suited to the requirements of our laser devices. Careful microscope observation of the fiber ends also showed relatively good fiber edges, with very few residual chippings and cracks on the fiber edge introduced by polishing (Figure 4(a)). The yield was also quite good in general, as most fibers showed that both faces had been polished.

More recently this method has been implemented to a slightly different form of holder. Also, a new method has been developed which should yield further improvement and faster processing. We refer the reader to the following subsection and to Section VI-D for further information on the subject of end-polishing.

2. Cladding Single Crystal Fibers

One of our efforts toward device development, which has been in progress under another program (Reference 7), was concerned with the development of suitable claddings and cladding techniques for single-crystal fibers. Since the techniques developed under that program are of interest to the present work, we briefly review them in this section. They will be available for adaptation to the needs of fiber oscillators under future programs.

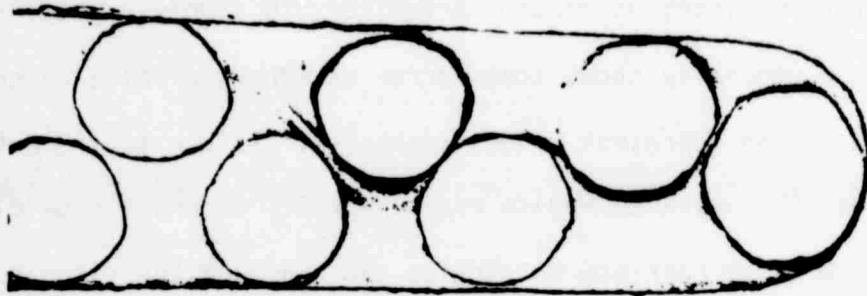


Figure 4(a)--Photograph of Polished Fiber Ends
(Array #16).

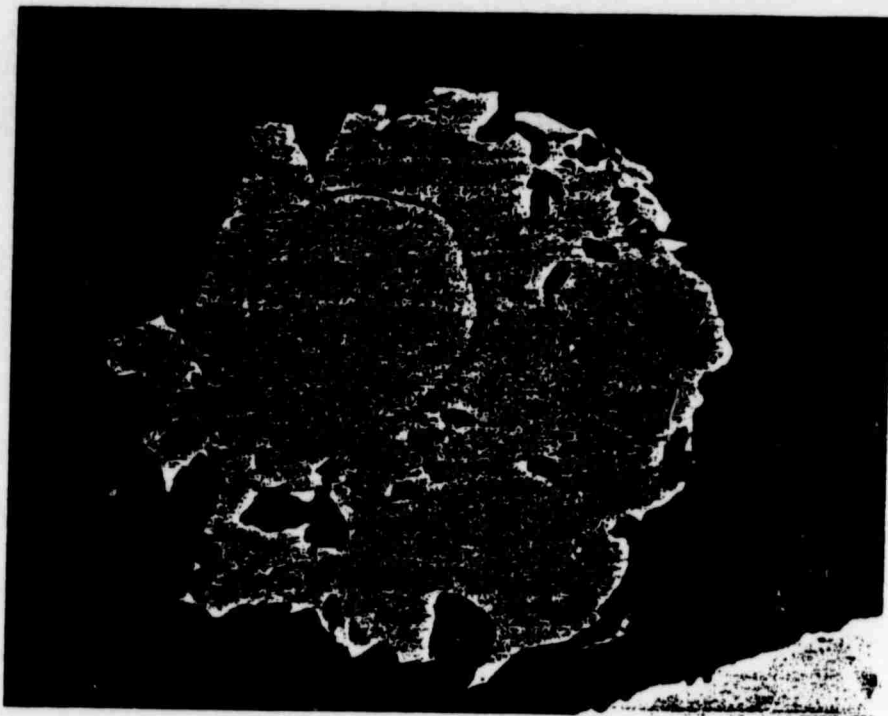


Figure 4(b)--Photograph of the Polished End of a
Nd:YAG Fiber Clad with SF-57 Glass
(Array #8).

One of the most important loss mechanisms in any type of optical fiber is scattering due to diameter fluctuations of the surface of the guiding region (core). In particular, as mentioned earlier, in single-crystal fibers the outer surface generally shows some degree of irregularities which scatter the optical signal and represent a loss mechanism. It can be shown by theoretical analysis that this loss mechanism may be greatly attenuated by placing a cladding with an appropriate refractive index around the fiber core (Reference 11). In essence, the cladding reduces the number of guided fiber modes to which the optical signal mode (presumably the fundamental mode) may be coupled by the fiber diameter perturbation. The effectiveness of the cladding at reducing scattering losses is thus directly related to the index difference Δn between the core and the cladding (Reference 11). Consequently, losses are minimized by making Δn as small as possible (Δn should however remain positive for waveguiding to be possible). For example, in a typical low-loss commercial glass fiber the core is surrounded by a cladding material with a slightly lower refractive index than that of the core, which isolates the core from the outside world and reduces scattering losses. Because glass fibers are generally fabricated by a pulling process, the core/cladding interface is smooth and the losses can be very low. Clearly a second advantage of cladding crystal fibers is that it reduces the number of guided modes the fiber can support, which is an important step towards the development of single-mode crystal fibers.

To reduce scattering losses and make crystal fiber devices practical we tried to partially reproduce the circumstances occurring in glass fibers by providing an appropriate cladding to single crystal fibers. Suitable materials and means for placing them on the outside of a Nd:YAG single crystal

fiber were investigated. A number of potential cladding materials and cladding deposition techniques were identified, covering a wide range of difficulty levels in realization and applications. Potential materials include liquids and waxes, gels, epoxies or solids. Possible deposition methods include extrusion, sputtering or in- and out-diffusion. This last technique, which relies on the implantation of chosen impurities or removal of some crystal constituents at the periphery of a crystal fiber to locally reduce its index, may provide the most flexible control of index profile. Alternatively, because of the availability of liquids with any index between ~ 1.3 and 2.2 , liquid claddings seem to be good candidates for an immediate approach. However, in view of the stability, hardness and appropriate range of indices offered by a variety of solids, most of our effort to date was devoted to experimental investigations of solid claddings.

Calculations show that a cladding thickness on the order of $10\text{ }\mu\text{m}$ should be enough for fibers with core diameters larger than $50\text{ }\mu\text{m}$. A promising way to achieve this goal is to use a sputtering method. In view of the potential of this approach, an existing in-house sputtering station was modified to the necessities of sputtering on cylindrical surfaces such as fibers. A motor was installed in the vacuum station that rotated the fiber about itself to present its entire outer surface to the flux of plasma. Since several continuous hours of operation are required to attain sputtered layers of several microns, a cooling system was mounted on the motor stage to prevent failure by overheating.

A promising material to sputter onto Nd:YAG is undoped YAG, which would provide a Δn of about 1.1×10^{-3} at $1.06\text{ }\mu\text{m}$ (Reference 12). However, because of the high cost of this material, preliminary sputtering runs were

performed with a quartz target ($n = 1.46$). Both commercial silica fibers (OD = 80 μm) and Nd:YAG fibers (OD = 100 μm) were used. On silica fibers, cladding was sputtered for 5 to 9 hours, leading to measured deposition rates of about 2 $\mu\text{m}/\text{hour}$. Although the process is slow, SEM photographs of the cladding surface and of cross sections of the clad fibers showed good adhesion to the fiber cores. The cladding thickness, up to 13 μm , is in general fairly uniform along the fiber length, with a slight tapering toward the ends of the fiber ($\sim 4\%/ \text{cm}$), located further away from the target. No cracks are noticeable on the cladding surface although some blisters developed, a situation which is not unusual on thick sputtered films. Insofar as the cladding is thick enough these imperfections should induce no additional signal loss.

Nd:YAG fibers clad by the same process yielded similar results. Again the core/cladding interface observed under SEM seems to be very smooth. The cladding surface was free of defects, probably as a result of uninterrupted deposition runs. The cladding, typically 10 μm thick, appeared somewhat brittle, which could be alleviated by annealing the clad fibers to relieve residual material stresses.

Sputtering of sapphire ($n = 1.7$) on Nd:YAG fibers yielded unsatisfactory results as the target shattered under the high-energy impact of the plasma beam. Sapphire sputters very slowly, and with lower energy beams deposition times become prohibitively long.

As an alternative, high-index glasses can be advantageously used as cladding materials, as they offer a wide range of optical properties at very low cost. A high-index lead-doped glass (SF57) (Reference 13) was selected because of the similarity of both its refractive index ($n \sim 1.82$) and

expansion coefficient with that of Nd:YAG. Another important property of this type of material is that its refractive index depends on the cooling rate applied during fabrication. By annealing the material (above $\sim 200^{\circ}\text{C}$ for SF57) after deposition and controlling its cooling rate, the cladding index can be tailored to any desired value.

Attempts at ion-sputtering SF57 glass on Nd:YAG fibers were so far unsuccessful as the material undergoes significant structural damage under the impact of even the lowest energy plasma beams. Although deposition rates on the order of $10\text{ }\mu\text{m/hour}$ and cladding thicknesses up to $50\text{ }\mu\text{m}$ were obtained, microscope investigation of the fibers clad in this process reveals inhomogeneous layered claddings permeated with cracks.

On the other hand, liquid phase deposition of high-index glasses on Nd:YAG fibers yielded very promising results while providing the solution to other problems as well. The low glass melting temperature ($\sim 400^{\circ}\text{C}$) and the similarity of its expansion coefficient to that of Nd:YAG make possible the deposition of molten glass onto Nd:YAG fibers without affecting the crystal structure or introducing critical internal stresses. A first cladding method involved dipping the fiber into a melt of the high-index glass and slowly pulling it out. To center the fiber in the cladding, funnel-like quartz crucibles were constructed with a long narrow orifice at the bottom through which the fiber is pulled. In early attempts the crucible was heated with a flame, but the use of heating wire coiled around the neck and main frame of the crucible greatly improved the uniformity of the melt. Finally a motorized feed was used for greater cladding thickness uniformity and reproducibility. Using this method, fairly thick claddings were obtained, on the order of $200\text{ }\mu\text{m}$ (total clad fiber diameter $\sim 500\text{ }\mu\text{m}$). Very few small bubbles were seen within the cladding, but none near the fiber core where they would be

detrimental. Cladding adhesion and strength were found to be better than that of sputtered claddings. However, a major problem was encountered in that the clad fiber was often bent (radius ~ 100 cm) probably because of asymmetric stresses associated with a less than ideal centering of the fiber core. Annealing did not cure the problem.

To circumvent this difficulty a second method was developed which involves mounting the fiber inside a capillary tube using high-index glass as both cladding and bonding agents. The outside diameter of the tube is large enough (≥ 3 mm) to facilitate handling and subsequent fiber end polishing. Early attempts used flint glass tubes, Nd:YAG fibers and SF57 glass. After firing at 600°C in an oven (during which the high-index glass melts and flows into the capillary) and cooling, the holder ends were polished. The cross section of the fiber again showed very smooth fiber edges and excellent fiber end flatness. When using a pyrex-glass instead of flint (which somewhat softens) the holder showed after curing internal cracks due to a strong thermal expansion mismatch. Further attempts involved Nd:YAG holders, the capillary then being replaced by a narrow slot, which provides a perfect thermal expansion match and eliminates the slight softening of the holder observed with flint glass. This process now enables us (a) to mount single fibers rigidly and permanently, (b) to provide a suitable cladding to the fiber, (c) to eliminate the use of softer epoxy and yield better quality end polishing (Figure 4(b)), (d) to deposit so-called hard AR-coatings onto the fiber ends, more durable than the currently used coatings (see Section IV-B-1), and (e) to apply the process to a large variety of single crystal fibers. We believe this method offers by far the most satisfactory solution to clad single crystal fibers, and with only minor improvements will become the future standard method of handling and processing crystal fibers.

SECTION III

THEORY OF MODAL OVERLAPS IN LASERS

A. INTRODUCTION

To optimize the optical interaction in optically end-pumped lasers, it was useful to study from a theoretical standpoint the effects of modal spatial overlaps on the laser behavior. Under this contract an analysis was therefore developed using the general formalism of mode overlap to derive very general expressions for the threshold and energy conversion efficiency of lasers in both guided and unguided geometries. This analysis, which involves the derivation of new laser equations, has the advantage of providing a general solution to the problem of pumping laser materials, and provides results that have a wide scope of applications. In this section we present the results of this analysis pertinent to the interpretation of the observed behavior of the experimental bulk and fiber lasers reported further on. We refer the reader to Appendices A through D for a more complete description of the details of these calculations.

In the following we shall consider a four-level laser material of length L placed in an external cavity which provides optical feedback and oscillation build-up. This laser is assumed to be end-pumped through the back mirror by an optical beam of wavelength λ_p . Our analysis is divided into three major sections. The first one addresses the general case of arbitrary pump and signal transverse modes, and derives general expressions for the laser single-pass gain, threshold and energy conversion efficiency. It develops the background to the last two sections, in which results are applied to the case of free-space (unguided) lasers and fiber (guided) lasers. Unless

otherwise specified, all numerical examples treat the case of Nd:YAG, using the materials parameters listed in TABLE 2, with a signal and pump wavelength of 1.064 μm and 0.5145 μm , respectively.

B. GENERAL FORMALISM

In a pumped laser system, the distribution functions of interest are the population inversion density $n(x,y,z)$, the pumping rate per unit volume $r(x,y,z)$, and the photon density of the i -th mode $s_i(x,y,z)$. They are related by the laser rate equations, which in a steady state may be written as (Reference 14)

$$\left\{ \begin{aligned} \frac{dn(x,y,z)}{dt} &= r(x,y,z) - \frac{n(x,y,z)}{\tau_f} - \frac{c\sigma n(x,y,z)}{n_1} \sum_{i=1}^m s_i(x,y,z) = 0 \end{aligned} \right. \quad (1)$$

$$\left\{ \begin{aligned} \frac{dS_i}{dt} &= \frac{c\sigma}{n_1} \iiint_{\text{cavity}} n(x,y,z) s_i(x,y,z) dv - \frac{c \phi_i}{2Ln_1} S_i = 0 \end{aligned} \right. \quad (2)$$

S_i is the total number of photons in the cavity in the i -th mode:

$$S_i = \iiint_{\text{cavity}} s_i(x,y,z) dv \quad (3)$$

where σ and τ_f are the laser material stimulated emission cross-section and fluorescence lifetime, respectively, while c is the velocity of light in vacuum, and n_1 is the medium refractive index. ϕ_i is the total round-trip cavity loss of the i -th signal mode, and L the optical cavity length.

Solving Eq. (1) for $n(x,y,z)$ and inserting the result in Eq. (2) yields the following equation describing the steady-state total number of signal

TABLE 2
PHYSICAL AND OPTICAL PROPERTIES OF Nd:YAG

Chemical formula	Nd:Y ₃ Al ₅ O ₁₂
Nd atoms/cm ³	1.38×10^{20}
Melting point	1970°C
Laser wavelength stimulated emission	1.064 μ m
Cross-section (@ 1.06 μ m)	$2.7-8.8 \times 10^{-19}$ cm ²
Fluorescence lifetime	230 μ sec
Index of refraction (@ 1.06 μ m)	1.8163
Linewidth	4.5 Å
Fluorescence efficiency	0.63
Scatter loss coefficient	~ 0.002 cm ⁻¹

photons S_i in the i -th mode:

$$J_i(S_1, S_2, \dots) = \frac{\delta_i}{2l\sigma\tau_f} \frac{1}{R} \quad (4)$$

R is the pumping rate, defined via the normalized pump distribution function $r_0(x, y, z)$:

$$r(x, y, z) = R \cdot r_0(x, y, z) \quad (5)$$

while $J_i(S_1, S_2, \dots)$ is the pump-to-signal overlap integral in the presence of all other signal modes

$$J_i(S_1, S_2, S_3, \dots) = \iiint_{\text{cavity}} \frac{s_{0,i}(x, y, z) r_0(x, y, z)}{1 + \frac{c\sigma\tau_f}{n_1} \sum_i S_i s_{0,i}(x, y, z)} dv \quad (6)$$

where $s_{0,i}(x, y, z)$ is the normalized signal distribution of the i -th mode

$$S_i(x, y, z) = S_i s_{0,i}(x, y, z) \quad (7)$$

Therefore

$$\iiint_{\text{cavity}} r_0(x, y, z) dv = \iiint_{\text{cavity}} s_{0,i}(x, y, z) dv = 1 \quad (8)$$

Equation (4) is the basic expression for the number of signal photons present in the cavity's i -th mode in the presence of other signal modes. Solving it for N cavity modes (there are then N equations) gives the number of photons

in each mode at a given pumping rate, as well as their dependence on the pumping rate, i.e., the pump threshold and conversion efficiency of each mode.

Oscillation of a single mode S_1 is described by Eq. (4) with $S_2 = S_3 = \dots = 0$, i.e.,

$$J_1(S_1) = \frac{\delta_i}{2\ell\sigma\tau_f R} \frac{1}{S_1} \quad (9)$$

where

$$J_1(S_1) = J_1(S_1, 0, 0, \dots, 0) = \iiint_{\text{cavity}} \frac{r_0(x, y, z) s_{0,i}(x, y, z)}{1 + \frac{c\sigma\tau_f}{n_1} S_1 s_{0,i}(x, y, z)} dv \quad (10)$$

The pumping rate required to reach threshold is obtained by setting $S_1 = 0$ in Eqs. (9) and (10), i.e.,

$$R_{th,1} = \frac{\gamma_1 n_1}{2\ell\sigma\tau_f} \cdot \frac{1}{J_1(0, 0, \dots, 0)} \quad (11)$$

where

$$J_1(0, 0, \dots, 0) = \iiint_{\text{cavity}} r_0(x, y, z) s_{0,i}(x, y, z) dv \quad (12)$$

The pumping rate is related to the absorbed pump power P_{abs} by

$$R = \frac{P_{abs}}{h\nu_p} \quad (13)$$

where $h\nu_p$ is the pump photon energy. From Eq. (11) the pump power absorbed at threshold is thus

$$P_{th} = \frac{h\nu_p}{\sigma\tau_f} \frac{\delta_i}{2\ell} \frac{1}{J_1(0)} \quad (14)$$

Equivalently, the unsaturated single-pass gain factor of the laser pumped with an absorbed pump power P_{abs} is

$$\gamma = \frac{\sigma\tau_f}{h\nu_p} \frac{P_{abs}}{A_p^*} \quad (15)$$

Here A_p^* is the effective pump area, given by

$$A_p^* = \frac{1}{\ell J_1(0)} \quad (16)$$

while P_{abs}/A_p^* is the effective (average) pump power density existing along the laser. Alternatively one can define an effective pump volume $V_p^* = \ell A_p^*$. Both quantities A_p^* and V_p^* are mostly functions of the pump and signal modes. We shall see in the following sections that it is convenient to normalize the effective pump mode area to the fiber active area A_f in the case of a fiber laser, and to the average pump mode area \bar{A}_p in the case of an unguided laser. This introduces the notion of filling factor $F_{\nu\mu nm}$, defined by

$$A_p^* = \begin{cases} \frac{A_f}{F_{\nu\mu nm}} & \text{(fiber case)} \\ \frac{\bar{A}_p}{F_{\nu\mu nm}} & \text{(unguided case)} \end{cases} \quad (17)$$

$$(18)$$

where the index pairs (ν, μ) and (n, m) characterize the signal and pump modes, respectively. With this notation the laser gain factor of Eq. (15) may be written as

$$\gamma = \gamma_0 F_{\nu\mu nm} \quad (19)$$

where γ_0 is the gain that would be expected when neglecting the signal and pump modal overlap, e.g., in the fiber situation

$$\gamma_0 = \frac{\sigma \tau_f}{h\nu_p} \frac{P_{abs}}{A_f} \quad (20)$$

With this notation the effect of the transverse structure of the interacting waves is described by a single additional parameter, namely the filling factor $F_{\nu\mu nm}$. This factor contains all the information pertaining to the efficiency of the interaction between the signal mode (ν, μ) and the pump mode (n, m) . We will see that in practical cases the F-coefficients can be accurately computed and conveniently tabulated. Since this result applies to any type of modes, similar tables can be generated for a variety of laser configurations. Furthermore, this formalism can be easily extended to the case of a laser optically excited by a multimoded pump. Then the filling factor entering in the gain expression [Eq. (19)] is replaced by the weighted factor

$$\langle F \rangle = \sum_{n,m} \rho_{nm} F_{\nu\mu nm} \quad (21)$$

where ρ_{nm} is the fraction of pump energy carried by the pump mode (n, m) .

This formalism is therefore a powerful tool which greatly simplifies the analysis of the gain in optically pumped single-mode lasers and amplifiers.

The laser output at a pumping rate R is given by

$$P_{out} = T_1 \frac{h\nu_s}{2\hbar n_1} c S_1 \quad (22)$$

where T_1 is the output coupler transmission, assuming the other mirror is a high-reflector (HR, $T_2 = 0$). Since Eq. (22) involves the number of photons S_1 , solution of Eqs. (9) and (10), the exact dependence of the cw output power P_{out} on the excitation power P_{abs} is expressed in a rather complicated mathematical form inappropriate for physical understanding. However, by looking at limited cases such as near threshold and far from threshold laser operations, one can derive a very simple and accurate analytical expression for this dependence. With a good approximation one can write the overlap integral $J_1(S_1)$ in the form of an expansion in S_1 (see Appendix A)

$$\frac{1}{J_1(S_1)} \approx \frac{1}{J_1(0)} + \frac{c\sigma\tau_f}{n_1} \frac{S_1}{\eta_p} \quad (23)$$

where η_p is the fraction of pump power carried by the active region:

$$\eta_p = \iiint_{\text{active region}} r_0(x,y,z) dv \quad (24)$$

Eliminating S_1 between Eqs. (22) and (23), and replacing $J_1(S_1)$ and $J_1(0)$ by their respective expressions as a function of the absorbed pump power (Eqs. (9) and (14), respectively), we find that the laser slope

efficiency is simply

$$s = \frac{P_{out}}{(P_{abs} - P_{th})} = \eta_p \frac{T_1}{\delta_0} \frac{h\nu_s}{h\nu_p} \quad (25)$$

Two assumptions were made to derive this result (see Appendix A). The first assumption is that the laser is operating far above threshold. However, comparison of exact and approximate solutions indicate that this result is also valid near threshold (see following sections). The second assumption is that the laser conversion efficiency s is reasonably large. This implicitly assumes that the signal and pump modes are reasonably comparable so that their spatial overlap is relatively efficient. The range of validity of this assumption therefore depends on the laser configuration, in particular whether it is guided or unguided. We shall see in the following sections that this range is rather broad in most practical cases of interest, and includes as expected, the region of maximum laser efficiency.

Within its limits of validity, Eq. (25) provides a simple and powerful result. It states that as long as the signal to pump spatial overlap is good enough, the pump to signal photon conversion process is relatively independent of the modal distributions involved. In other words, provided the pump and signal photons occupy the same general area, the probability of stimulated emission is large enough that essentially the entire inverted population is driven to the ground level (which again implies a relatively efficient laser to start with, and in particular a relatively low additional cavity loss $\delta_0 - T_1$). In such conditions the laser slope efficiency [Eq. (25)] is proportional to

- (1) η_p , the fractional pump power contained in the active region of the laser; if this region vanishes no active material is available, and no output power is expected. η_p can at best equal unity.
- (2) T_1/δ_0 , the ratio of output 'loss' to total loss; in the most favorable case (low cavity loss) it can be made very close to unity.
- (3) $h\nu_s/h\nu_p$, the ratio of signal to pump photon energy which constitutes the fundamental limit of any photon-to-photon conversion efficiency.

Another important result is that Eq. (25) holds for any pump mode. It also holds for any signal mode (as long as it is the only oscillating mode in the laser cavity). This expression is therefore a powerful result which applies to any single mode laser regardless of the pumping configuration. Note however that the output power P_{out} does depend on the pump configuration and pump mode through the threshold P_{th} [Eq. (14)]. Again, the laser material properties (σ, τ_f) only influence the threshold of oscillation, but not the conversion efficiency. Consequently, in order to fully characterize the response of a single-mode laser to a given excitation $r_0(x,y,z)$ and pumping arrangement the only overlap integral that needs to be evaluated is $J_1(0)$ [Eq. (12)].

Finally, to provide a different picture of this result, it is useful to define an effective signal mode area A_s^* . A more standard expression of the slope efficiency of a laser is (Reference 15)

$$s = \frac{1}{2} \eta_p T_1 A_s^* I_{sat} \cdot \frac{1}{P_{th}} \quad (26)$$

where

$$I_{\text{sat}} = \frac{h\nu_s}{\delta\tau_f} \quad (27)$$

is the laser material saturation intensity. Replacing P_{th} by its expression as a function of the pump effective area A_p^* [Eqs. (14) and (16)] and comparing to Eq. (25) leads to

$$A_s^* = A_p^* \quad (28)$$

which establishes a fundamental relationship between A_s^* (the effective area which saturates the gain medium) and A_p^* (the effective pumping area). Note that the same result would have been obtained if we had neglected modal overlaps (plane wave case) and assumed $A_p^* = A_s^* = A$ at the outset.

C. FREE-SPACE LASERS

As a first application of the above theory of interest to the work reported here, let us consider the case of a free space (unguided) laser. The laser configuration is specified in Figure 5. We assume that the pump beam, end-fed into a (miniature) laser crystal along the laser cavity axis, is a fundamental Gaussian beam with a waist w_p . Diffraction causes the pump beam to expand on either side of its waist so that its radius varies along the z-axis of the crystal as

$$w_p^2(z) = w_p^2 \left[1 + \frac{\lambda_p^2 (z - z_p)^2}{\pi w_p^2 n_2} \right]^2 \quad (29)$$

where λ_p is the pump wavelength in vacuum, n_2 the refractive index of the crystal, and z_p the location of the pump waist inside the crystal (Figure 5). Similarly, the signal mode has a TEM_{mn} Gaussian distribution

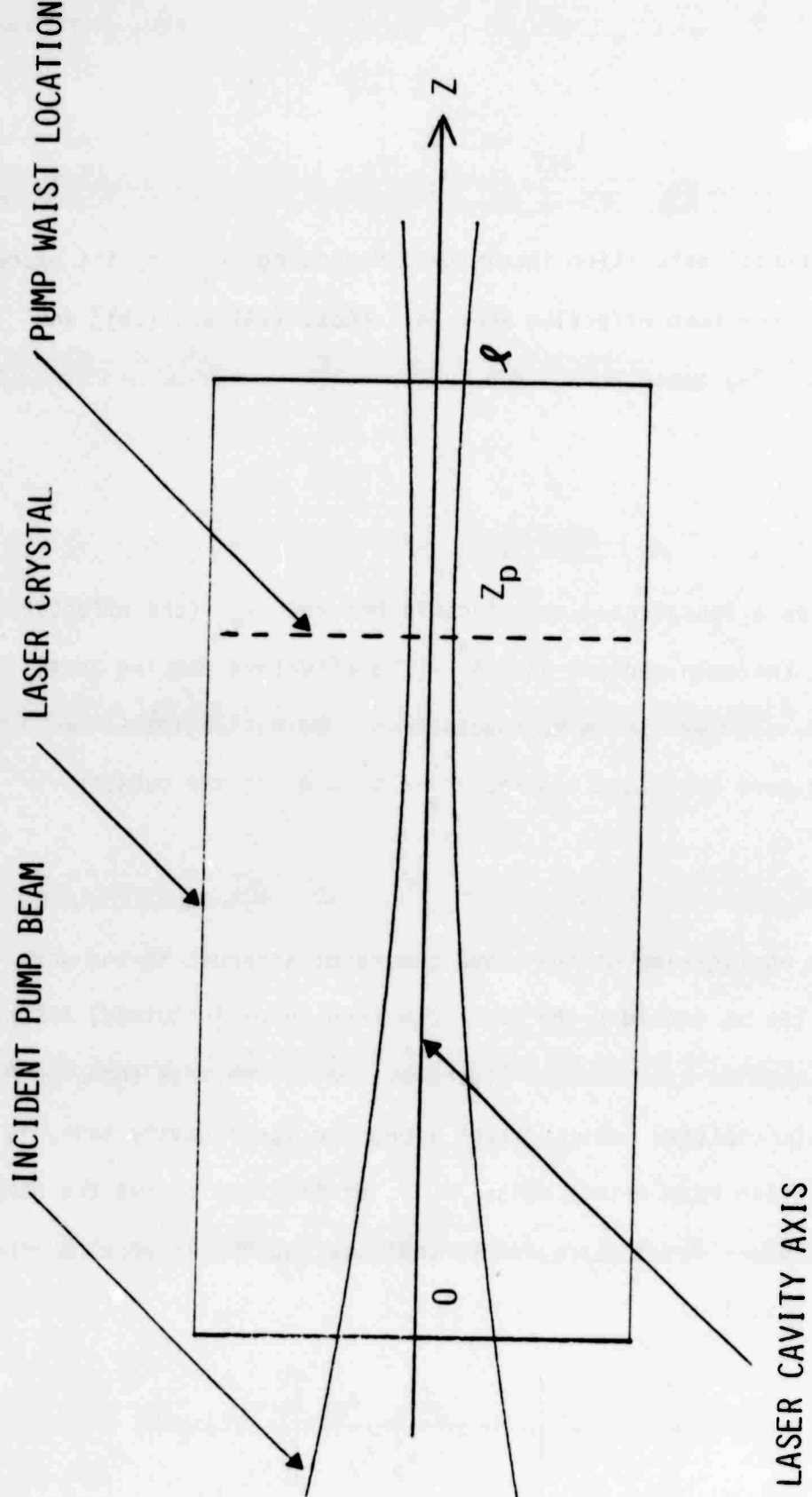


Figure 5--Schematic of the Gaussian Pump Beam inside the Laser Crystal.

imposed by the configuration of the resonant cavity. For all modes the beam radius at z is given by an expression similar to Eq. (29):

$$w_s^2(z) = w_s^2 \left[1 + \frac{\lambda_s (z - z_s)}{\pi n_2 w_s^2} \right]^2 . \quad (30)$$

where w_s , λ_s and z_s are the relevant parameters for the signal.

Further, we assume pump and signal modes are coaxial and aligned with the z -axis defined by the resonant cavity. The average pump beam area \bar{A}_p inside the crystal is approximated by

$$\bar{A}_p = \frac{\pi}{2} (\bar{w}_p)^2 \quad (31)$$

where \bar{w}_p is the average pump beam radius along the crystal:

$$\bar{w}_p^2 = \frac{1}{l} \int_0^l w_p^2(z) dz \quad (32)$$

Similar quantities can be defined for the signal mode.

These parameters can be calculated in a closed form using Eqs. (29) and (30). For example, for the fundamental signal mode we find that, assuming its waist is located at the center of the crystal ($z_s = z_p = l/2$):

$$\bar{w}_s^2 = w_s^2 (1 + \epsilon_s) \quad (33)$$

with

$$\epsilon_s = \frac{1}{3} \left(\frac{\lambda_s l}{\pi n_2 w_s^2} \right)^2 \quad (34)$$

Following the definition of the filling factor introduced in the previous section, $F_{\nu\mu nm}$'s can be computed for a few pump and signal modes. Because of the simplicity of the mathematical description of Gaussian modes, they can be evaluated in a closed form (see APPENDIX B). For example, for the most important case of a TEM_{00}/TEM_{00} configuration, one finds

$$F_{0000} = \frac{\bar{W}_p^2}{\bar{W}_p^2 + \bar{W}_s^2} \quad (35)$$

where \bar{W}_p is the average pump beam radius, calculated in the same manner as \bar{W}_s [Eq. (33)]. For this mode configuration the effective pump area is [from Eq. (18)]

$$A_p^* = \frac{\bar{A}_p}{F_{0000}} = \bar{A}_p + \bar{A}_s = \frac{\pi}{2} (\bar{W}_p^2 + \bar{W}_s^2) \quad (36)$$

This result is identical to that derived by other authors in a slightly different form (Reference 14). It is an important result, which was extensively used in our fiber laser threshold analysis, as we shall see in SECTION C of this report. We should also point out its simplicity. The computation of \bar{W}_s and \bar{W}_p only [Eq. (33)] is required to determine the efficiency of the pump and signal interaction and the laser threshold. Of course, similar expressions can be obtained for higher order signal modes. For example, for the TEM_{01} mode it can be shown that the filling factor is (see APPENDIX B)

$$F_{0100} = \frac{\bar{W}_p^4}{(\bar{W}_p^2 + \bar{W}_s^2)^2} \quad (37)$$

Returning to the fundamental case of a TEM_{00}/TEM_{00} configuration [Eq. (36)], a number of interesting comments can be made. First, for a given signal waist radius, the smaller the average pump radius \bar{W}_p the higher the overlap, and the higher the gain. Again diffraction limits the minimum average radius \bar{W}_p available for a given crystal length, index, and pump wavelength. It can be easily shown that the pump waist radius W_p that minimizes \bar{W}_p is (see APPENDIX B)

$$W_{p,opt} = \left(\frac{\lambda_p \ell}{\sqrt{3}\pi n_2} \right)^{1/2} \quad (38)$$

Similarly, for a given pump waist radius W_p , the smaller the average signal radius the higher the gain. In a signal beam focused much higher than the pump, most of the signal photons experience amplification. Of course, the smallest size of the signal is again limited by diffraction, which appears in the expression of \bar{W}_s as the ϵ_s quantity. Clearly there is a value of W_s which minimizes \bar{W}_s , and optimizes the gain (and the threshold) for a given crystal length ℓ . Note that \bar{W}_s does not necessarily optimize the laser output, which depends on the saturation level as well as the gain.

We show in Figure 6 the dependence of W_p^* on W_p as calculated from the exact form of the filling factor (see APPENDIX B), which takes into account the position z_p of the pump within the crystal, and of the fact that in a single pass end-pumped laser the gain is higher on the pump input side of the crystal. As expected the effective pump radius is minimum for a certain pump waist radius. Note also that the gain is lower when the pump waist is located at the far end of the crystal ($z_p = \ell$) than when it is at the near end of the crystal ($z_p = 0$). It is optimum when $z_p \approx \ell/2$ as expected for

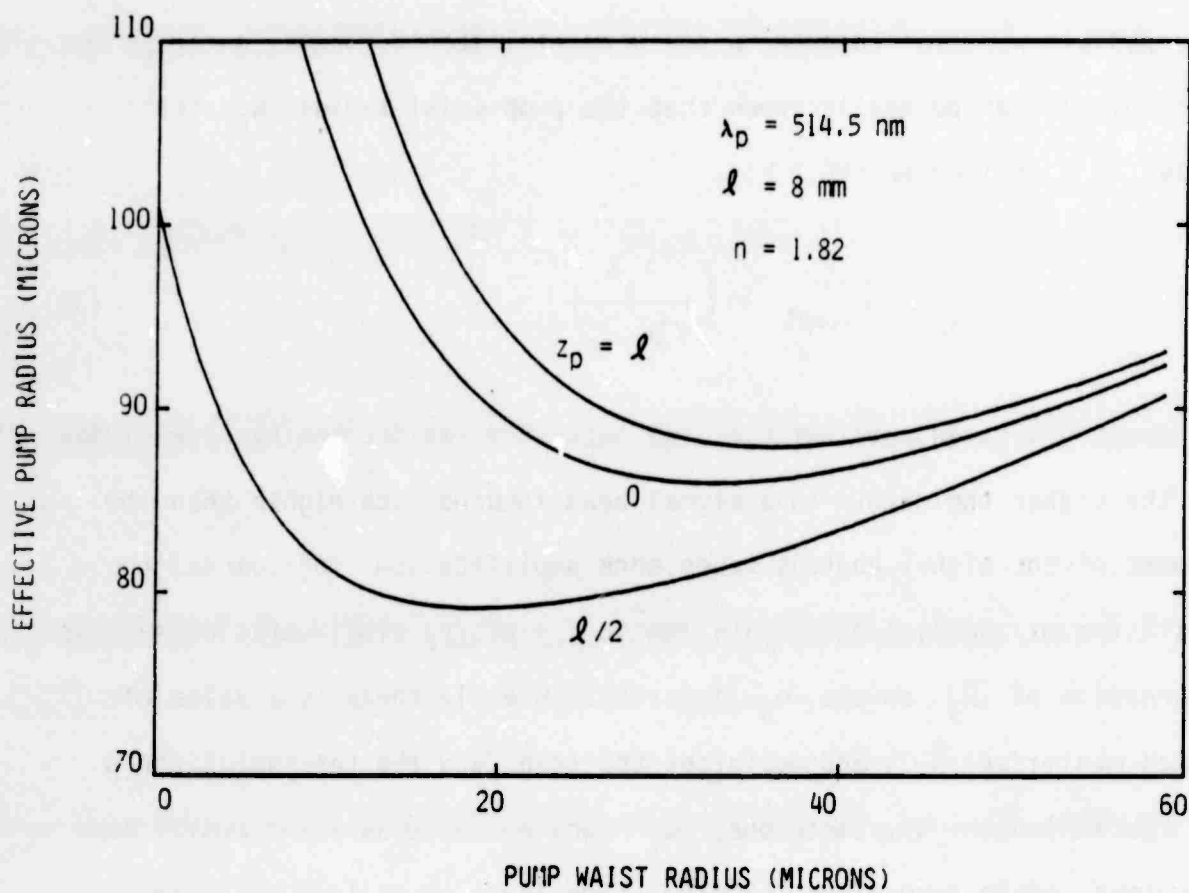


Figure 6--Dependence of the Effective Pump Radius on Actual Pump Waist Radius

crystals with lengths on the order of the material absorption length

$$l_a = 1/\alpha_a .$$

The accuracy and validity of the approximation made to derive the closed-form of the laser slope efficiency [Eq. (23)] was estimated in the present case of a free-space laser by comparing it to the exact overlap integral [Eq. (12)]. It shows that the approximation is more accurate for values of $\alpha = \bar{W}_s^2/\bar{W}_p^2$ near unity, as expected. The error in the slope efficiency is then less than a few percent. This is illustrated in Figure 7, which represents the slope efficiency of a Nd:YAG crystal laser ($T_1 = 1\%$, $\delta_0 = 5\%$, $\lambda_p = .5145 \mu\text{m}$, $\lambda_s = 1.064 \mu\text{m}$, $W_s = 25 \mu\text{m}$) versus pump waist radius. When the pump is focused either too tightly or too loosely, $\bar{W}_p \gg \bar{W}_s$ ($\alpha \ll 1$), the signal misses a good part of the population inversion, and the efficiency drops. As expected, maximum conversion efficiency may be reached only when the inverted population distribution and the signal mode present some degree of similarity. For this particular example, the agreement with the approximate form of the slope efficiency is excellent for \bar{W}_p ranging from about 10 to 50 μm .

The laser behavior was also analyzed far above the TEM_{00} threshold where higher order modes are likely to break into oscillation. As an example the threshold of TEM_{10} in the presence of TEM_{00} was calculated to be

$$P_{th}(\text{TEM}_{10}) = \frac{P_{th}(\text{TEM}_{00})}{\left(\frac{\delta_{00}}{\delta_{10}} - \alpha \right)} \quad (38)$$

where δ_{00} and δ_{10} are the cavity round-trip losses for TEM_{00} and TEM_{10} ,

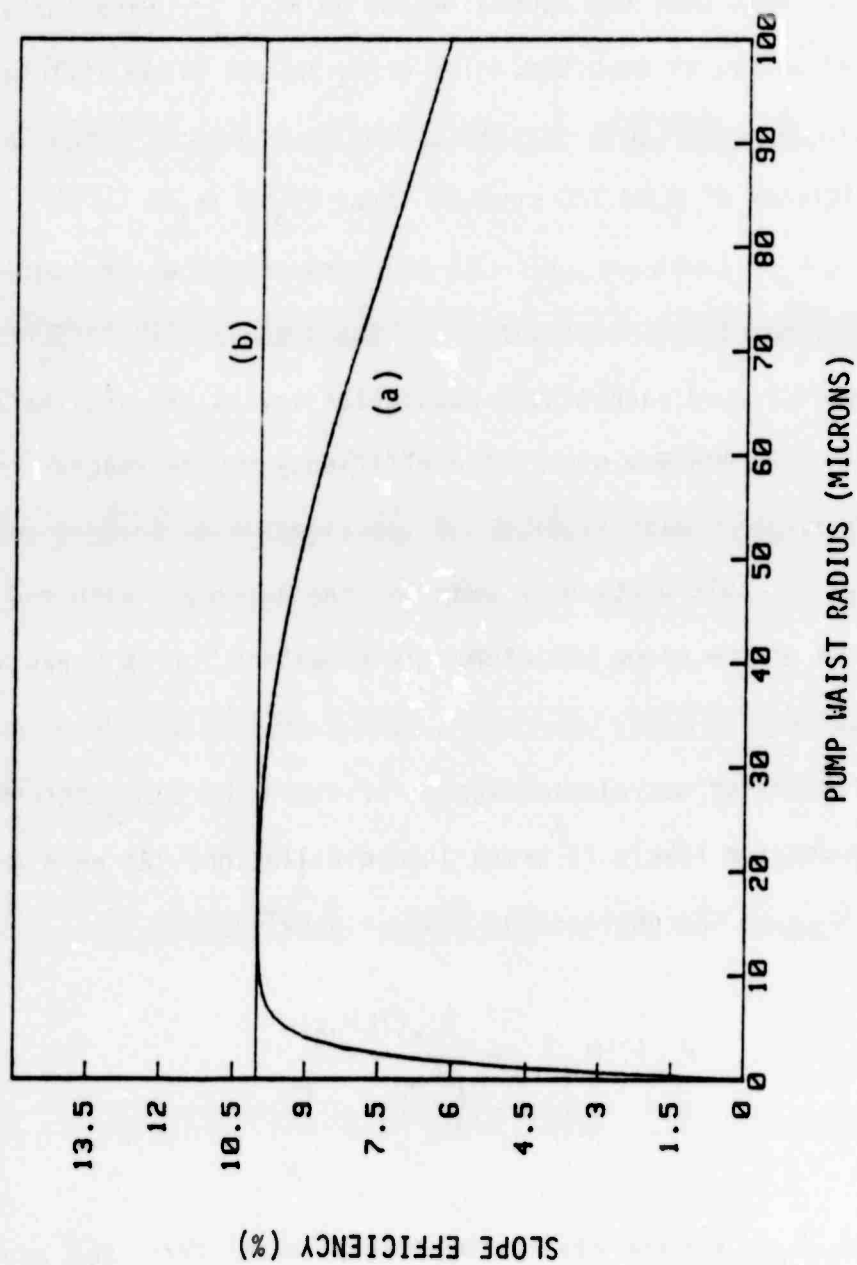


Figure 7--Dependence of the Slope Efficiency on the Pump Waist Radius for a Nd:YAG Bulk Laser pumped at $\lambda = 514.5$ nm ($T_1 = 1\%$, $\delta_0 = 5\%$, $W_0 = 25$ μ m); (a) Exact Solution; (b) Approximate Solution given by Eq. 25.

respectively, and α the same ratio $\overline{W}_s^2/\overline{W}_p^2$ as before. It appears that to reach the onset of TEM₁₀ oscillation, α must satisfy

$$\alpha < \frac{\delta_{00}}{\delta_{01}} \quad (39)$$

while the ratio δ_{00}/δ_{10} is in general smaller than unity. This reflects the fact that when the pump area is much larger than the area of either signal mode (and in particular, $\alpha \ll 1$), the small signal gains γ_{00} and γ_{10} of TEM₀₀ and TEM₁₀, respectively, are expected to become comparable. In such an event, as the pump power is turned up, the photon density due to TEM₀₀ does not build up too rapidly and does not saturate the gain γ_{10} too fast. This situation would clearly be modified in favor of the TEM₁₀ mode if the pump beam was offset from the cavity axis, or if a higher order pump mode was used. Signal modes with a low E-field on axis ($r = 0$) such as TEM₀₁ would then be favored over the TEM₀₀ mode. An important conclusion is that the control of the pump distribution is elementary to single-mode laser operation, as expected. Controlled pump distributions, as opposed to the highly multimoded situation occurring in most commercial solid state lasers, should therefore extend the single-mode output range of end-pumped lasers to much higher power levels. This is typically done in commercial lasers by introducing an aperture which further decreases δ_{00}/δ_{nm} . However, in general it also increases δ_{00} and reduces the laser overall efficiency.

D. FIBER LASERS

(1) Fiber Laser Configuration

In this section we consider the case of a fiber laser. The fiber is assumed to have a step-index profile and a circular geometry. The fiber core

(index n_1) is assumed to be the only active part of the fiber. The core is surrounded by a cladding of index n_2 ($n_2 < n_1$) infinite in the radial dimension, so that the fiber V-number is

$$V = \frac{2\pi a}{\lambda} \sqrt{n_1^2 - n_2^2} \quad (40)$$

For the sake of simplicity we assume the fiber is weakly-guiding, i.e., that its numerical aperture

$$\text{N.A.} = \sqrt{n_1^2 - n_2^2} \quad (41)$$

is small ($\text{N.A.} \ll 1$). The fiber guided modes are then almost linearly polarized and the so-called LP mode classification can be advantageously used (Reference 16). We also assume that the fiber fills the entire length L of the optical cavity, so that all optical signals remain guided throughout the cavity.

The fiber modes used for overlap computations, labeled LP_{nm} , have been widely studied in the literature, and are described in Appendix C. Their mode power density distributions are described by two mode integer numbers, namely the radial mode number n and the azimuthal mode number m .

(2) $F_{\nu\mu nm}$ Coefficients

Using the signal [Eqs. (C-2)] and pump [Eqs. C-5)] mode densities described in Appendix C, the filling factors were computed for a few mode configurations $\text{LP}_{\nu\mu}/\text{LP}_{nm}$. From the basic overlap expression [Eq. (12)] it readily appears that only pump and signal modes with the same azimuthal dependence will interact constructively. In the following we will therefore

consider only modes varying as $\cos^2(v\phi)$ (see APPENDIX C). The angular integration can then be done easily:

$$I_\phi = \int_0^{2\pi} \cos^2 n\phi \cos^2(v\phi) d\phi = \pi e_{vn} \quad (42)$$

where

$$e_{vn} = \begin{cases} 2 & \text{if } v = n = 0 \\ 1 & \text{if } v = 0 \text{ or } n = 0 \\ 3/4 & \text{if } v = n \neq 0 \\ 1/2 & \text{if } v \neq n, n \neq 0, v \neq 0 \end{cases} \quad (43)$$

Because of the complexity of the mathematical functions involved, and unlike the case of Gaussian modes of the previous section, the radial integrations can not be expressed in a closed form, and were analyzed by computer. The dependences of $F_{v\mu nm}$ on the fiber V-number and on the mode number were investigated, with emphasis on the behavior of $F_{01,nm}$ of interest for fundamental mode laser operation.

In Figure 8 we show the computed dependence of $F_{v\mu nm}$ on the fiber V-number for a few low order pump and signal modes in a Nd:YAG fiber laser. For each curve of Figure 8 the smallest allowed V-number V_c is the higher cutoff value of the mode pair $LP_{v\mu}/LP_{nm}$, below which one of the modes does not propagate. As V is decreased toward V_c , the corresponding F-coefficient decreases at first slowly, then rapidly, to vanish at $V = V_c$. This result stems from two facts. First, as one of the modes reaches cutoff,

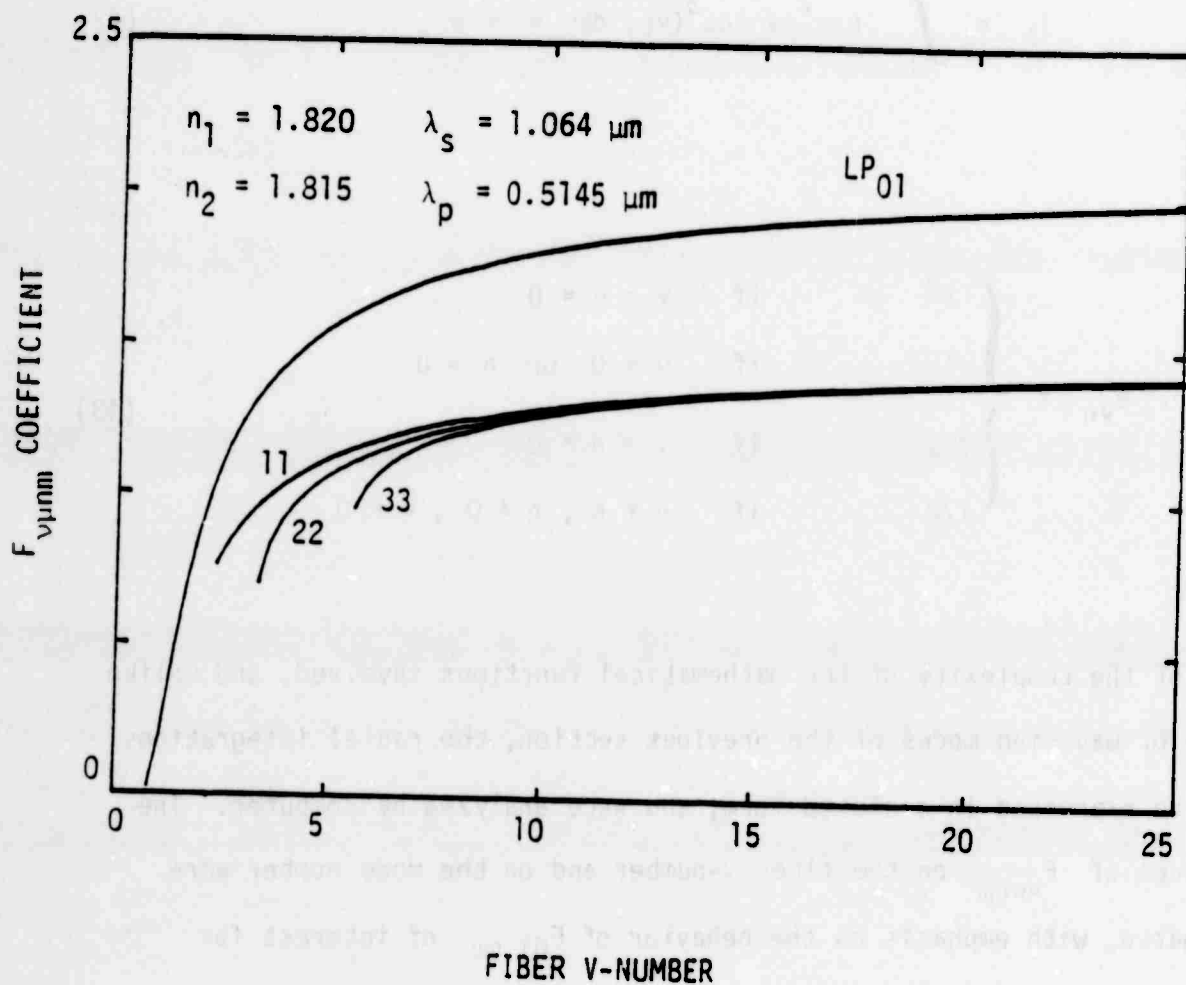


Figure 8--Variation of a few $F_{v\mu nm}$ Coefficients with the Fiber V-Number (at the Signal Frequency).

it starts spreading outward into the fiber cladding, and less and less energy is involved in the active region. Second, the energy density of this mode in the active region decreases, to vanish at cutoff. For V-numbers large compared to V_c the F-coefficients rapidly converge to asymptotic values only as function of the two interacting modes. This behavior stems from the fact that when both modes are far above cutoff their power density distributions become essentially independent of the fiber V-number, and so does their overlap. Since this convergence is rather rapid, in a practical situation involving a large V-number fiber laser all low-order $F_{\nu_{\mu nm}}$ may be replaced by their far-from cutoff limit with a good approximation. The filling factors are then universal numbers independent of the pump and signal frequencies and of the fiber geometry (provided it has a step-index profile), and are only a function of the mode numbers.

TABLE 3 gathers the large-V limit of filling factors computed for a few low order pump modes. For a fundamental signal mode (LP_{01}) pumped with a fundamental pump mode, the F-coefficient is $F_{0101} = 2.098$, i.e., the effective pump mode area A_p^* entering in the expression of the laser gain [Eq. (17)] is approximately half the area of the fiber core. When pumped with higher order modes, it can be shown that, as was intuitively expected, the corresponding overlap with ν_{01} signal is reduced. On the other hand, F-coefficients and therefore larger gains are expected for higher order mode configurations of the type LP_{nm}/LP_{nm} as a result of the larger signal and power densities and well-matched distributions. In fact, for this far-from-cutoff limit and configuration the pump and signal modes have the exact same spatial distributions. The symmetry of the matrix array given in TABLE 3 is also worth mentioning. In the far from cutoff region the guided modes are

TABLE 3

ASYMPTOTIC VALUES ($V \rightarrow \infty$) OF THE MODAL OVERLAPS $F_{\nu\mu nm}$

FOR A FEW LOW ORDER SIGNAL AND PUMP MODES

<div style="display: inline-block; transform: rotate(-45deg);"> PUMP ↓ </div> <div style="display: inline-block; transform: rotate(45deg);"> SIG. → </div>	01	02	11	12
01	2.098	1.800	1.435	1.677
02	1.800	2.743	.9422	1.576
11	1.435	.9422	2.327	1.681
12	1.677	1.576	1.681	2.943

independent of wavelength, so that the overlap between these modes is invariant under a commutation of modes:

$$F_{\nu\mu nm} = F_{nm\nu\mu} \quad (V \gg V_c) \quad . \quad (44)$$

This property can be usefully invoked to reduce computation time and the volume of tabulated data.

It is also interesting to look at the general evolution of $F_{\nu\mu nm}$ as the mode numbers are increased. In Figure 9 we show five series of coefficients, namely F_{010m} , F_{011m} , F_{012m} , F_{015m} and F_{018m} computed for $m = 1$ to $m = 30$, all pertaining to the important case of a fundamental signal mode. From these curves a number of interesting observations can be made. First, the largest possible overlap occurs with the fundamental pump mode, with $F_{0101} = 2.0983$. In this configuration the interaction mode distributions are as well-matched as can be. Second, for a fixed n ($n \neq 0$) the F_{01nm} coefficients increase with increasing m . This behavior arises from the fact that the distribution of an LP_{nm} mode has a maximum near the fiber axis ($r = 0$), and that this maximum increases with increasing m , as shown in Figure C-1 (see APPENDIX C). Since the signal mode LP_{01} has a broad maximum near $r = 0$, the overlap with an LP_{nm} mode increases with increasing m . Third, the F_{01nm} coefficients have a finite asymptotic value for large m , and this value is independent of n (for $n < m$). To understand this property we looked at the fractional energy carried by an LP_{nm} mode between $r = 0$ and $r = r_0$ as a function of r_0 (Figure 10). For large enough values of m , this energy increases almost linearly with r_0 , regardless of the value of n . For high order fiber modes each modal ripple (see Figure C-1) carries

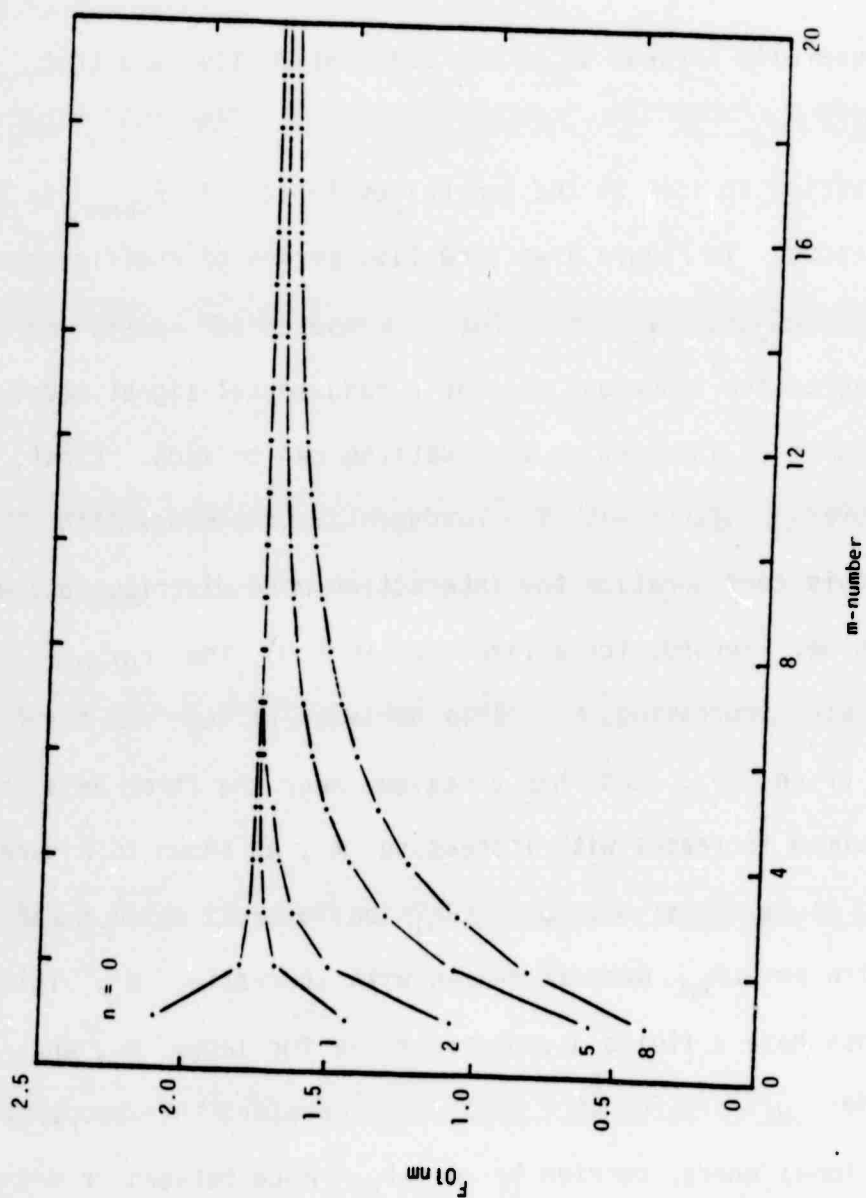


Figure 9-- Evaluation of Overlap Coefficients F_{01nm} for Increasing Value of the Modal Number m .

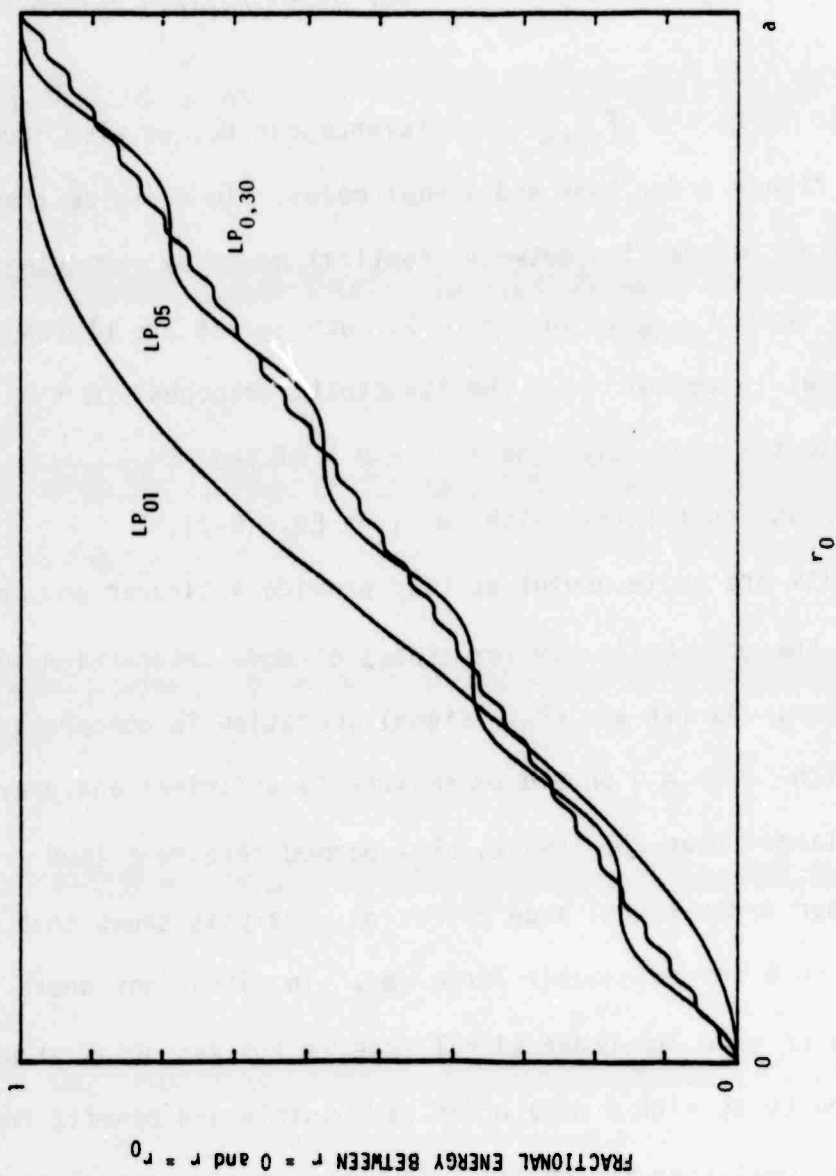


Figure 10--Fractional Modal Energy Contained between $r = 0$ and $r = r_0$ as a Function of r_0 for a few LP-Modes.

nearly the same energy. Their overlap with a given mode (here, LP_{01}) is therefore expected to converge to a finite value independent of m or n , as observed. Finally, this asymptotic value, equal to 1.7568, is reached even more rapidly when n is small. For all practical purposes, for $n < 10$ the F_{01nm} coefficients take this value for $m \geq 10 - 20$. The above conclusions, of course, apply to any $F_{\nu\mu nm}$ series with fixed values of ν and μ .

To estimate how large the $F_{\nu\mu nm}$ coefficients can be, we also looked at overlaps involving higher order pump and signal modes. To maximize these overlaps we considered interaction between identical modes by computing coefficients of the type F_{nmnm} . In Figure 11 such series are plotted versus m for several values of n . The asymptotic branches ($m \rightarrow \infty$) now go to infinity, since the peak value (near $r = 0$) of the LP_{nm} distributions increases indefinitely with m (see Eq. (C-3)).

The above results are quite useful as they provide a clearer and more complete picture of the originally complex aspect of mode interaction in a multimoded fiber laser. As far as LP_{01} signal operation is concerned, LP_{nm} pump modes (with $m \gg n$) should be reasonably efficient and provide a threshold only 30% larger than the lowest, LP_{01} -pumped threshold (see Figure 9). For higher order signal mode operation, analysis shows that F_{nmnm} range from 3 to 6 for reasonably large m . In situations where running the fiber laser on a low order signal mode is not essential it would be advantageous to go to as high a mode order as possible and benefit from a threshold many times lower (see Figure 11). However, in a practical device the higher loss experienced by these modes will have to be taken into account, together with the resulting slope efficiency.

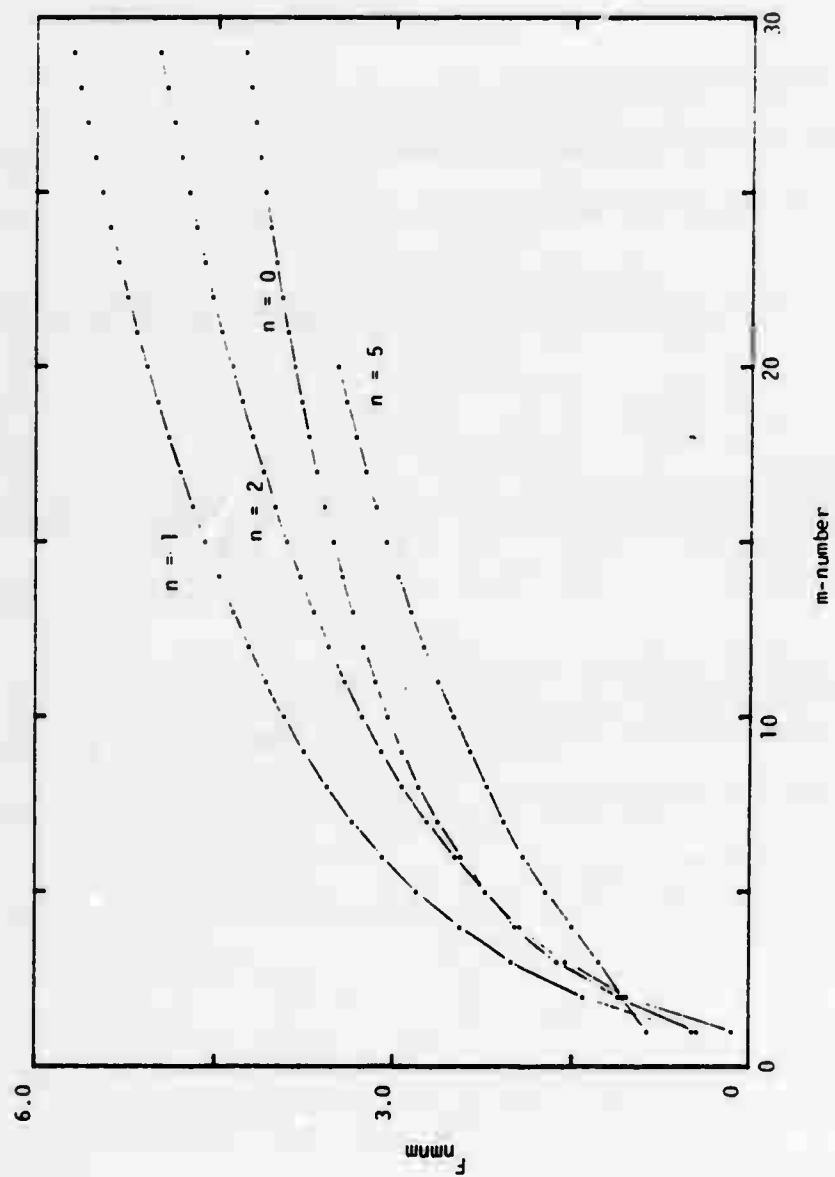


Figure 11--Evolution of a few Overlap Coefficients F_{nmm} for Increasing Values of the Modal Number m .

A last case of interest is that of a fiber laser in which the pump is distributed among a large number of guided modes. This situation may arise in particular when the fiber laser is excited by a Lambertian source (such as an LED) or a strongly diverging source (such as an LD). In this highly multimoded configuration we intuitively anticipate the pump mode density to be nearly radially uniform across the fiber core, and nearly zero in the cladding. For large enough V-numbers (say, $V \gtrsim 10 - 20$) it can be shown that the pump distribution can be approximated by a simple (normalized) square profile $r_u(r)$ ('u' standing for uniform) independent of the azimuthal direction ϕ :

$$r_u(r) = \begin{cases} \frac{1}{\pi a^2} & \text{for } r \leq a \\ 0 & \text{for } r > a \end{cases} \quad (45)$$

In a fiber laser excited in such a manner the inverted population distribution follows the step-index profile of the fiber. The overlap with any signal mode $LP_{\nu\mu}$, characterized by the coefficient $F_{\nu\mu,u}$, can easily be calculated from Eq. (12), yielding the simple result

$$F_{\nu\mu,u} = \eta_s \quad (46)$$

where η_s is the fraction of signal energy contained in the fiber core. For signal modes reasonably far from cutoff, $\eta_s \approx 1$ and the F-coefficient is approximately mode-independent and equal to unity. As expected, all modes with a reasonably good confinement experience the same gain. Note that

$F_{01,u}$ is about half the maximum anticipated value ($F_{0101} = 2.098$) which occurs with an LP_{01} pump mode. Consequently, the threshold of a fiber laser running in the fundamental mode is expected to be doubled by going from a fundamental pump mode to a highly multimoded pump distribution. This simple analysis therefore shows that although the use of a fundamental pump mode is desirable, it only provides a factor of two improvement over the multimoded pump configuration.

(3) Threshold

From the definition of A_p^* [Eq. (17)] we can write the laser threshold condition [Eq. (14)] as

$$P_{th} = \frac{h\nu_p}{\sigma\tau_f} \frac{\delta_{\nu\mu}}{2} \frac{A_f}{F_{\nu\mu nm}} \quad . \quad (47)$$

The dependence of the threshold on the modal overlap is entirely contained in the coefficient $F_{\nu\mu nm}$, which has been studied in the previous section. The dependence on the V-number involves both $F_{\nu\mu nm}$ and the loss factor $\delta_{\nu\mu}$ (which, for a given mode (ν, μ) does depend on V). Because of its complexity this last dependence is not considered here. Of greater interest to the present work is the dependence of the threshold on the fiber core radius. Intuitively, since the laser gain grows as the pump power density and therefore as the reciprocal of the fiber active area, it should be interesting to attempt reducing the fiber diameter. However, two other factors also contribute to this dependence: (1) the $F_{\nu\mu nm}$ coefficients and (2) the absorption of the pump by the fiber. This last contribution stems from the fact that for small enough core sizes, the pump mode is near cutoff, part of its energy is external to the fiber active area (core) and is not absorbed.

To take this effect into account it is actually more relevant to refer to the incident power threshold, i.e., the pump power coupled into the fiber laser at $z = 0$ at threshold. It can be easily derived from Eq. (47) and shown to be:

$$P_{th,inc} = \frac{h\nu_p}{\sigma\tau_f} \frac{\delta_{\nu\mu}}{2} \frac{A_f}{F_{\nu\mu nm}} \left(1 - e^{-\alpha'_a l}\right) \quad (48)$$

where the plane-wave absorption coefficient α_a has been replaced by the effective coefficient

$$\alpha'_a = \eta_p \alpha_a \quad (49)$$

where η_p is the fraction of pump energy contained in the fiber core [Eq. 24)]. For large enough fiber cores the pump mode is far above cutoff, $\eta_p \approx 1$ and $\alpha'_a = \alpha_a$, as assumed so far. Conversely, when the pump mode is near cutoff (small core), the fraction of pump energy absorbed vanishes.

Taking all three contributions into account, the incident pump power threshold of a fiber laser for a given pair of modes is expected to vary as follows. For large core radii, the modal overlap and effective absorption coefficient are independent of a , and the only dependence comes from the pump power density. The threshold grows quadratically with a . For very small core radii, the overlap and core area vanish, but so does the effective absorption coefficient. We actually expect the combination of these three effects to give an infinite threshold as $a \rightarrow 0$ since in the absence of an active medium the gain vanishes. Consequently a minimum threshold is expected for some optimum core radius a_{opt} .

This behavior is exemplified in Figure 12 for an LP_{01}/LP_{01} configuration. Note the parabolic growth of the threshold for $a > a_{opt}$, and the rapid increase in threshold when the pump mode reaches cutoff ($a < a_{opt}$). For practical fiber numerical apertures (N.A. $\sim .08 - .23$), the optimum core radius a_{opt} which minimizes the fiber laser threshold is in the range of 1.3 to 3.4 μm . However, they all correspond to a fiber V-number at the signal wavelength of $V_{opt} \approx 1.7$ (despite the fact that $P_{th,inc}$ is not a function of V only).

It is interesting to compare V_{opt} to the value V_{max} which maximizes the (average) pump intensity in the fiber, approximately $V_{max} \approx 1.1$ in a step-index fiber (Reference 17). As expected V_{opt} and V_{max} are of the same order of magnitude. V_{opt} also depends slightly on the pump wavelength ($V_{opt} \approx 1.9$ at $\lambda_p = 810$ nm) but is always in the range of 1 - 3. It does not depend on the laser properties of the material (σ, τ_f), and depends only slightly on the absorptive properties of the fiber (α_a, L) in the practical situation $\alpha_a L \sim 1$. For mode configurations other than LP_{01}/LP_{01} the value of V_{opt} is expected to be larger (since the energy density of higher order modes is maximum at larger V-numbers) and would have to be computed individually.

Although the above analysis does not take into account the dependence of the cavity loss and of the pump launching efficiency on the core dimension, it still shows that the choice of core size is elementary in the design of a fiber laser. In fiber lasers with a well-chosen core radius ($a \sim a_{opt}$) the optical gain per unit pump power is so large that even in a 5% round-trip loss cavity the laser threshold is very low, in the 10 - 50 μ watts range for Nd:YAG (Figure 12). The existence of an optimum V-value range also makes it

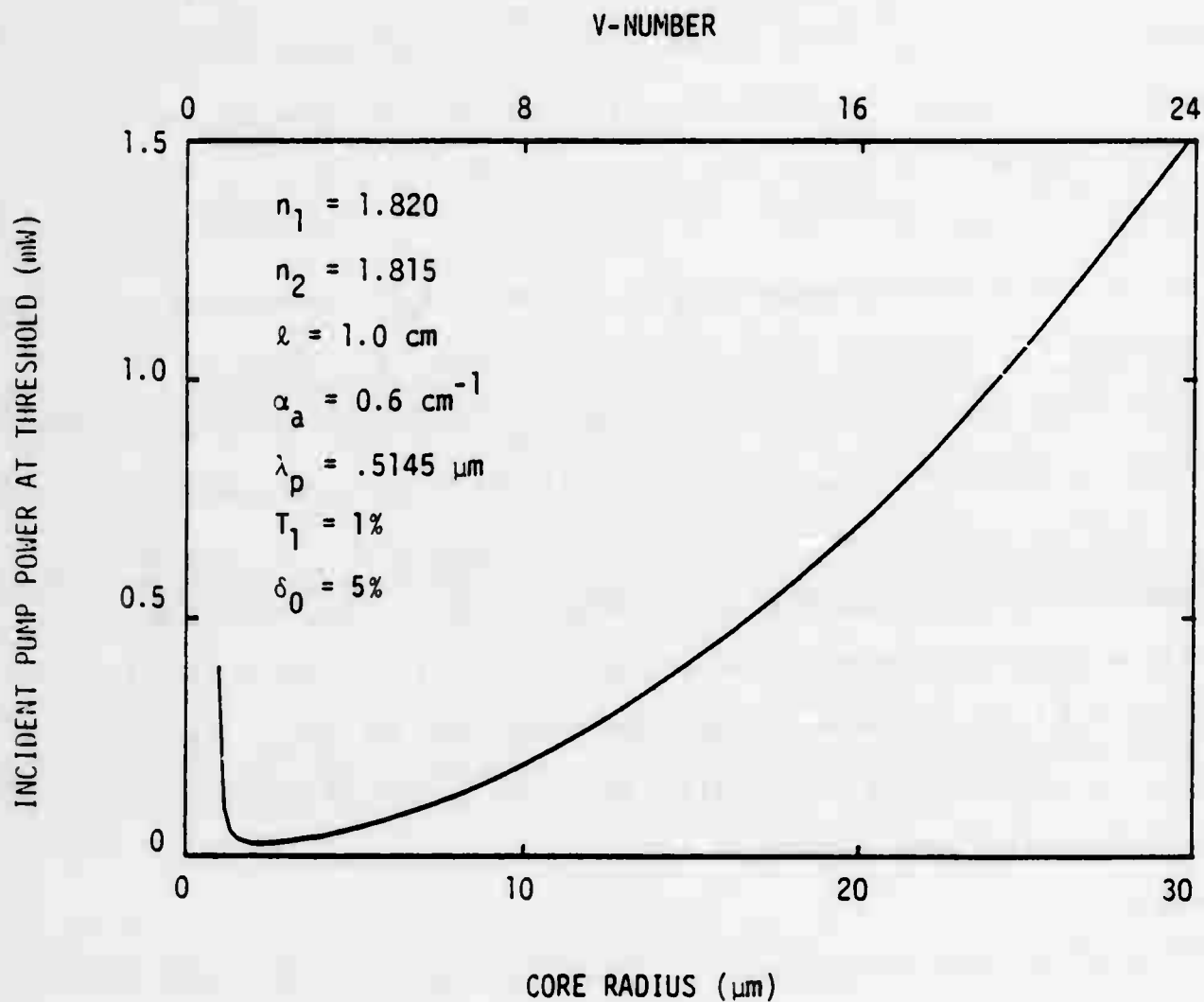


Figure 12--Dependence of the Fiber Laser Threshold on Core Radius in the LP_{01}/LP_{01} Mode Configuration.

convenient to estimate the optimum fiber laser configuration (assuming LP_{01} modes). For example, in a Nd:YAG fiber with $N.A. = .2$ and pumped at $\lambda_p = 810 \text{ nm}$, the lowest threshold would be obtained with $a_{opt} \approx 1.2 \mu\text{m}$. Since the design of a laser can not be complete without the analysis of its slope efficiency, we postpone further discussions to a later section.

(4) Slope Efficiency

As mentioned earlier, the power output P_{out} of a fiber laser at a given pumping rate [Eq. (22)] is proportional to the total number of signal photons in the cavity S_1 , as per solution of Eqs. (9) and (10). In Figure 13 we show the dependence of P_{out} on the pump power absorbed by the fiber active medium P_{abs} for a few values of the cavity loss $\delta_{\nu\mu}$ for the (LP_{01}, LP_{01}) mode configuration. Solid curves are exact solutions obtained from Eq. (10) by computer simulation. Dashed curves were computed from the approximate form of the slope efficiency [Eq. (25)]. As expected, the exact dependence of P_{out} on P_{abs} is very nearly linear. More specifically, it can be shown that the slope efficiency increases slightly as the laser is pumped harder. However, it does not increase by more than $\sim 20\%$ from just above threshold to very far above threshold. Comparison of the exact and approximate solutions (Figure 13) indicates that the approximation (developed in APPENDIX A) is quite accurate and, as stated, is valid everywhere above threshold. The discrepancy between exact and approximate predictions is small, between 5% and 10% in the example of Figure 13. As anticipated this discrepancy is smaller for higher efficiencies.

The dependence of the slope efficiency of a fiber laser on the fiber V-number is shown in Figure 14 in the important case of a fundamental signal mode (LP_{01}) and different pump modes. We find again that just like for the

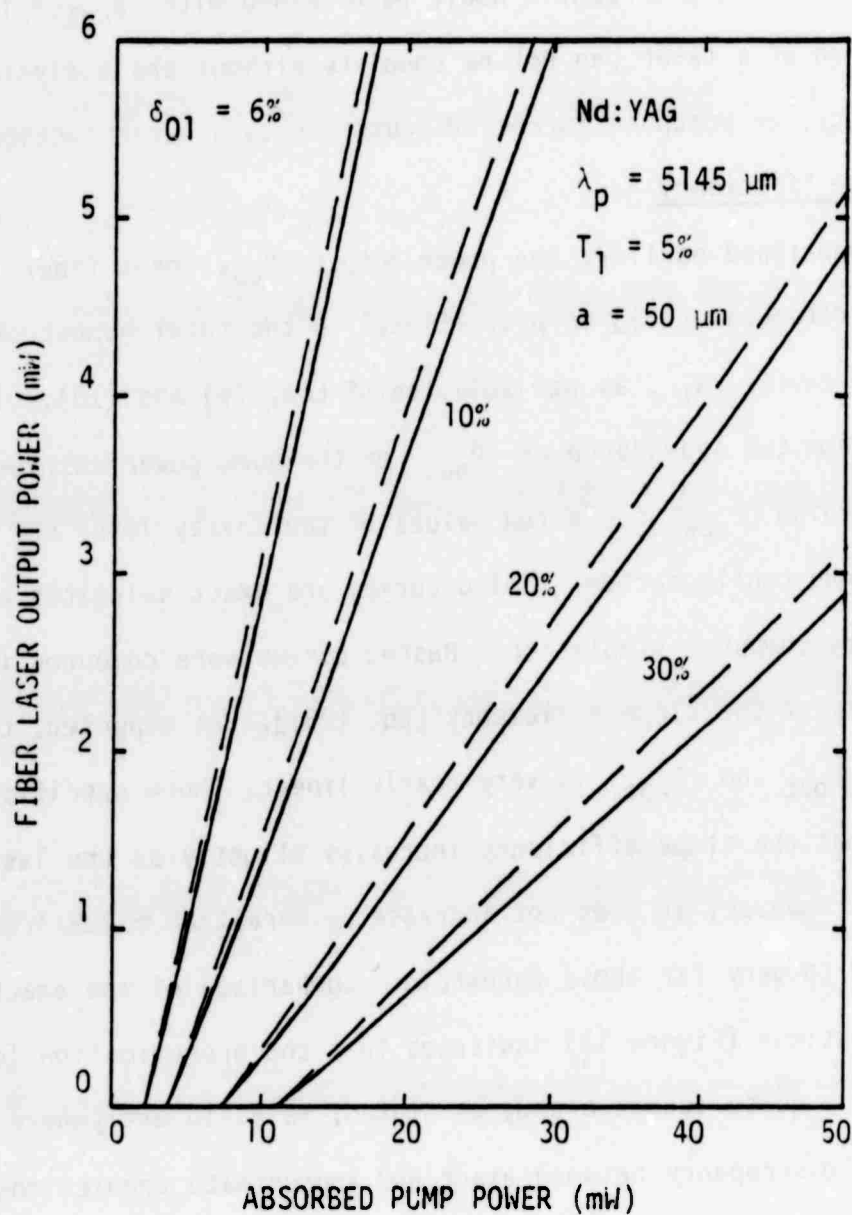


Figure 13--Exact (Solid Curves) and Approximate (Dashed Curves) Theoretical Dependence of the Output Power of a Fiber Laser on Absorbed Pump Power for Increasing Round Trip Cavity Loss. Signal and Pump Modes are LP_{01} , Fiber V-Number is 40.

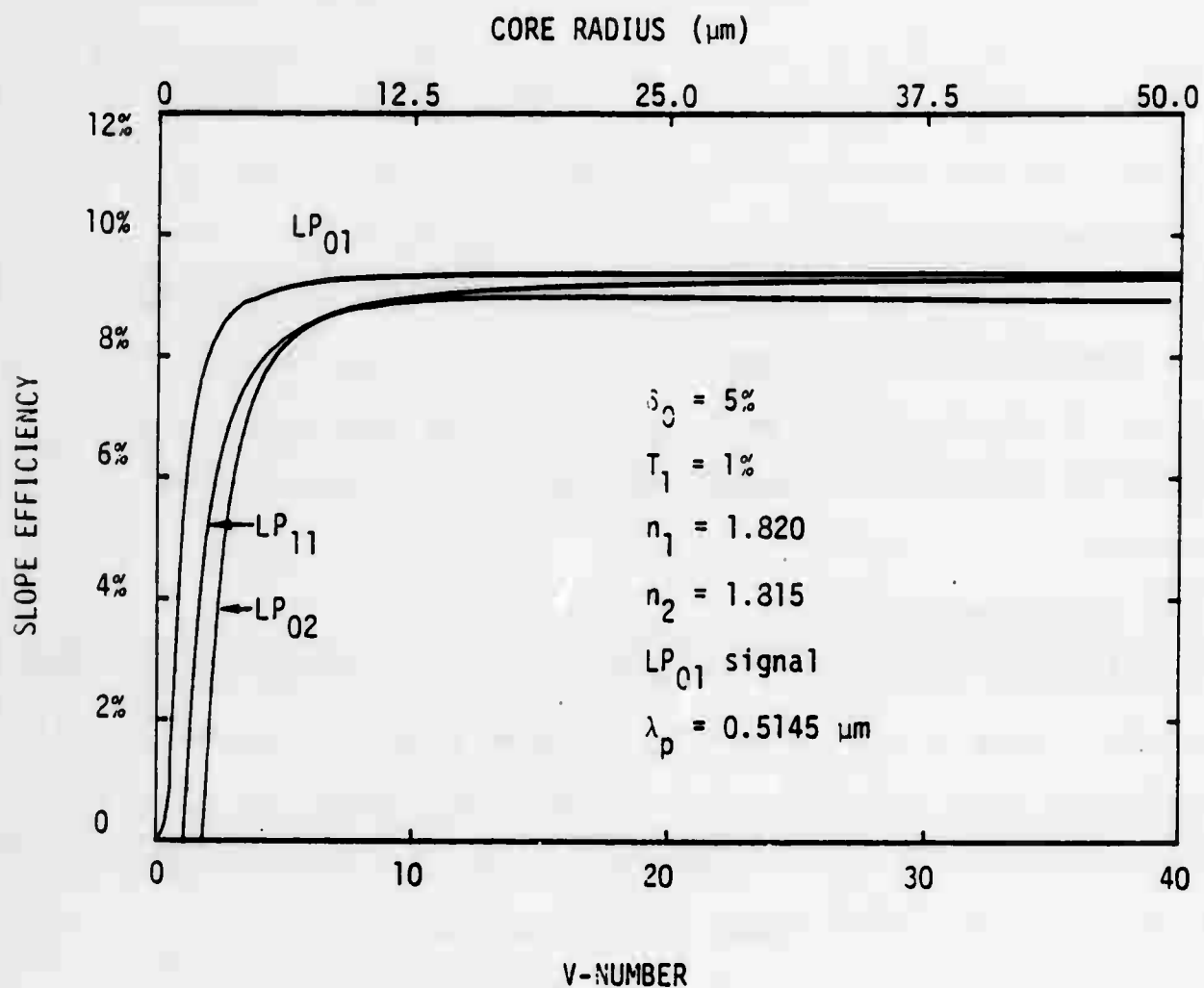


Figure 14--Slope Efficiency Dependence on the Fiber V-Number for an LP_{01} Signal Mode and Various Pump Modes.

$F_{\nu\mu nm}$ coefficients, the slope efficiency increases rapidly from zero at $V \sim V_c$ (pump cutoff, no pump energy involved in the fiber core) to an asymptotic value at $V \gg V_c$ (where the mode profiles no longer depend on V). This asymptotic value agrees well with the slope efficiency given by the approximate form of Eq. (25).

Finally, as mentioned concerning free-space lasers, we find that in fairly efficient lasers, the slope efficiency does not depend on the modes involved for modes sufficiently far from cutoff. Under such conditions the relative confinement provided by the fiber core, combined with the large probability of stimulated emission, guarantees efficient stimulated relaxation of most of the inverted population regardless of the exact photon distributions.

(5) Fiber Laser Design

Combining the results of the two previous sections allows one to make the best choice of core radius in the design of a low threshold, high slope efficiency fiber laser. A compromise must be made between low threshold (ideally a core radius of a few micrometers) and high slope efficiency (a core radius of at least 10 - 20 μm , depending on the pump mode). In the fundamental case of LP_{01} modes, and for the parameters used in our example, the optimum value is in the range of 8 to 10 μm , or a V-number of 6 to 8.

For practical reasons which will become apparent in later sections, it may be difficult, at least for some materials, to fabricate fibers with diameters much smaller than about 40 μm . In other cases, such as Nd:YAG, it is possible to fabricate fibers as small as 15 μm in diameter, but handling difficulties may then require the use of larger fibers. It may also be preferable to use slightly larger diameter fibers and benefit from reduced

surface scattering losses (Reference 6). However, in such cases going to a somewhat larger fiber size does not significantly degrade the laser performance. Reference to Figure 12 shows that by going from an optimum $10\text{ }\mu\text{m}$ core radius to a $20\text{ }\mu\text{m}$ radius, the fiber laser only requires an additional 0.5 mW to reach threshold, while the slope efficiency remains nearly unchanged. In the present example of a $\sim 10\%$ efficient laser, this 0.5 mW only results in a $50\text{ }\mu\text{W}$ reduction of the laser output power. In a laser with a maximum efficiency ($\sim 48\%$) it would still represent an output reduction of only $250\text{ }\mu\text{W}$. Consequently, a $40 - 50\text{ }\mu\text{m}$ core diameter fiber laser will perform with essentially the same overall efficiency as an optimized $16 - 20\text{ }\mu\text{m}$ diameter laser. Furthermore, since in general fiber propagation losses are also reduced by increasing the fiber core size, in a practical situation the optimum core size will be somewhat larger than that predicted by the present model.

As similar curves can be generated for any mode configurations and cavity parameters, it is a relatively simple matter to design the optimum configuration in any situation. However, in the fundamental case of LP_{01} pump and signal modes, the above results are typical. As a rule of thumb, a fiber with a V-number in the range of 5 to 25 will yield the best results.

(6) Summary

For easy reference we briefly summarize below the major results of this theoretical section pertaining to the behavior of fiber lasers. We have shown that

- The gain factor in a guided fiber laser can be written in essentially the same form as in a free-space laser (Eq. 19);

- The effective pump mode area required to calculate this gain factor is proportional to the fiber core area, and the proportionality constant $F_{\nu\mu nm}$ is only a function of mode numbers for $V \gtrsim 10$;
- The $F_{\nu\mu nm}$ can be easily tabulated;
- The F-coefficient is only half its maximum value when the pump is uniformly distributed across the fiber core instead of being in the LP_{01} mode;
- The fiber laser power output grows linearly with absorbed pump power;
- The slope efficiency can be written in a simple, accurate form and can be easily calculated [Eq. (25);
- For far from cutoff pump modes, the slope efficiency is independent of the V-number and of the pump mode.
- The overall laser efficiency is optimized in a fiber with a V-value of 6 - 8, although in practical situations values up to ~ 25 will give similar results.

SECTION IV

ARGON-LASER PUMPED Nd:YAG LASERS

We describe in this section work on cw Nd:YAG lasers end-pumped at $0.5145 \mu\text{m}$. In SECTION A we present the results obtained in unguided miniature Nd:YAG lasers made of a small crystal rod placed in an external optical cavity. In SECTION B we report cw oscillation of a number of Nd:YAG fiber lasers of different geometry, and their characterization. Emphasis is put on the guiding properties of these devices, and on the sources of residual loss. These subjects will be addressed in further detail in SECTION VI after description of the results obtained with laser diode pumped fiber lasers (SECTION V).

A. MINIATURE BULK LASERS

1. Laser Configuration

Experiments on bulk lasers involved small commercial crystals of Nd:YAG as an active material, placed in an external optical cavity. A schematic of the experimental arrangement is shown in Figure 15. The pump beam at $\lambda_p = 5145 \text{ \AA}$ was produced by a cw argon-ion laser (Coherent CR-6) with a maximum output power at that wavelength between 0.5 and 1.0 watt depending on laser conditions. The laser beam was transformed by a spherical lens so as to match the fundamental mode of the laser cavity at the signal wavelength ($\lambda_s = 1.064 \mu\text{m}$). The cavity itself was formed by two high reflecting short radius mirrors (Reference 18). The optical signal coming out of the cavity was separated from the residual pump signal by a $1.064 \mu\text{m}$ spike filter and a high-pass (color) filter. The output of Nd:YAG lasers was observed with an infrared camera (not represented).

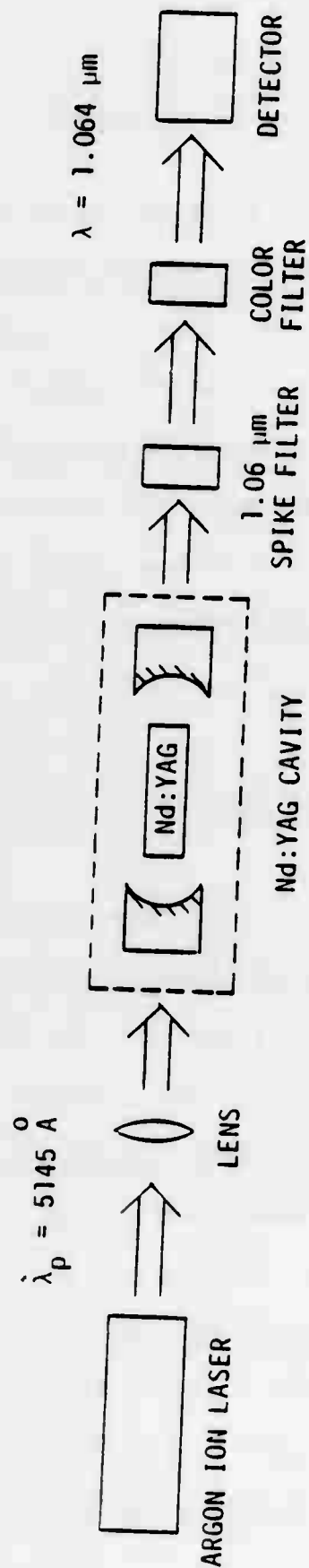


Figure 15---Schematic of the 514.5 nm End-Pumped Miniature Nd:YAG Laser Experimental Arrangement.

In all experimental arrangements involving bulk crystals, both cavity mirrors had a radius of curvature of $R = 10 \text{ cm}$, with respective reflectivities of 99.9% and 99.5% or 95.0% at $1.064 \text{ }\mu\text{m}$. Both mirrors were about 89% transmitting at the pump frequency. The cavity length was typically $L = 10 \text{ mm}$, i.e., only slightly longer than the crystal itself. From these data, the calculated radius of the signal beam waist supported by the cavity, which is located at the center of the cavity, is $64.5 \text{ }\mu\text{m}$.

A schematic of the optical cavity is shown in Figure 16. Each mirror was placed in a gimbal mount provided with two orthogonal tilt angle adjustments. The gimbal mounts were mounted on separate translation stages for adjustment of the length of the cavity. The assembly was secured on a mounting platform, itself attached to a three-axis translation stage to position the optical cavity with respect to the pump beam. The pump beam could be steered with respect to the axis of the cavity by two independent mirrors, although it was mostly stationary. The Nd:YAG crystal was placed on a pedestal in the center of the optical cavity.

Before use in the cavity, the end faces of the Nd:YAG crystal were first polished and then anti-reflection (AR) coated for $\lambda = 1.064 \text{ }\mu\text{m}$ using in-house facilities. Anti-reflection coating is necessary because Fresnel losses at the Nd:YAG/air interfaces are significant ($\sim 8.5\%$ per face) and may increase the threshold pump power.

2. Laser Characterization

(a) Nd:YAG Crystals

A total of four different crystals were used to characterize bulk Nd:YAG lasers, numbered 1 through 4. Their dimensions and the pump wavelength at which they were tested are summarized in TABLE 4 (the last dimension is

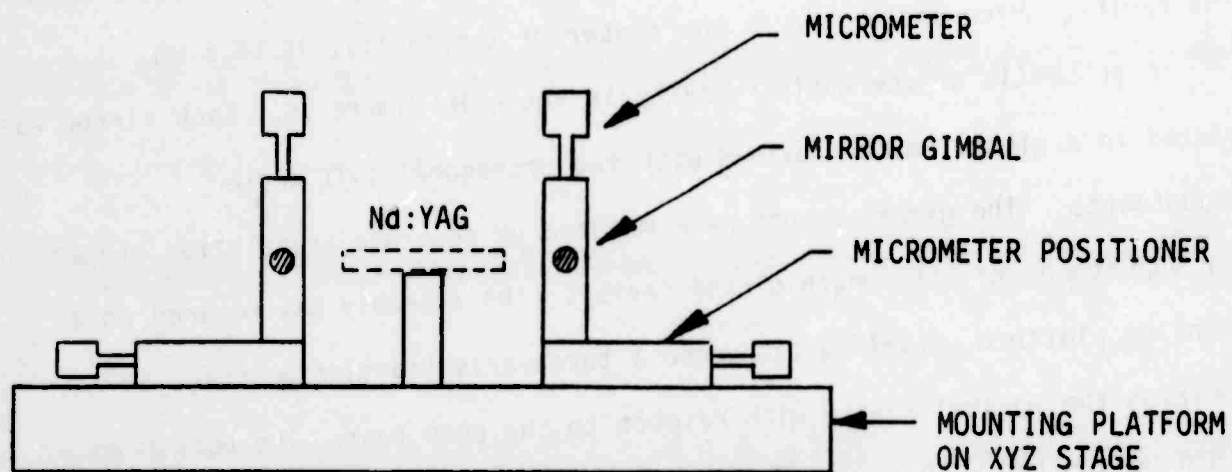


Figure 16--Miniature Nd:YAG Laser Cavity.

taken along the cavity axis). Crystal #2 was found early to have a defective AR-coating (the only coating which was performed by outside facilities), and was subsequently abandoned for crystals #1 and #3.

TABLE 4
Nd:YAG CRYSTALS DATA

Crystal Number	Dimension (mm)	λ_p (μm)
#1	1 x 1 x 7.5	0.5145
#2	3 x 8.0	0.5145
#3	1 x 1 x 7.5	0.5145
#4	6 x 2 x 4.0	~ 0.825/ 0.5145

(b) Output Measurements

Laser action of miniature Nd:YAG bulk lasers pumped at 0.5145 μm was successfully obtained in three crystals (see TABLE 4), two of which showed very good performance. Routine alignment of the cavity proceeded by using the pump beam as a probe in a standard fashion. Alignment of the back reflected beams with the incident beam led to the typical flickering of the pump light resonating in the cavity. Lasing action was then observed at higher pump power. The threshold was then reduced by refining the mirror alignment. It was found that the configuration described above, which uses in-house designed gimbals, lent itself quite well to an easy alignment of the laser.

Absolute measurements of the output power of these lasers were done by recording the output power for increasing pump power. Measurements of both the signal and the pump power incident on the focusing lens (see Figure 15) were performed with a power meter (Reference 19) calibrated at 0.5145 μm and 1.064 μm . The relative amount of pump power absorbed by the crystal was generally estimated in each particular case by measuring the transmission of each individual optical element and the Fresnel reflection from the crystal faces. The measured value was always consistent with an absorption coefficient $\alpha_a \approx 0.6 \text{ cm}^{-1}$ in agreement with published values and other measurements. For a crystal length of about 8 mm, the ratio $P_{\text{abs}}/P_{\text{inc}}$ of the absorbed pump power to the power incident on the focusing lens was in general on the order of 30%, while about 38% of the power launched into the crystal was absorbed.

All P_{out} vs P_{abs} curves showed a good linearity. This is illustrated in Figures 17 and 18 which show the output power curves of crystals #3 and #1, respectively, using either a 0.5% or 5% transmission output coupler. With crystal #3 (Figure 17), the slope efficiency with the 0.5% output coupler was 10.5%, while the threshold was about 7 mW. As expected, more energy was extracted from the crystal by using a 5% output coupler, which yielded an increased threshold ($\sim 17 \text{ mW}$) but a much larger efficiency of 38%. Crystal #1 yielded even better results (see Figure 18), probably as a result of a slightly better crystal quality (the crystals were cut from a boule which was not necessarily homogeneous) and/or better AR-coatings. This laser was operated with a state-of-the-art threshold of about 5 mW with a 0.5% output coupler, and a record slope efficiency of 43.6% with a 5% output coupler. This result is quite outstanding, especially if one considers that the

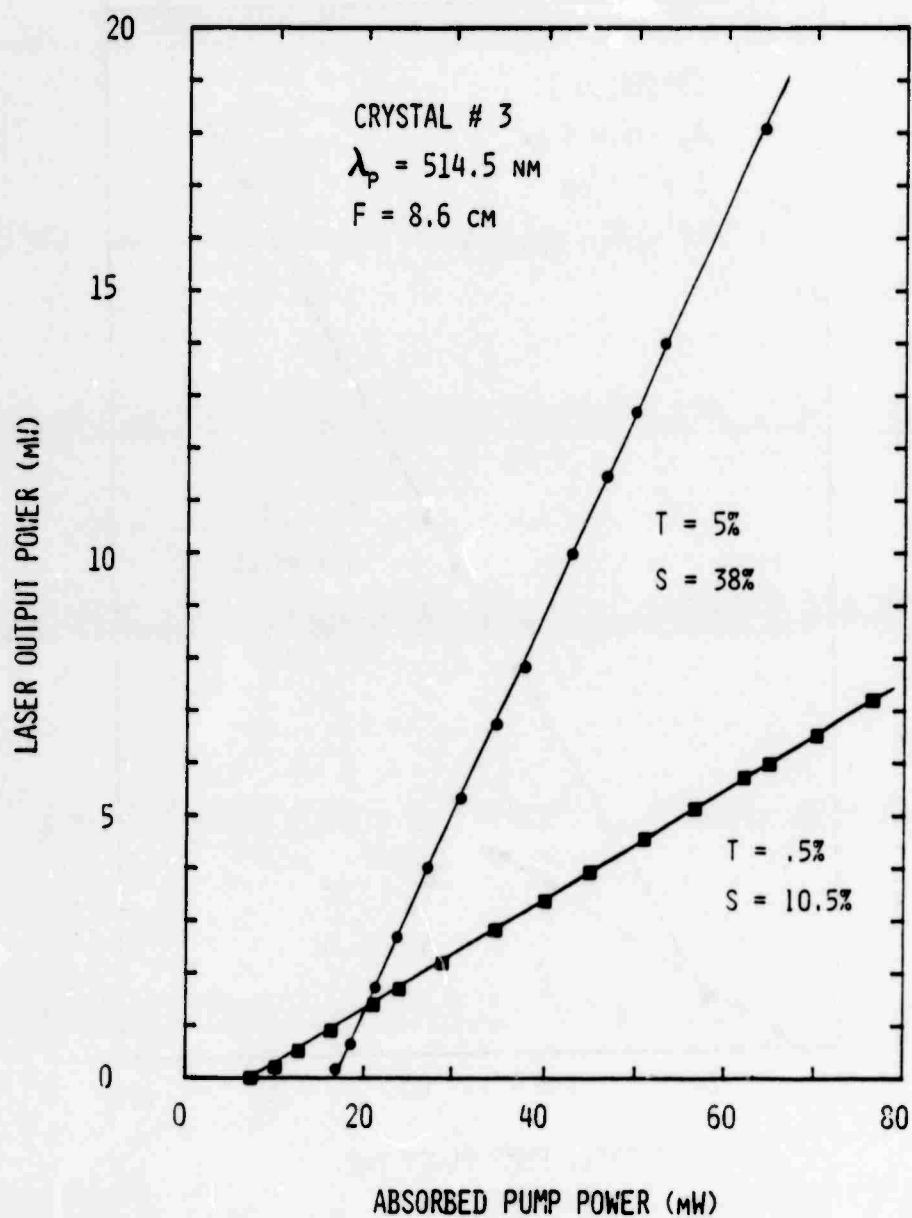


Figure 17--Laser Output Power Versus Absorbed Pump Power in Crystal #3.

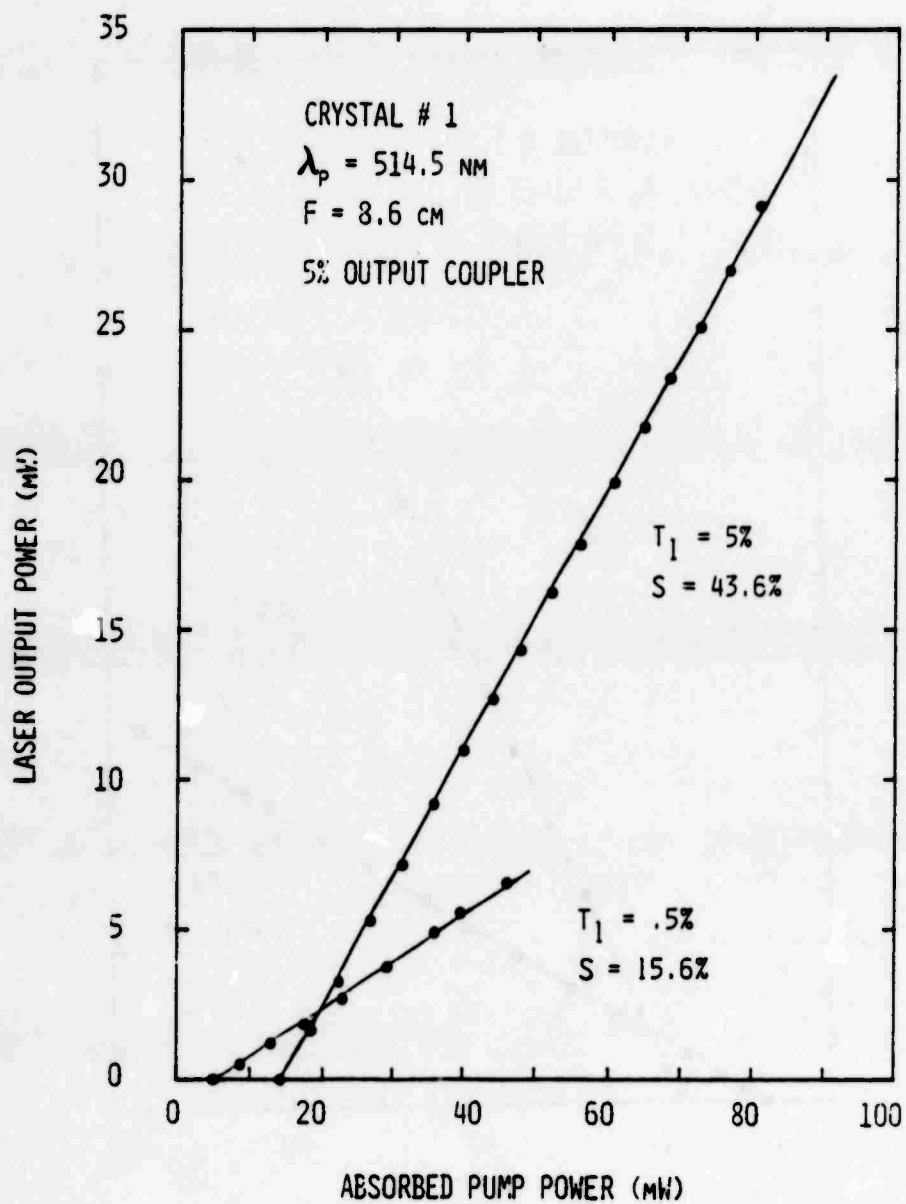


Figure 18--Laser Output Power Versus Absorbed Pump Power in Crystal #1.

absolute maximum theoretical efficiency of this laser, equal to the ratio of signal to pump photon energy (see Eq. 25), is about 48.3%. At the maximum pump power used in this measurement ($P_{\text{abs}} \sim 80 \text{ mW}$) the laser output was nearly 30 mW. The amount of radiation lost to the user was actually quite small - in this configuration, about 9 out of 10 pump photons absorbed in excess of the threshold were actually turned into output signal photons. We should also point out that this result is all the more remarkable in that no special precaution was taken to cool the laser.

Under the above conditions, short term output stability (seconds) was quite good, on the order of 0.5% to 1%. Long term stability (minutes) was 5 to 10%. It was noted that longer focal length lenses gave more stable outputs, probably as a result of a lowered pump beam wander inside the cavity. A focal length on the order of 12 cm was found to be a good compromise between efficiency ($\sim 9.5\%$) with $T_1 = .5\%$ and stability (a few percent over tens of minutes). The residual output power drift was attributed to a gradual misalignment of the cavity (the output could always be brought back to its initial value by tweaking the mirrors).

We summarize in TABLE 5 the results obtained from crystals #1 and #3 presented above. Slope efficiency and threshold pump power are measured values. The total round-trip cavity and crystal loss and A_p^* are calculated from these values, as described below.

Interpretation of laser output power measurements were routinely done using the theory developed in SECTION III-C. From Eq. (25), where $\eta_p \approx 1$, the slope efficiency s is

$$s = \frac{T_1}{\delta_0} \cdot \frac{h\nu_s}{h\nu_p} \quad (50)$$

TABLE 5
SUMMARY OF LASER PERFORMANCE FOR TWO Nd:YAG CRYSTALS
PUMPED AT $\lambda_p = .5145 \mu\text{m}$

CRYSTAL	T_1	SLOPE EFFICIENCY	THRESHOLD	ROUND-TRIP CAVITY LOSS	ROUND-TRIP CRYSTAL LOSS	A_p^* ($\times 10^5 \text{cm}^2$)
#3	.5%	10.4%	7.4 mW	2.3%	1.7%	8.9
	5%	38.3%	17.0 mW	6.3%	1.2%	7.5
#1	.5%	15.6%	5.0 mW	1.6%	1.0%	8.7
	5%	43.6%	14.4 mW	5.6%	0.5%	7.1

From the knowledge of T_1 and s (and $h\nu_s/h\nu_p = .483$), the round-trip cavity loss δ_0 can easily be calculated. The residual crystal loss due to other mechanisms than mirror output coupling is then simply

$$\delta_1 = \delta_0 - T_1 - T_2 \quad . \quad (51)$$

In the conditions of the above measurements, T_2 was measured to be .1%. The calculated round-trip crystal loss δ_1 was $1.4\% \pm .3\%$ for crystal #3, and $0.75\% \pm .25\%$ for crystal #1. These measured crystal loss values include the spurious reflectivity of the AR-coated crystal end-faces. To estimate the relative importance of the two main cavity loss mechanisms, i.e., AR-coating and actual propagation loss in the crystal, the reflectivity of each AR-coating was measured individually. This was done simply by measuring the amount of light reflected by each coated surface. The focused beam of a cw Nd:YAG laser was used near normal incidence in these measurements. For example, for crystal #3 we found .37% and .49% respectively, with an error of about 30% on these values. The round-trip Fresnel loss is thus about 1.7% ($\pm .5\%$). Propagation through the crystal therefore accounts for a negligible fraction of the residual cavity loss. Similar results were obtained for crystal #1. This result attests to the good quality of the crystals. It also shows that the difference in performance of crystals #1 and #3 is mainly due to differences in the state of their end surfaces and not in crystal quality. Note that an upper bound of the respective crystal loss coefficient α_s can be estimated assuming perfect AR-coatings. We then find $\alpha_s \approx .009 \text{ cm}^{-1}$ (crystal #3) and $\alpha_s \approx .005 \text{ cm}^{-1}$ (crystal #1), consistent with the generally recognized value of $\sim .002 \text{ cm}^{-1}$ for the residual bulk scattering coefficient of the best Nd:YAG crystals (Reference 15).

Another aspect of these measurements of interest to the understanding of this type of laser interaction is the degree of overlap between the signal and pump modes. As shown in SECTION III-B , it affects the laser threshold through the effective pump mode area A_p^* [Eq. (14)]

$$P_{th} = \frac{\delta_0}{2} \frac{A_p^*}{\kappa} \quad (52)$$

where $\kappa = \sigma \tau_f / h \nu_p$ is a constant of the material and of the pump wavelength. Measurement of the slope efficiency gives δ_0 as described above, while the measurement of P_{th} and the knowledge of the constant κ gives the value A_p^* from Eq. (52). This first value can then be compared with the theoretical prediction from individual measurements of the pump and signal mode waist radii w_p and w_s [Eq. (36)]

$$A_p^* = \frac{\pi}{2} (w_p^2 + w_s^2) \quad (53)$$

For example, in the case of the measurements summarized in TABLE 5, the cavity waist radius, calculated from cavity parameters, is $w_s = 64.5 \mu m$, or $\bar{w}_s = 65.5 \mu m$ [Eq. (33)]. The pump mode waist radius, calculated for the argon-ion laser beam parameters and a focal length $f = 86 \text{ mm}$, is $w_p = 18 \mu m$, or $\bar{w}_p = 29 \mu m$. Experimental values of w_p obtained by measurement of the far field mode profile with a linear diode array agreed well with the calculated value. This yields a theoretical value of A_p^* [Eq. (53)] of $A_p^* = 8.06 \times 10^{-5} \text{ cm}^2$. Values of A_p^* inferred from laser output measurements are summarized in TABLE 5. Note that the agreement is quite good between experimental and theoretical values.

A note should be added at this point concerning the value of the stimulated emission cross section σ of Nd:YAG at 1.064 μm . Even though this material has been extensively studied, the published values of its cross section σ vary widely, from $2.7 \times 10^{-19} \text{cm}^2$ to $8.8 \times 10^{-19} \text{cm}^2$.⁽¹⁵⁾ The original value of $\sigma = 8.8 \times 10^{-19} \text{cm}^2$ that we used in the beginning of this work is definitely not consistent with our own measurements. In fact, during our work on both Nd:YAG fiber and bulk crystal lasers, we found that the value of $2.3 \times 10^{-19} \text{cm}^2$ agreed consistently well with our observations. We shall therefore use this value throughout this report. This result is not necessarily in disagreement with published results. Several factors enter in the value of σ for an actual Nd:YAG, such as the exact laser line or combination of lines tested, the fluorescence efficiency of the 1.06 μm transition group ($\eta \approx 0.63$), as well as less obvious parameters such as the crystal doping and quality. The scatter in the reported values of σ may actually reflect the variety of experimental conditions and definitions used by different authors.

(c) Transverse Mode Structure

The transverse mode structure of miniature Nd:YAG lasers was routinely observed during laser operation and characterization by observing the magnified image of the laser output beam with a visible-infrared camera. When the laser cavity was aligned for minimum threshold and the pump power increased, the laser was found to oscillate in the fundamental mode up to the highest tested pump power levels. In other words, when the pump and signal modes were very nearly coaxial, mode selection was such that it precluded oscillation of any other mode. This was true in particular during the measurements on crystals #1 and #3 reported in the previous section. Even though they were pumped as high as 17

times above threshold in some cases, single mode TEM_{00} output was always observed.

Miniature Nd:YAG lasers were also operated with higher order modes. Preferential excitation of TEM_{nm} modes was done either by tilting one of the cavity mirrors, or better yet by offsetting the pump beam laterally (i.e. moving the entire cavity perpendicularly to the stationary incoming pump beam). In the first case a higher loss was induced for lower order modes, while in the second case a higher gain was induced for higher order modes, as described earlier (see SECTION III-C). We show in Figure 19 pictures of some of the modes that were observed with crystal #3 ($T_1 = 1\%$), taken directly on the TV screen. The irregularities in the mode shapes are artifacts due to inhomogeneities in the camera sensitive area. At 1.6 mW of output power TEM_{on} modes could oscillate up to $n = 15$, and TEM_{mn} up to $m = n = 5$. Apparently, mode selection was such that at the pump levels at which the laser was operated, the output was always in a single transverse mode.

(d) Mode Overlap Measurements

To verify the validity of our overlap theory, and to determine the best operating conditions of our experimental lasers, it was interesting to analyze the dependence of the laser threshold and slope efficiency on the degree of overlap between the pump and the signal modes. For this purpose one of the lasers (crystal #3) was characterized with different pump waist radii w_p (all other parameters being kept constant) by focusing the pump beam with different lenses. In each case the absorbed pump power at threshold (P_{th}) was measured, as well as the slope efficiency (s).

Figure 20 shows experimental results obtained with focal lengths ranging from 45 to 265 cm. The pump waist radii w_p were calculated from the knowledge

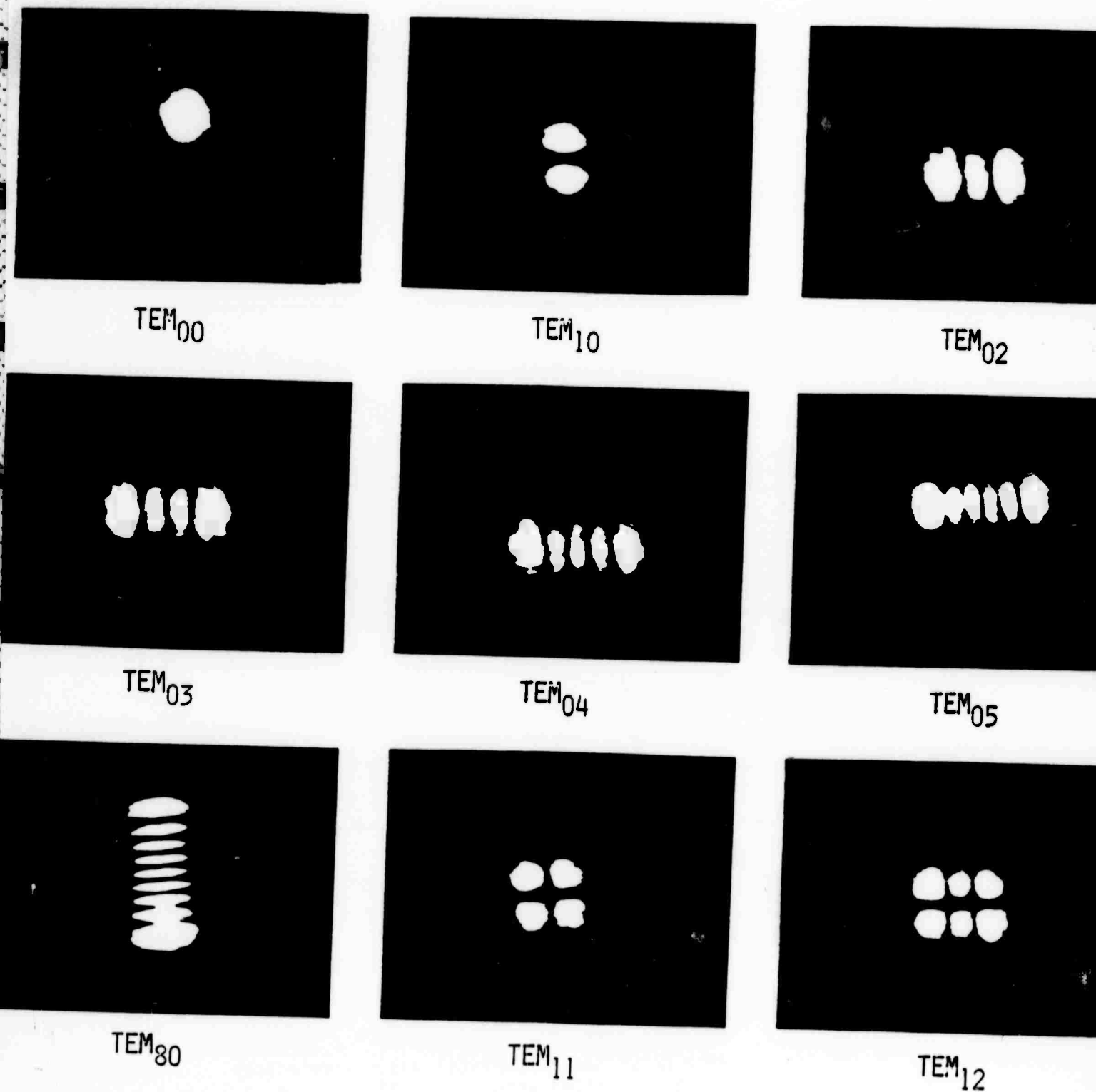


Figure 19--Photographs of a Few of the Transverse Modes Observed in Miniature Nd:YAG Lasers (Crystal #3).

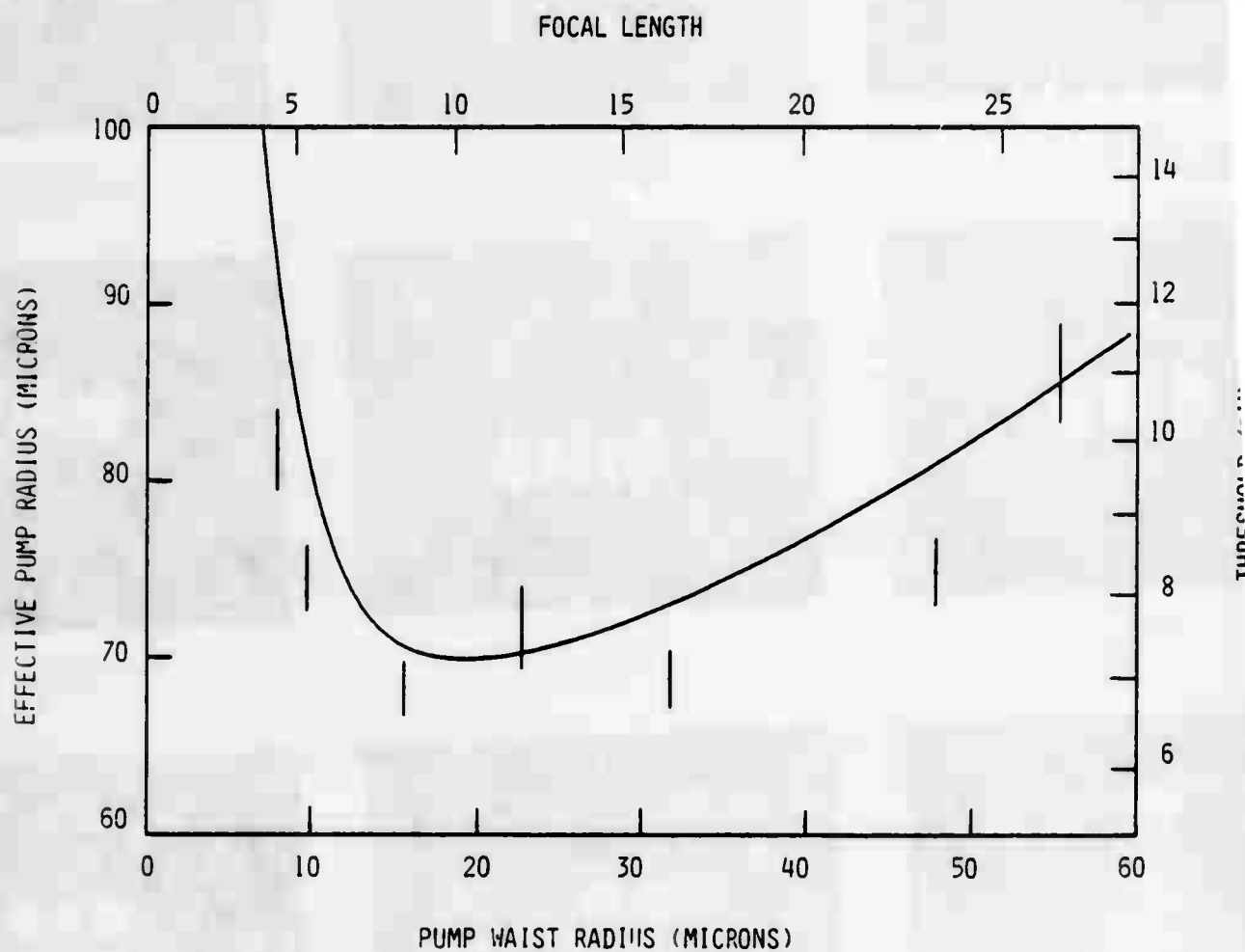


Figure 20--Experimental Verification of the Dependence of the Threshold of a Miniature Nd:YAG Laser on the Pump Waist Radius (Crystal #3). Theoretical Curve was fitted with $\delta_0 = .026$ and $W_s = 64.5 \mu\text{m}$.

of the argon laser cavity parameters and the distance from the argon laser to the focusing lens. The solid curve is the theoretical prediction derived from the analytical results presented in SECTION III-B using the exact overlap expression [Eq. (12)], and a round-trip cavity loss of $\delta_0 = .026$. Agreement between experimental and theoretical results is excellent. The slight tendency of our results to be lower than the theoretical prediction is either due to an underestimation of the round-trip loss or of the measured threshold. In any case the average discrepancy in w_p^* between theory and experiment is less than $4.5 \mu\text{m}$, or about 5%, which can be considered a good fit. The laser threshold presents a minimum (and the laser gain a maximum) which occurs, as predicted by the theory, when the average pump beam spot size along the interaction region is minimum. This was achieved in our experimental arrangement with a focal length $f = 86 \text{ mm}$, which was used throughout our measurements on miniature lasers (since they all had approximately the same length).

In Figure 21 we show the dependence of the slope efficiency on the pump waist radius of the same laser (measured with the threshold simultaneously). Again the measured data agree well with the theory. When the pump beam is focused either too tightly or too loosely, the region in which population inversion is created is not well matched to the signal mode, and a significant fraction of the inverted population does not contribute to the stimulated emission of photons. The range of pump waist radii which nearly optimizes the slope efficiency is, however, relatively broad, from $10 \mu\text{m}$ to $50 \mu\text{m}$ in the present example. The fact that the efficiency drops more rapidly in our measurements than predicted is probably due to a more difficult alignment of the pump and signal beam axis when using shorter focal length lenses. Also, in the tight-focusing configuration, \bar{w}_p (and δ_0) depend very strongly on w_p

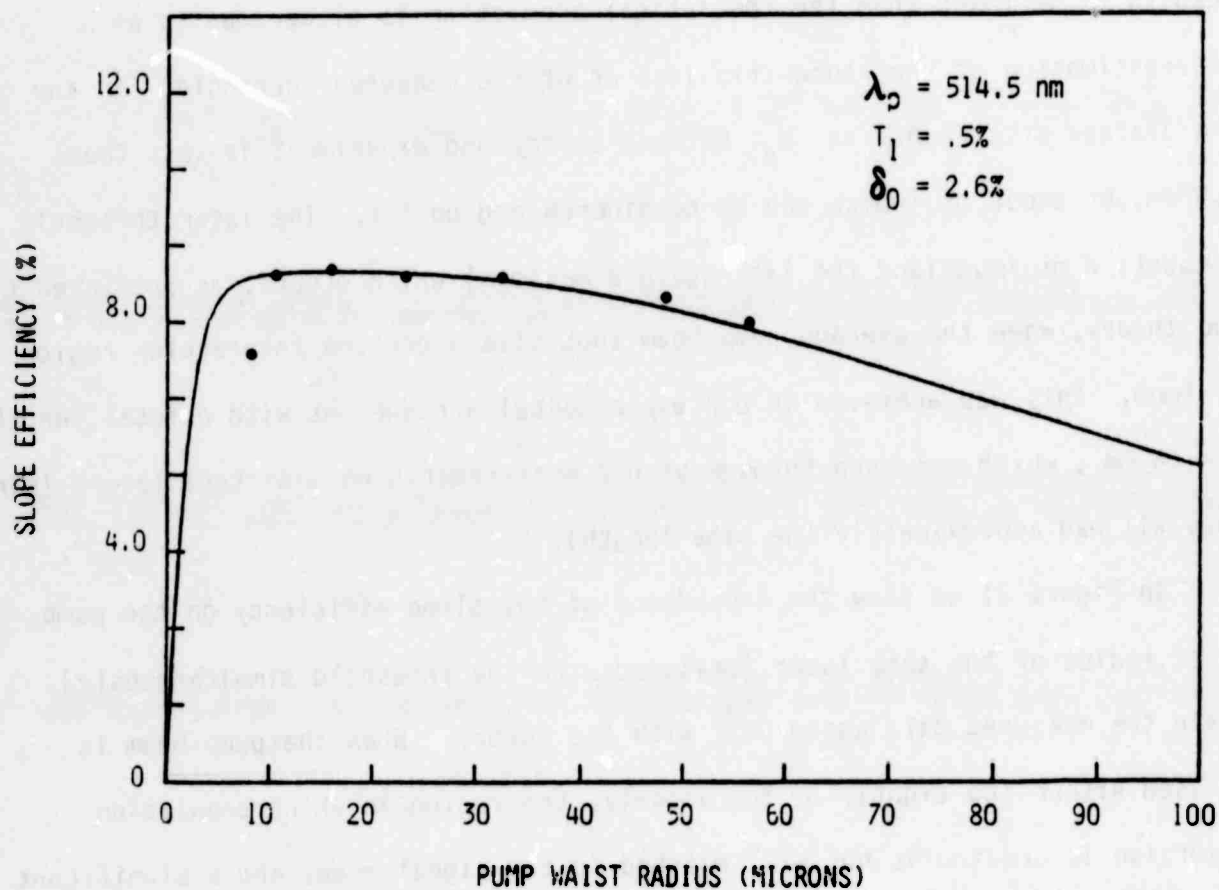


Figure 21--Experimental Verification of the Dependence of the Slope Efficiency of a Miniature Nd:YAG Laser on the Pump Waist Radius (Crystal #3). The fitting Parameters are the same as in Figure 20.

(W_p^{-3} law) and on the location of the waist with respect to the crystal, two parameters which are not very accurately known.

B. FIBER LASERS

1. Experimental Arrangement

Work on Nd:YAG fiber lasers pumped at $0.5145 \mu\text{m}$ was a direct continuation of the analysis of Nd:YAG bulk lasers reported above, and presented a number of similarities in experimental arrangement and methods. The fibers used in all of our measurements had their ends polished by the method described in SECTION II-C, in which a number of fibers with similar diameters were bonded in a slotted Nd:YAG cylindrical holder. To take advantage of the ruggedness of this configuration the fibers were made into lasers as is, i.e., without removing them from the polishing holder. To eliminate Fresnel end reflections, some fiber arrays were anti-reflection coated. In such cases in-house facilities were used to deposit so-called soft coatings directly on the ends of the holder. They present the advantage of not requiring a high-vacuum, precluded by the epoxy which normally out-gases. AR-coatings were thus simple quarter wave plates of magnesium fluoride (MgF_2) approximately 1970 \AA thick. Theoretical investigations show that the tolerance on the coating thickness or uniformity for a spurious reflection smaller than .1% is about $\pm 260 \text{ \AA}$. This was relatively easy to achieve without a wavelength monitor, as shown by direct measurements as well as subsequent laser measurements, which both indicated spurious Fresnel power reflections of .1% to .5%.

A total of 16 fiber arrays, or over 120 fibers, were thus processed for laser evaluation and related measurements under this program. For easy reference these arrays, numbered 1 through 16, are listed in TABLE 6. This table also lists the (approximate) fiber diameters and lengths, the number of fibers per

array, as well as other characteristics. In a given array fibers were numbered starting from the bottom of the slot, so that a given fiber is referred to by a double number, such as #4-2, in which the first number refers to the array and the second one to the fiber.

Arrays #1, 2 and 7 were fabricated for extensive laser characterization. Arrays #5 and 10 were purposely polished into thin slabs for index profile measurements. Arrays #3 and 4, fabricated in two slots in the same holder, were originally designed to be long enough that their aspect ratio would prohibit propagation of a free-space mode. After laser tests they were cut transversely for further laser measurements, becoming arrays #11 through 14. A few high-index clad fibers were mounted in array #8 for polishing and optical measurements performed under another program. Array #15 was prepared one step further as all fibers were removed from the holder after polishing for fiber laser miniaturization. Array #16 was fabricated to perform a series of new polishing tests. Finally a few arrays (#4, 9, 12, and 14) were fabricated with fibers provided to us by Bell Telephone Laboratories a few years ago, and were used to measure the optical properties of Nd:YAG fibers from another source.

The optical cavity used for the evaluation of fiber lasers pumped at $0.5145 \mu\text{m}$ is shown in Figure 22. The new arrangement presented only minor modifications from the one used before. Miniature mirrors with dimensions $2 \times 2 \times 5 \text{ mm}$ were used with a view toward further miniaturization as well as to keep the cost down. Each mirror was lightly bonded on a small bored cylinder that was mounted on the tilt stage. A variety of such mirrors was available, with transmissions $T = 0\%$ (HR), 1% and 5% , flat curvature ($R = \infty$), in sizes ranging from 2×2 to $4 \times 4 \text{ mm}$, and in approximate quantities of 20 each (Reference 18).

TABLE 6
LIST OF FIBER ARRAYS AND CHARACTERISTICS
AS AVAILABLE AT THE MOMENT

Array #	Length	Average Diameter	Number of Fibers	Comments
1	7.8 mm	100 μ m	11	AR-coated
2	4.0 mm	230 μ m	13	
3	11.8 mm	95 μ m	5	AR-coated
4	11.8 mm	80 μ m	4	AR-coated/BTL fibers
5	.46 mm	80-120 μ m	11	Index profile measurements
6	8 mm	230 μ m	3	Glass holder
7	8 mm	85 μ m	7	AR-coated
8	~ 5 mm	110 μ m	6	Clad fibers
9	5.6 mm	65 μ m	13	BTL fibers
10	~ 0.5 mm	250 μ m	11	Index profile measurements
11	5.3 mm	95 μ m	5	
12	5.3 mm	80 μ m	4	BTL fibers
13	5.5 mm	95 μ m	5	
14	5.5 mm	80 μ m	4	BTL fibers
15	4.0 mm	250 μ m	10	Individual fibers
16	~ 3 mm	250 μ m	10	Polishing tests

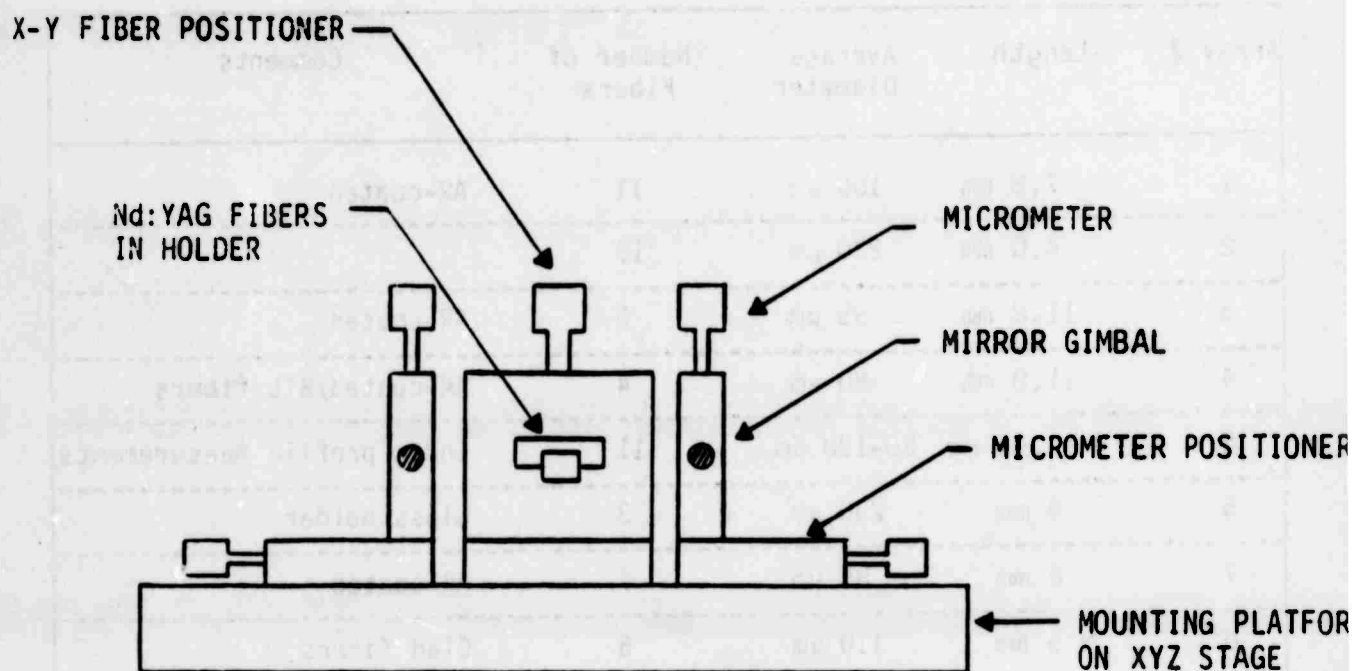


Figure 22--Schematic of the Fiber Laser Cavity.

The Nd:YAG fiber array was held inside the cavity by a miniature X-Y stage which allowed us to position any fiber in the incident pump beam. The pump beam was focused with a single lens and launched into the fiber through the back mirror (high reflector).

Routine alignment of the optical cavity proceeded as follows. The selected fiber was first aligned (tilts and x-y) in the fixed incident pump beam so as to optimize the amount of pump energy confined to the center of the core, as seen at the fiber output end. In the best cases a large fraction of the pump power was in the fundamental mode, the rest of it being scattered in higher order modes. Next the mirrors were aligned as before until a noticeable flickering of the pump beam occurred, before being brought as close to the fiber ends as possible.

2. 100 μ m Diameter Fiber Lasers

A first class of fiber lasers that were extensively studied are lasers with $\sim 100 \mu\text{m}$ diameter, in particular arrays #1 and #7. Laser action was successfully observed in 13 out of the combined 18 fibers of these arrays. However, fiber #1-4 gave by far the best results and was the object of most of the tests on this type of fiber lasers.

Fiber laser #1-4 was tested with a 1% and 5% output coupler. Typical output power curves are shown in Figures 23 and 24. With a 1% output coupler, the maximum observed slope efficiency was 3% for a threshold of oscillation of 5 mW. The best threshold observed with this fiber was remarkably low, on the order of 2.6 mW. With a 5% output coupler, the slope efficiency was up to 15%, and the maximum output power observed was in excess of 10 mW for 80 mW of absorbed pump power. Observed threshold with a 5% output coupler was as low as 7 mW.

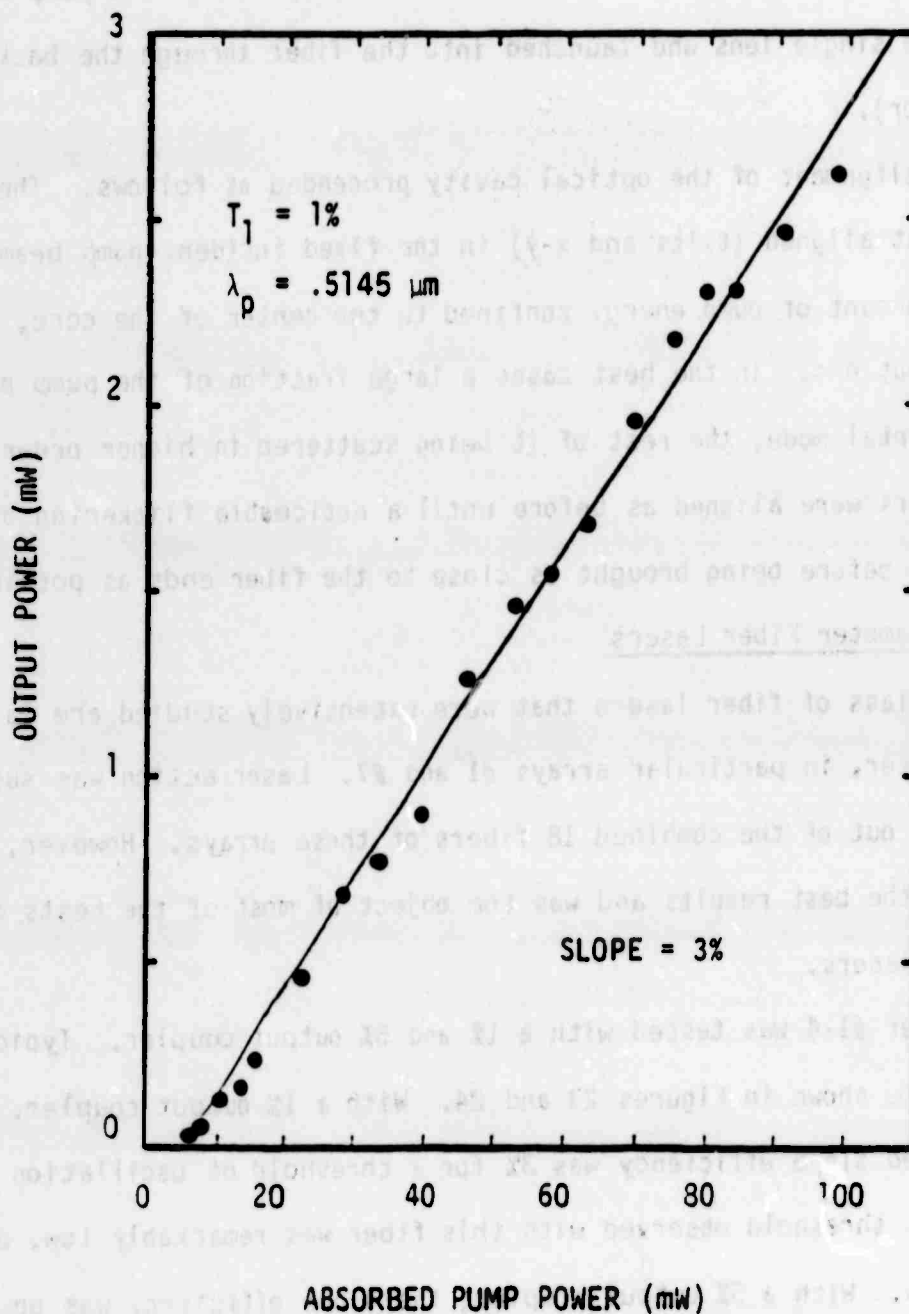


Figure 23--Output Power Versus Absorbed Pump Power for Fiber #1-4 ($T_1 = 1\%$).

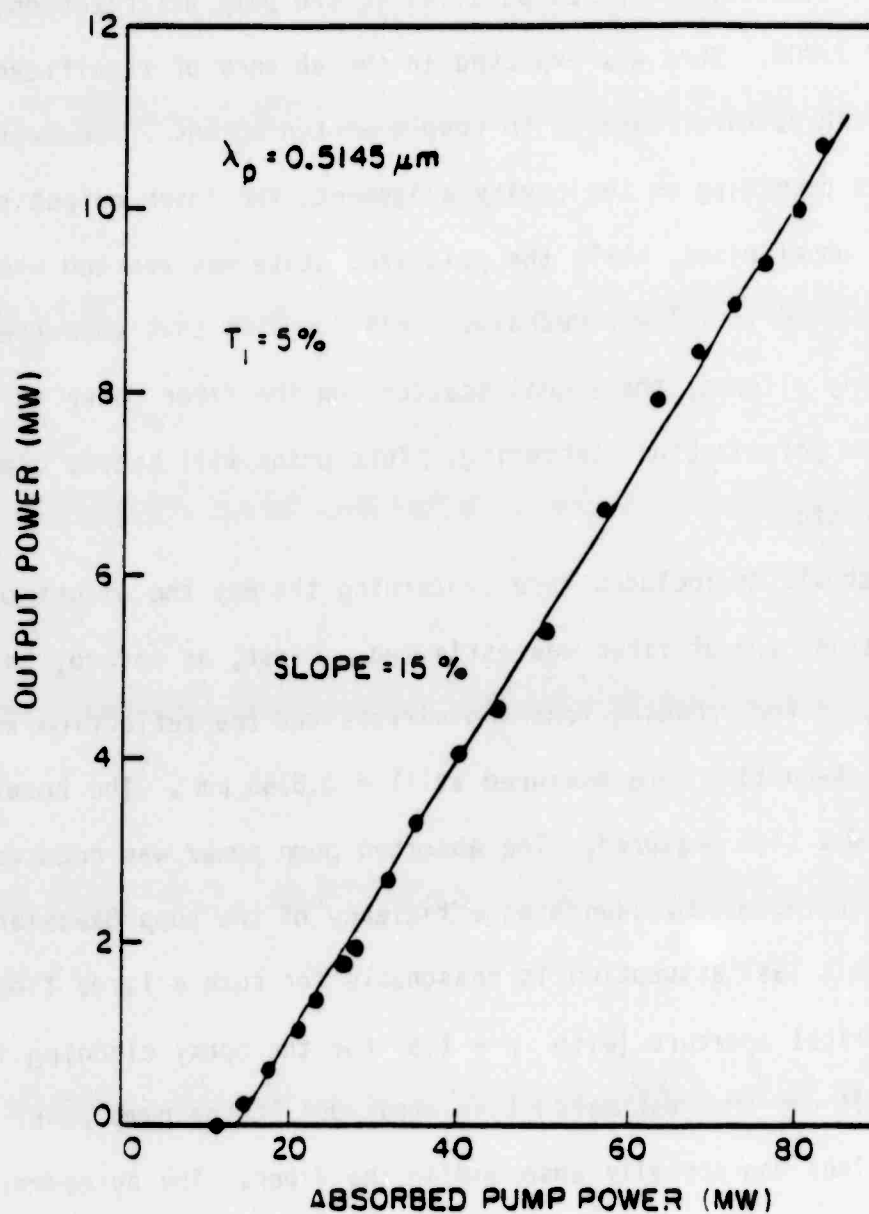


Figure 24--Output Power versus Absorbed Pump Power for Fiber #1-4 ($T_1 = 5\%$).

In both sets of measurements the output signal was in the fundamental single transverse mode even at the highest tested pump power levels. The signal output mode was also linearly polarized parallel to the pump polarization, up to linearity of 1:200. This was expected in the absence of significant anisotropic mechanisms such as birefringence to couple photon momenta. However, it was also observed that depending on the cavity alignment, the laser output could be either polarized or unpolarized, while the polarized state was reached when the laser cavity was aligned to a low threshold. This suggests that when the fiber laser is not properly aligned, the signal scatters on the fiber outer surface and suffers random polarization scattering. This point will become clearer after further discussion.

A note should be included here concerning the way the amount of pump power absorbed by this type of fiber was estimated. First, as before, the transmissions of the focusing lens and mirrors and the reflection coefficients of the 1.064 μm AR-coating were measured at $\lambda = 0.5145 \mu\text{m}$. The total system transmission was then measured. The absorbed pump power was deduced from the above data assuming a 100% launching efficiency of the pump Gaussian mode into the fiber. This last assumption is reasonable for such a large fiber diameter and high numerical aperture (with $n \approx 1.5$ for the epoxy cladding index, $NA \approx 1.0$). It was thus estimated that about 30% of the pump power incident on the focusing lens was actually absorbed in the fiber. The agreement with our earlier measurements in bulk Nd:YAG crystals of similar length indicates an absorption coefficient of Nd:YAG fibers of $\sim .6 \text{ cm}^{-1}$ at 0.5145 μm , as confirmed by individual fiber transmission measurements.

The tolerance on the alignment of the mirror tilts and of the fiber lateral position was found to be quite easy to satisfy. The mirror-to-fiber end spacing

was also not very critical. For this type of fiber laser, a spacing of up to 200-300 μm on both fiber sides resulted in only a slight ($\sim 10\text{-}20\%$) increase in the threshold, in agreement with theoretical predictions (see Section VI-A-4). As expected, this spacing was more critical with smaller diameter fibers. On the other hand, the tolerance on the tilt of the fiber with respect to the incident pump beam seemed relatively demanding. As the tilt angle needs to be finely adjusted to achieve efficient launching of low order pump modes, this observation reflects our theoretical result: low order pump modes yield an overall gain factor up to twice as large as a high order mode distribution.

Again we found that although the cavity was not designed for optimum stability and involved a fair number of inherently unstable translation stages, the output of fiber lasers was remarkably stable - definitely better than commercial cw Nd:YAG lasers. The fact that our fiber lasers were run uncooled and were not allowed to develop any significant temperature gradient probably accounts for this improvement. The main source of instability was found to originate from pump feedback into the argon-ion laser from spurious back reflections. As the fiber laser could not be tilted without introducing a misalignment which would preclude efficient pump and signal overlap, this difficulty was cured by placing an optical isolator between the pump laser and the fiber laser. Short-term output power stability was then on the order of a few percent, as attested by the good linearity of the output curves (see Figures 23 and 24) which took, in general, 5 to 10 minutes to record.

The laser measurements (s and P_{th}) done on fiber #1-4 suggest, using Eqs. (50) and (52), a round-trip cavity loss on the order of 10 - 15%, and an effective pump mode area of about $1\text{-}2 \times 10^{-5} \text{cm}^2$. The scatter in the many measurements done with this or any other fiber reflects the relative difficulty

in aligning the cavity to its lowest threshold. As mentioned above, the relative fiber-to-pump beam tilt was rather critical and difficult to reproduce. In any case a first conclusion is that the round-trip fiber laser loss is somewhat larger than that of bulk crystal lasers. Secondly, although the same optics as before were used to focus the pump ($f = 86 \text{ mm}$), A_p^* appeared to be always smaller in fibers than in bulk crystals. This observation suggests a higher signal mode confinement in fibers, and therefore a higher gain per unit absorbed pump power, by as much as a factor of 4 to 10.

To verify this observation, and to analyze the quality of the signal mode generated by fiber lasers, the mode structures of both pump and signal fiber outputs were investigated. Far-field profiles were measured with a mechanically-scanned apertured ($\lesssim 500 \text{ }\mu\text{m}$) detector, and were automatically plotted on a time-base chart recorder. Near-field profiles were obtained by imaging the end of the fiber on a linear 500 element Reticon diode array ($12 \text{ }\mu\text{m}$ diode spacing) with a short focal length lens. The ratio of the lens-to-fiber end distance d_1 to the lens-to-detector distance d_2 is the optical magnification factor M (in our measurements, $M \approx 18.5$).

Typical far-field profiles measured for fiber laser 1-4 are shown in Figures 25(a) and 25(b) (concluded) for the pump and the signal, respectively. The mode distributions are very nearly Gaussian. By measuring the mode width at the $1/e^2$ power point for different fiber-to-detector distances, we found that the signal beam was diverging like a diffraction-limited fundamental Gaussian mode of waist at the fiber, $W_s = 25.4 \text{ }\mu\text{m}$. Similar results were obtained with the pump beam, yielding $W_p = 19 \text{ }\mu\text{m}$.

Near-field profiles are shown in Figures 26(a) and 26(b) (concluded) (pump and signal, respectively). The recollimated signal beam is particularly clean,

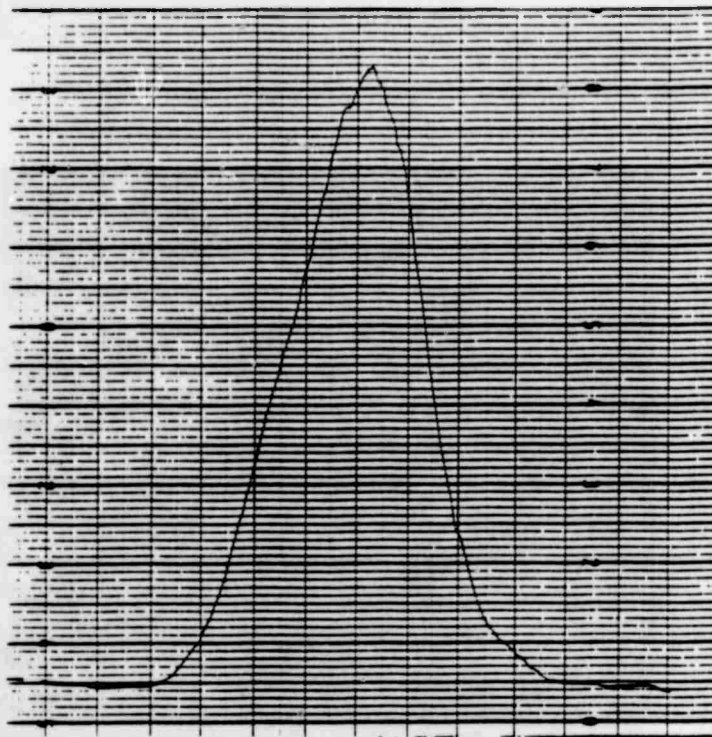


Figure 25(a)--Far-Field Profile of the Fundamental Pump Mode ($.5145 \mu\text{m}$, Fiber #1-4).

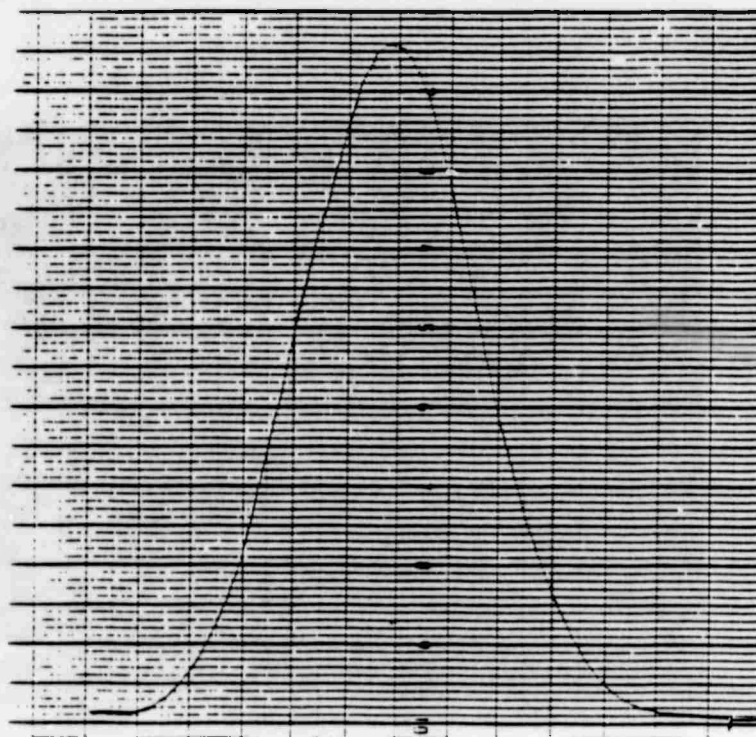


Figure 25(b)--Far Field Profile of the Fiber Signal Output Mode ($1.064 \mu\text{m}$, Fiber #1-4).

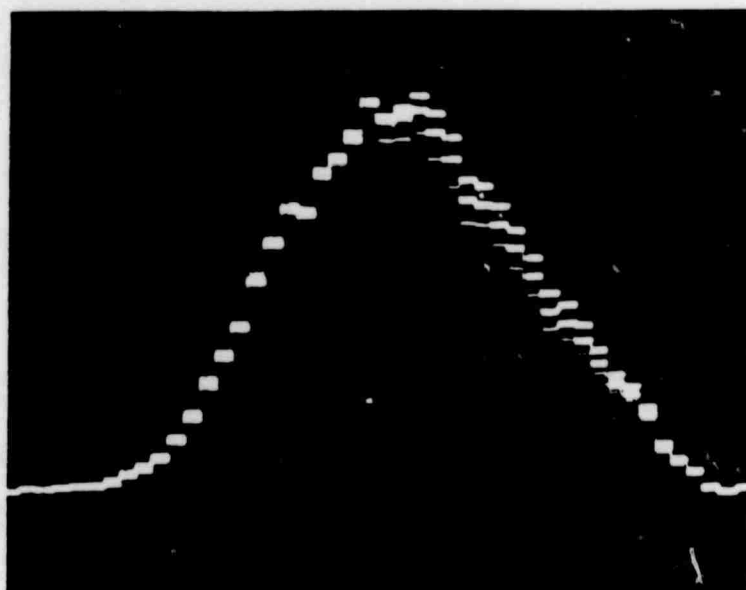


Figure 26(a)--Near-Field Profile of the Fundamental Pump Mode ($.5145 \mu\text{m}$, Fiber #1-4).

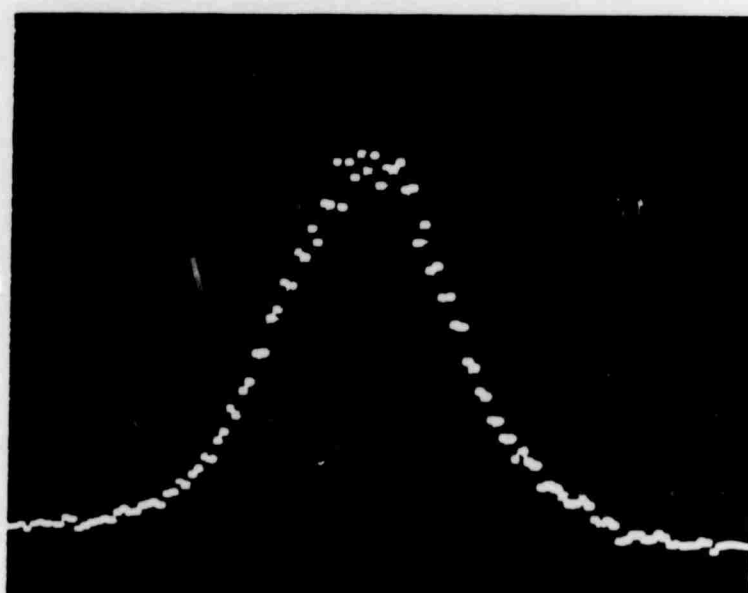


Figure 26(b)--Near-Field Profile of the Fiber Signal Output Mode ($1.064 \mu\text{m}$, Fiber #1-4).

so that although such measurements were not performed, we believe a significant fraction of the mode could be coupled into a single mode fiber, or focused to a small diffraction-limited spot size (the slight double-image effect is only due to the series of filters used to isolate the signal from the pump). Average values computed from several measurements are $W_s = 19.7 \mu\text{m}$ for the signal and $W_p = 21.3 \mu\text{m}$ for the pump.

These two sets of results agree well although we believe the far-field measurements, which do not involve any optics, are more accurate. They indicate a pump waist of approximately $19 \mu\text{m}$ identical to the previously calculated value of W_p for this pumping arrangement. The pump beam was therefore not guided by the fiber laser, although some degree of aperturing at the input and/or output end of the fiber may have been present. The situation is different for the signal. Assuming the signal mode was guided by the fiber, this value corresponds to a fiber core radius of $a = W_s/.645 = 39.4 \mu\text{m}$. (This last relationship was derived using a computer model of mode coupling between a guided LP_{01} mode and a fundamental space Gaussian mode, and agrees well with published data (Reference 17)). This result is compatible with the value of the fiber diameter measured for fiber #1-4, which ranges at least from $86 \mu\text{m}$ to $130 \mu\text{m}$. As expected the smaller portion of the fiber imposes its size to the signal mode. These results clearly indicate that at least in fiber laser #1-4 mode confinement is provided by the finite transverse size of the fiber. Note that since within the fiber the signal mode is very nearly Gaussian with a constant waist radius, we can use the Gaussian mode overlap theory of SECTION III-C to estimate A_p^* . With $W_s = \bar{W}_s \sim 25 \mu\text{m}$, $W_p \sim 19 \mu\text{m}$ and $L \sim 8 \text{ mm}$, we find $h_p^T \sim 25 \mu\text{m}$ and $A_p^* = 2.0 \times 10^{-5} \text{ cm}^2$, in excellent agreement with the value inferred from threshold measurements ($1-2 \times 10^{-5} \text{ cm}^2$).

These conclusions were confirmed by further laser measurements on the other fibers of array #1. Laser action was successfully observed in 10 out of the 11 fibers of this array. Each laser measurement was preceded by a careful tilt alignment of each individual fiber until the cleanest possible fundamental output pump mode was observed. All fibers but #5 displayed a fairly nice fundamental pump output mode. TABLE 7 summarizes measurements done on these fiber lasers with $T = 1\%$. Five fibers were operated with thresholds below 10 mW, of which three were lased with less than 5 mW. The best results were obtained with fibers #1 and #4, which yielded thresholds on the order of 3 mW only. These thresholds were measured by observing the fiber laser output extinction with an infrared camera and video monitor, so that these figures may differ in some cases from the threshold extrapolated from output power versus pump power curves (see Figures 23 and 24). The amount of pump power absorbed by each fiber was estimated from individual measurements of fiber transmission and discrete optical element losses. TABLE 7 also shows the measured fiber transmissions at $.5145 \mu\text{m}$ (corrected for end-face reflections, and assuming 100% coupling efficiency), which again agree well with the generally accepted value of $.6 \text{ cm}^{-1}$ for 1 at.% Nd-doped YAG. Note that this method leads to an overestimation of the absorbed pump power (i.e., a worst threshold) as other mechanisms besides absorption are certainly present. Finally, TABLE 7 also lists the diameter characteristics of fibers of array #1. Fiber diameters were not characterized prior to mounting the fibers. Diameter data were therefore measured at each fiber end, of which ϕ is the average value, and $\Delta\phi/\phi$ the relative difference.

A first conclusion of these tests is that all fibers do not display the same loss characteristics, as reflected by the wide range of thresholds and transmissions. A definite correlation exists between fiber transmission and

TABLE 7
MEASURED DATA FOR FIBER LASERS OF ARRAY #1

Fiber #	ϕ (μm)	$\Delta\phi/\phi$	Transmission ($\lambda = .5145 \mu\text{m}$)	P_{th} (mW)
1-1	97	20.3%	.67	3.20
1-2	95	17.4%	.73	11.3
1-3	101	19.2%	.66	16.2
1-4	110	37.2%	.67	2.6
1-5	91	20.5%	< .30	
1-6	94	11.2%	.67	4.0
1-7	91	46.9%	.46	72.3
1-8	92	27.8%	.72	6.4
1-9	94	22.6%	.60	40.7
1-10	96	13.0%	.65	9.0
1-11	91	20.9%	.62	36.0

laser threshold, as illustrated in Figure 27. In this figure the threshold is plotted versus the overall loss coefficient α_s for the fibers of array #1. The loss coefficients are computed from $T = \exp(-\alpha_s L)$ with $L = 7.7$ mm, and include the absorption coefficient α_a . Fibers with the lowest transmissions have the highest thresholds. Visual inspection of the fiber under a microscope or of the quality of the pump mode transmitted by the fiber also provided a clear indication of the best fiber samples and a prediction of the best fiber lasers. For example fibers #5 and #7 appeared more optically opaque (at visible frequencies) than the other fibers, while the transmitted pump beam was scattered into several modes at the fiber output. As expected, these two fibers display the highest thresholds. Another correlation was observed between threshold and diameter variations, as shown in Figure 28, or equivalently, between fiber transmission and diameter variations. The fibers with the largest diameter fluctuations display the highest propagation loss.

These observations give additional weight to our initial conclusions concerning the confinement mechanism involved in fiber #1-4. Since flat mirrors were used, some mechanism other than the focusing effect of the cavity optics had to be responsible for the relatively tight confinement of the signal mode. In fact, an unguided laser with flat mirrors is unstable unless, for example, apertures (such as naturally provided by the fiber) are introduced inside the cavity. This was verified by observing lasing action in bulk Nd:YAG with two flat mirrors. The resulting laser had a very high threshold (~ 100 mW), was very sensitive to mirror adjustment, and provided an odd-shaped mode (laser action was taking place along several optical paths). This behavior is characteristic of unstable resonators. The absence of such characteristics in our fiber lasers indicate the presence of either guiding action or some aperturing effect.

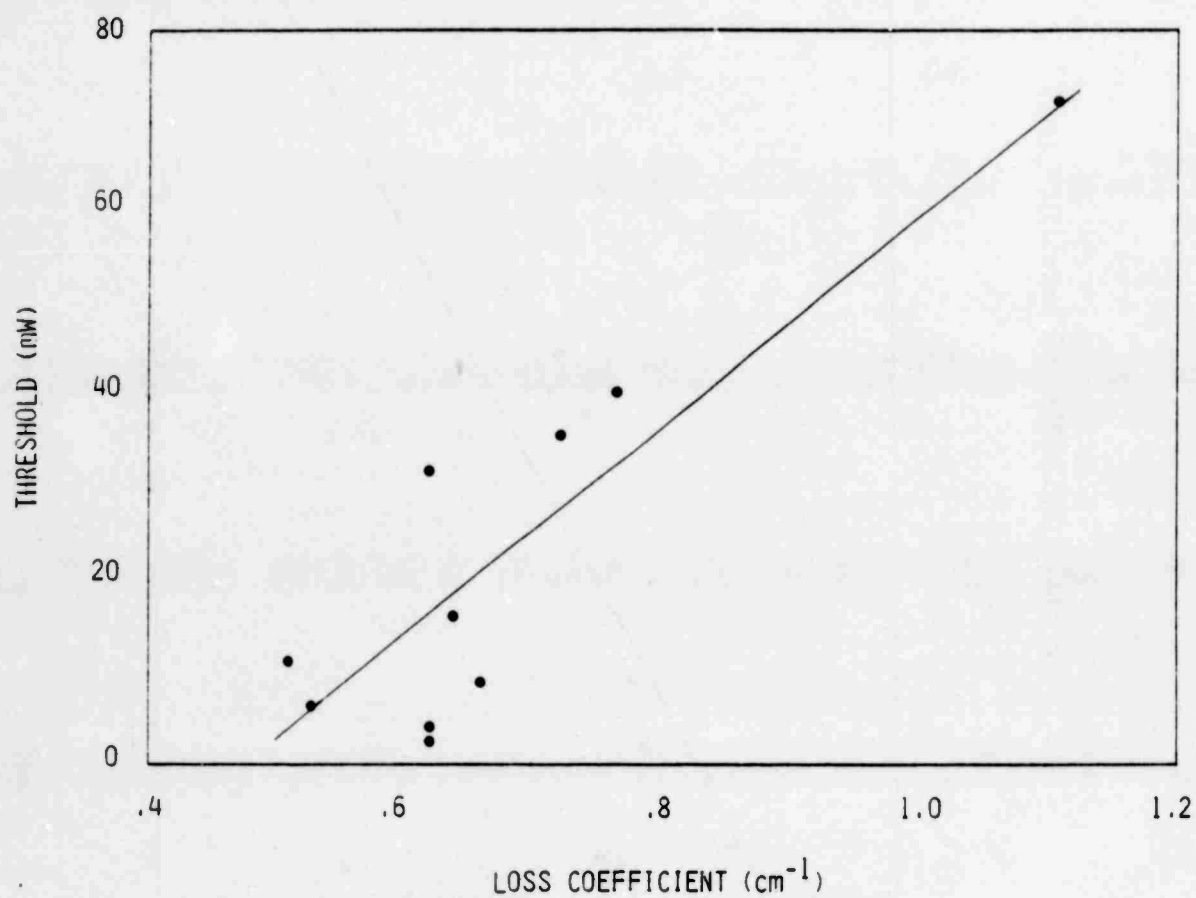


Figure 27--Threshold versus Loss Coefficient
in Fiber Lasers of Array #1.

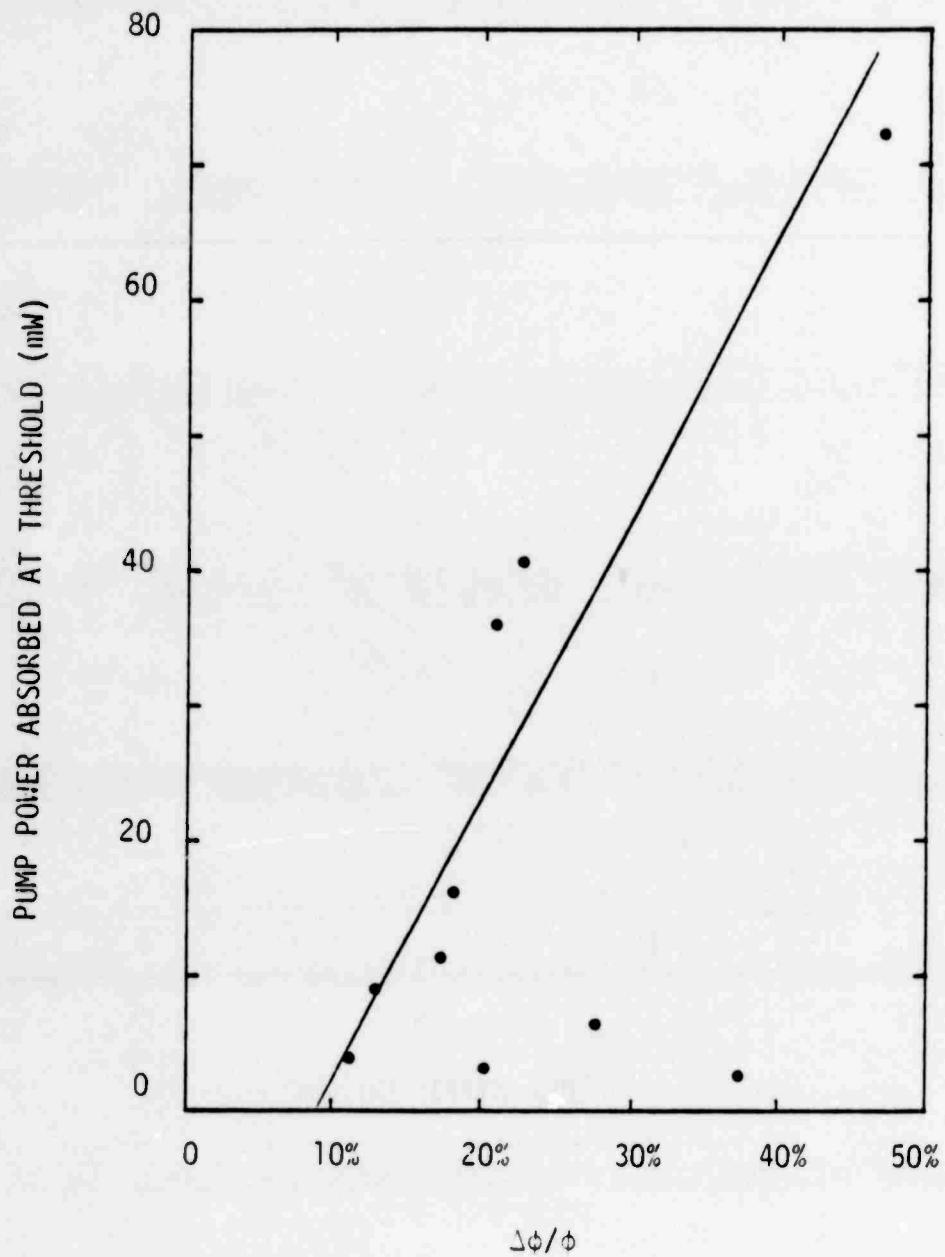


Figure 28--Measured Threshold versus Measured Fiber Diameter Fluctuations for 10 Fiber Lasers (Array #1).

For all the fibers of array #1 the ratio of fiber length to diameter (aspect ratio) is small enough that a Gaussian mode at the signal frequency could indeed propagate through the fiber without being aware of the finite transverse size of the fiber. It was therefore difficult to conclude whether total internal reflection or local aperturing at the smallest section of the fiber was responsible for signal mode confinement. However, it appears clear that aperturing is also responsible for (1) the greater gain per unit pump power available in fiber lasers, (2) the increase in cavity loss observed in fiber lasers, and (3) the consistent oscillation of all tested fiber lasers on the fundamental mode exclusively, regardless of the pump or cavity configuration, as higher order modes experience higher loss. The fact that the fiber loss is worse in fibers with larger diameter fluctuations also shows that in smaller diameter fibers in which mode confinement is provided by the finite transverse fiber size, it is important to keep diameter variations to a minimum. The relatively important diameter variations of the fibers of array #1 are most probably responsible for the residual cavity loss observed with these fibers.

In TABLE 8 we summarize the results obtained with the fibers of array #7. They include fiber diameter, crystal and polishing quality, fiber tilt with respect to the holder axis, measured oscillation threshold and calculated round-trip loss. All fibers of array #7 were tested for laser performance using the same experimental arrangement (1% output coupler). We found that three of them could be easily brought to oscillation while the other four could not be lased at all. It appears that fiber #7-2 could not be lased because of poor crystal quality (the fiber appeared dark in the microscope). In fibers #7-5, #7-6,

TABLE 8
CHARACTERISTICS OF FIBERS IN ARRAY #7

Fiber #	Diameter (μm)	Tilt Angle	Polish/ Crystal Quality	Threshold (mW)	Round-trip Loss
7-1	78.1	.72°	Slightly Gray	3.8	~ 18%
7-2	80.3	.61°	Dark		
7-3	90.0	.06°	OK	16.0	~ 60%
7-4	86.0	.52°	Two small Chips	4.6	~ 19.5%
7-5	87.3	1.07°	OK		
7-6	87.4	1.58°	One Small Chip		
7-7	85.8	4.2°	OK		

and #7-7 lasing was probably prohibited by unusually large fiber tilts. A large fiber tilt has two effects: (1) it prohibits constructive interference of spurious Fresnel reflections at the fiber ends with the main signal (see next section); (2) it eventually requires mirror tilt angles larger than can be achieved with our gimbal mounts ($\pm 2^\circ$). Apparently, the limit of acceptable tilt (or laser end-face parallelism) is on the order of 1° . As expected, the outermost fibers (furthest from the bottom of the groove) pick up the highest tilt angle during bonding. This suggests the use of less than ideal quality fibers as fillers in future holders. Two of the fibers which lased show near state-of-the-art performance, with thresholds lower than 5 mW. Again a clear correlation was observed between the threshold level and the mode quality of the pump mode at the fiber output.

With a 78 μm diameter fiber #7-1 is the smallest of this type brought to oscillation. Its laser slope efficiency was measured to be 2.6% (with a 1% output coupler). This value suggests a round-trip loss of 18.6%, and combined with an extrapolated threshold of 7 mW, an effective pump mode area $A_p^* = 1.04 \times 10^{-5} \text{ cm}^2$. The signal mode area has a calculated radius of 18 μm in agreement with a theoretical value of $.645 \times a = 25 \mu\text{m}$ (this fiber probably has a slightly smaller diameter somewhere along its length).

Finally, the longitudinal mode structure of $\sim 100 \mu\text{m}$ diameter fiber lasers was analyzed with Fabry-Perot (F.P.) interferometers placed at the laser output. The ring pattern given by the interferometer was observed on a TV-monitor with an infrared camera. With a 1 cm^{-1} free spectral range (FSR) F.P. etalon, we saw that these fiber lasers were running single longitudinal mode at, and near, threshold, and that a second mode was soon appearing above threshold. As the pump power was further increased, a third mode appeared (about twice above

threshold). The mode spacing was measured to be $\Delta\nu \approx .33 \text{ cm}^{-1}$, i.e., exactly $1/3$ of the etalon FSR, compared to a predicted value $\Delta\nu = 1/2 n\lambda$ ($n = 1.82$, $l \approx 8 \text{ mm}$) of $.34 \text{ cm}^{-1}$. The use of a 10 cm^{-1} FSR etalon revealed the presence of 4th and 5th longitudinal modes, previously undetected as they overlapped with the 2nd order rings of the 1st and 2nd mode, respectively. The 4th mode appeared 3 times above threshold, and the 5th one 5 to 10 times above threshold. No more than 5 modes were observed up to the maximum available pump power ($P_{\text{abs}} \sim 180 \text{ mW}$). This result is expected in a homogeneously broadened laser material where in general ~ 5 modes only are required to saturate the gain to a uniform profile (along the action medium) through spatial hole-burning. Note however that, again as expected, the two first modes to appear carried most of the laser output energy.

3. Short Fiber Lasers

The series of measurements made on $\sim 100 \text{ }\mu\text{m}$ diameter, $\sim 8 \text{ mm}$ long Nd:YAG fiber lasers (aspect ratio ≈ 80) indicated that it would be interesting to attempt reducing cavity loss by moving toward lower aspect ratio fiber lasers. This was achieved with fiber array #2 (see TABLE 6), with a length of 4.0 mm and fiber diameters ranging from $213 \text{ }\mu\text{m}$ to $255 \text{ }\mu\text{m}$, or an aspect ratio of ~ 17 . This array was the object of extensive measurements, reported in this section.

Using the same experimental arrangement as before, all the fibers of array #2 were lased at one point or another. Since they all showed approximately the same operating characteristics, most of our measurements were concentrated on one of them, namely fiber #2-5 (unless otherwise specified). Initial measurements indicated a threshold of 5 mW , a linear output curve with a slope efficiency of 2.2% ($T = 1\%$) and a calculated round-trip loss of 22% . For these shorter lasers,

approximately 16% of the pump power incident on the lens ($f = 98 \text{ mm}$) was actually absorbed by the fiber.

A first important remark must be made concerning the fact that these fiber lasers were operated without AR-coatings, while the observed round-trip loss is still much less than would be expected from the Fresnel loss ($4 \times 8.5\% = 34\%$) alone. In the present geometry the laser cavity actually consists of three optical cavities, namely the fiber itself and the two cavities formed by each fiber end and mirror. Provided scattering at the fiber ends is small, the two end-cavities can have their lengths adjusted to bring their respective longitudinal mode to coincide with one of the longitudinal modes of the fiber cavity, at least in principle. We believe this is what was indeed observed, as hinted by the relatively low cavity loss. The laser cavity alignment was also far more critical on the mirror longitudinal position than usual, as expected. When the mirrors were brought to locally contact the fiber holder the cavity could be mechanically stabilized well enough to perform further measurements.

During the experimental study of array #2 we observed that the alignment of the incident pump beam with respect to the fiber axis was critical to the performance of the laser, in terms of both its threshold and efficiency. A theoretical analysis of the effect of a relative offset or tilt between pump and signal modes on the laser characteristics was conducted (see APPENDIX D). In essence, either a relative constant offset (the two mode axes remain parallel but offset by Δ) or an angular offset (mode axis at an angle, α) spoils the modal overlap and reduces the laser slope efficiency while increasing the threshold. The analysis shows that tolerance on a constant offset is easy to meet, as the modes must be coaxial to better than $\Delta = W_p/5$ for 90% optimum

performance. On the other hand, the effect of an offset is rather significant, and tilt angles must be kept below a critical value of about $1/2$ degree for acceptable performance. Meeting this last condition was, in general, difficult to achieve experimentally as the fiber positioner (see Figure 22) was not equipped with fine tilt stages.

Careful fiber tilt alignment was possible, however, using available adjustments. We found that, as predicted by the theory, a great improvement in laser characteristics was brought about by minimizing the spurious tilt angle between the pump and signal beams. This angle was measured by observing in two orthogonal directions the signal and pump output beams coming out of the fiber laser with a fixed diode array. This angle could then be minimized, and possibly cancelled, by rotating the fiber axis in the appropriate direction and by an appropriate amount. We thus observed that the threshold was decreasing and the slope efficiency was increasing when the beam angle was reduced. The fiber laser performance was near optimum for tilt angles smaller than $\sim .4^\circ$, which shows that our theoretical analysis is fairly accurate, if slightly pessimistic. This improvement led to the demonstration of the lowest-loss fiber laser developed under this program. Figure 29 shows the output power curve of the laser as measured after bringing the beam tilt angle down to $\sim .14^\circ$ (2.4 mrad). A maximum output power of 9 mW was obtained, with a threshold of ~ 11.5 mW and a slope efficiency of 31%. As before, the output beam was polarized linearly (1:100, parallel to the pump polarization), and even at the maximum tested output power the fiber laser was running single transverse mode. These combined characteristics make this device the most efficient fiber laser yet demonstrated in our laboratory. Its output power of 9 mW at 40 mW of pump power is well in excess of our original 5 mW goal, and was only limited by the maximum output

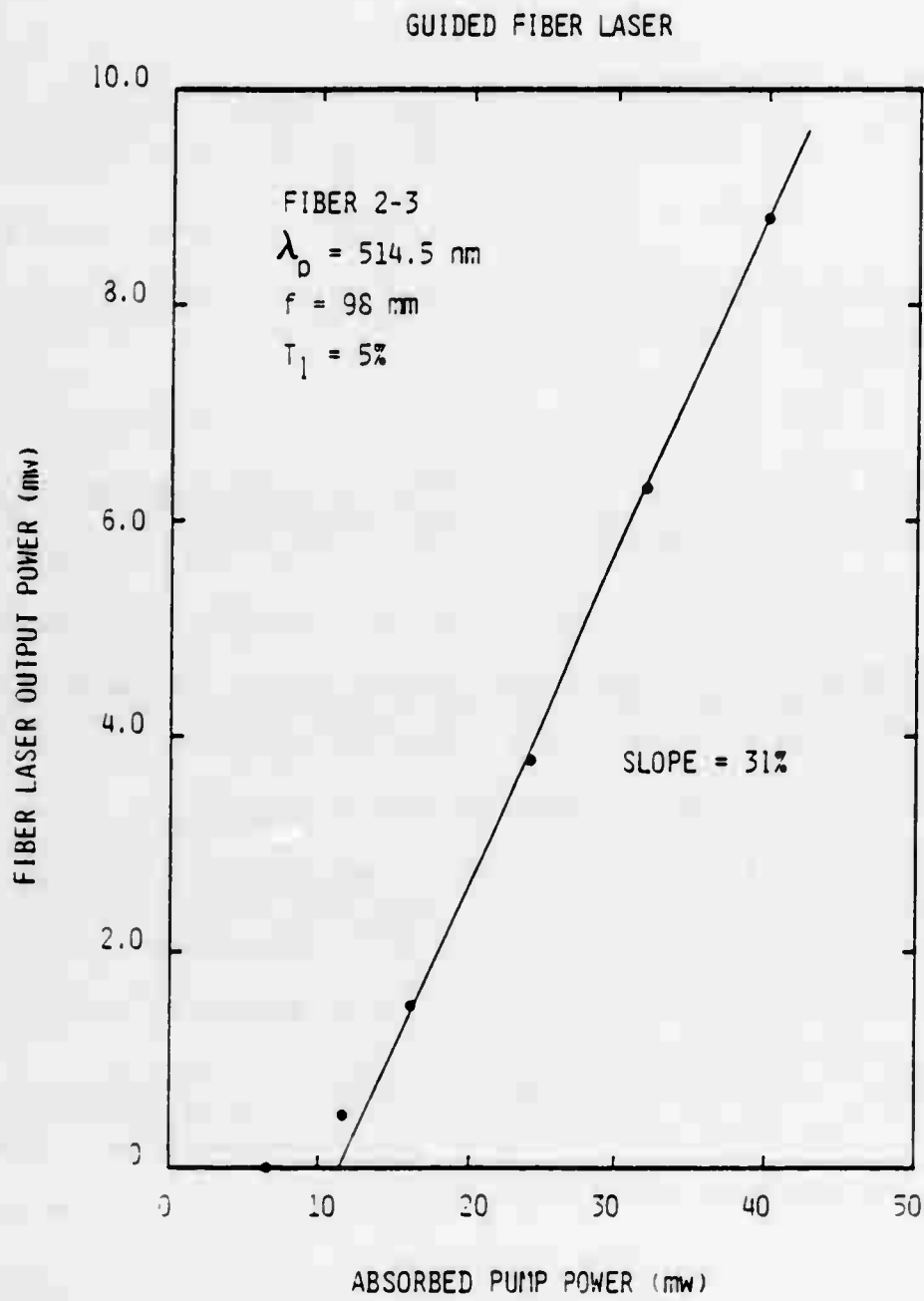


Figure 29--Output Power Curve of Fiber Laser #2-3.

power tested, not by any fundamental limit. Similarly the observed slope efficiency was only limited by the choice of output coupler transmission available.

These and other measurements with $T = 1\%$ were compatible with a residual fiber loss $\delta_1 = 2.8\%$ only, or, assuming fiber propagation loss is dominant, an overall fiber loss factor of $\alpha_s \approx .035 \text{ cm}^{-1}$ (.15 dB/cm). The pump effective area A_p^* estimated from laser measurements is $4.1 \times 10^{-5} \text{ cm}^{-1}$, which reflects a relatively tight mode confinement.

The signal output mode was found to be a very clean and symmetrical single fundamental mode. Measurement of the far-field profile with a high-resolution diode array yielded the value of $30.8 \text{ } \mu\text{m}$ for the mode radius inside the fiber compatible with the measured value of A_p^* . Compared to the 234 micron diameter of fiber #2-5, this value suggested again the presence of some guiding mechanism.

An investigation of the possible guiding mechanisms present in a fiber laser was conducted to explain this behavior (APPENDIX E). It showed that index gradients due to the crystal structure itself or its surrounding (cladding) are by far the strongest guiding mechanism. In fibers with inhomogeneous loss, loss-guiding may also be a strong possibility. However, other mechanisms such as nonlinearity, χ' -guiding, thermal lensing or gain-guiding have small or negligible effects on fiber laser modes (see TABLE E-1). As a corollary, these intensity-dependent mechanisms have also negligible limiting effects on the fiber laser performance, whereas they do become troublesome in high power solid state lasers.

In order to verify the presence of gain-guiding, the same fiber was brought to oscillation with different pump mode sizes - if gain-guiding was the main guiding effect the signal mode profile was expected to show some dependence on the gain radial profile. However, within experimental errors, measurements

TABLE 9
MODE MEASUREMENTS IN FIBER LASER #2-5

f (mm)	W_p (Measured, μm)	W_s (Measured, μm)	P_{th} (mW)
55	13	31.7	5.5
98	17.2	30.8	5.5
177	28.2	31.0	8.4

indicate no such dependence (TABLE 9). Although the pump waist size was changed from 13 to 28 μm the signal waist radius was constant and equal to about 31 μm . Two other observations further support our belief that gain-guiding was not the main guiding mechanism in these fibers: (1) in some cases the pump and signal beams emerging from the fiber laser were not coaxial; (2) when rotating the fiber (to cancel the tilt angle) the signal beam followed the fiber axis while the pump beam was virtually unaffected.

A second effect that might have been responsible for the confinement of the signal mode is the optical cavity. We therefore checked the curvature of laser mirrors. Mirrors were tested against an optical flat under a coherent, quasi-monochromatic source. Their flatness was excellent, probably better than $\lambda/2$ across the entire mirrors. When bonded in the same fashion as they are when used in external cavities, they showed a very slight curvature estimated to have a radius of curvature of several meters. The (bonded) mirrors used in our laser

cavity with fiber array #2 were further tested to provide a better measurement of their curvature. By observing the divergence of a He-Ne laser beam reflected from and transmitted through these mirrors we were able to find that the mirrors do have a slight positive curvature, that both sides have approximately the same curvature, with a radius in excess of 3 meters for both mirrors. However, to explain a 30 μm signal mode, a curvature of 1.2 cm would be necessary. Therefore no significant mode confinement was provided by the mirrors.

Another possible guiding mechanism was real Δn -guiding to an index profile within the fiber. The presence of such a profile was suspected on the ground that during fiber growth, the large temperature gradient that develops between the surface and the center of the fiber favors migration of Nd-ions (and other impurities) towards the fiber center. This effect is indeed routinely observed during the growth of Nd:YAG boules. Simple thermodynamic considerations would then suggest that larger diameter fibers develop larger Nd: concentration gradients. Since Nd impurities increase the index of YAG (Reference 12), a positive, guiding index profile might be present in larger fibers.

The so-called interferometric slab method was used to attempt detecting such index profiles in CMR-grown Nd:YAG fibers. Thin slabs of fibers were placed in one of the arms of a Mach-Zehnder interferometer and the magnified image of the slab surface was formed on a screen. When the interference field is originally uniform (constructive interference), any index variations across the fiber appear as sets of fringes. For example, a cylindrical index profile yields a set of concentric circular fringes. When the interference field is originally fringed, the same index variations appear as distortions of these fringes across the image of the fiber. In both cases a two-dimensional mapping of the fiber index profile is generated. By counting fringes in the first case, or fringe shift in the

second, one has access to the index information. If t is the slab thickness and λ the wavelength of measurement, the index difference between two consecutive fringes is given by $2\pi t \Delta n / \lambda = \pi$.

This method was applied to arrays #5 and #10 (see TABLE 6) using a He-Ne laser as a source. The slabs were cut from longer holders in which the fibers were mounted as before, then polished to a thickness of ~ 500 microns. The fibers tested had diameters ranging from 70 to 250 microns.

We show in Figure 30(a) (fiber diameter $\approx 95 \mu\text{m}$) and 30(b)(concluded) ($120 \mu\text{m}$) two typical fiber interferometric images obtained in a fringed field. As was observed for all of the fibers, the interferometric field distortion introduced by the fibers is minimal to the point of being barely noticeable, say a phase shift smaller than $1/4$ fringe. In uniform field none of the fibers introduced any noticeable fringe. Only fiber #5-11 [Figure 30(b)] seemed to introduce some fringe distortion near its center. Estimating this distortion to be one quarter of a fringe, the maximum observed index gradient is $\sim 2 \times 10^{-4}$. Compared to the maximum value of 1.1×10^{-3} expected in 1% doped Nd:YAG, this value indicates that the gradient of Nd-concentration across any of the tested fibers is less than 20%. Fiber #5-11 was also the largest of fibers in array #5 ($\phi \sim 120 \mu\text{m}$).

Repeating these measurements with $\sim 250 \mu\text{m}$ diameter fibers (array #10), we observed that the fringe pattern of each fiber was slightly distorted, and in general more so than for the smaller diameter fibers of array #5. However, it raised the question of the exact origin of this fringe distortion, which can be either a slight curvature of the fiber end surfaces, or a gradient of index within the fibers. The fiber end flatness is on the order of, or better than,

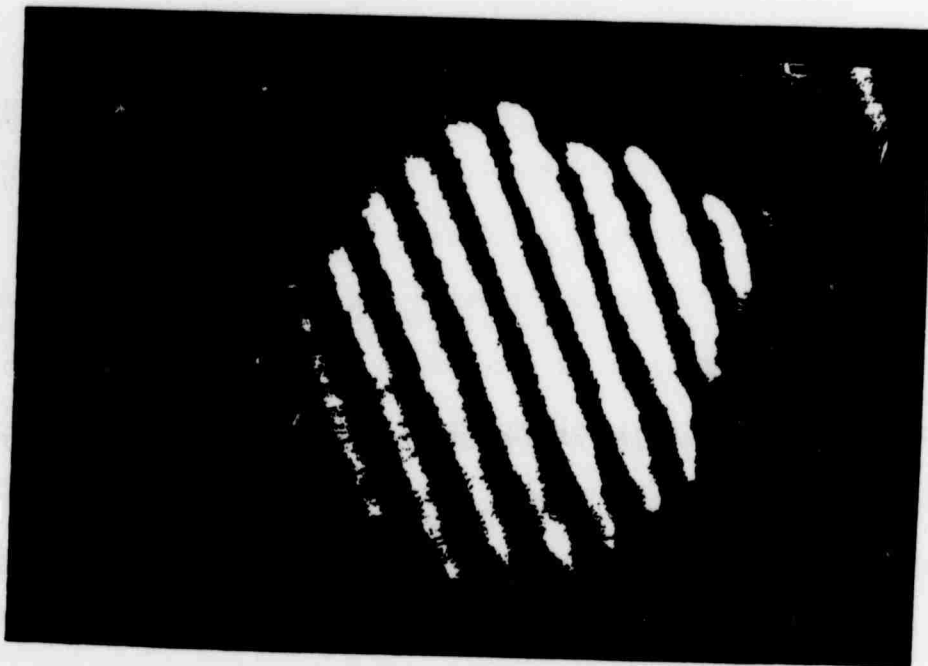


Figure 30(a)--Interferogram of Nd:YAG Fiber #5-9.

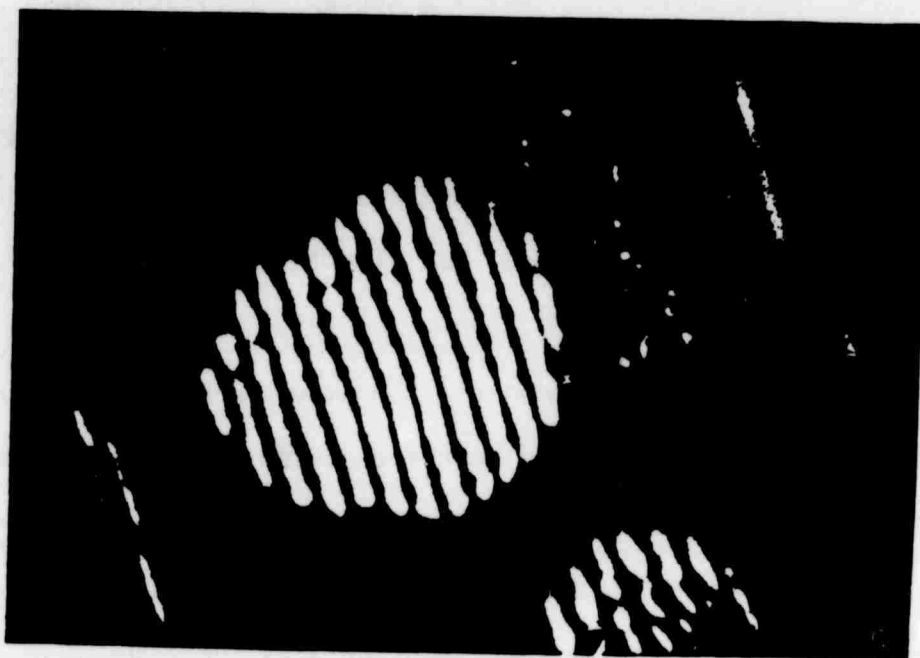


Figure 30(b)--Interferogram of Nd:YAG Fiber #5-11.

$\lambda/4$, i.e., on the order of the fringe shift created by the type of index gradient to be measured. For example, the top fiber of array #10 had poorly polished ends as it was somewhat loosely bonded, and showed strong fringe distortions on the order of one fringe. A hasty conclusion would have erroneously attributed it to a strong index gradient.

Since flatness is difficult to map accurately, discrimination between these two effects is also difficult. A possible method to eliminate the unwanted effect of residual fiber end curvature would be to place the fiber array between two high-quality optical flats (say, better than $\lambda/10$ flatness) and insert an index matching liquid between the flats and the array. Ideally both the liquid and the optical flats should have the same refractive index as the fiber (here ~ 1.82 for Nd:YAG). When implemented with glass microscope cover slips (which are locally very flat) and a 1.45 index matching liquid, this approach showed a slight reduction in fringe distortion. However, because the matching was imperfect, the conclusion is not very firm.

Although it is clear that further measurements are required to finalize this point, we believe the presence of a slight index gradient in larger Nd:YAG fibers is still a good possibility. Two guiding mechanisms in fibers of array #2 therefore remain possible, namely Δn -guiding and loss-guiding. This last mechanism would originate from the inhomogeneous transmission of $\sim 250 \mu\text{m}$ fibers. When probed with a tightly focused ($w \sim 10 \mu\text{m}$) optical laser beam at $\lambda = 633 \text{ nm}$, they all show that some regions of the fiber transmit the signal with less distortion than others. In a particular fiber this region of better optical quality would thus offer a low-loss path to the laser signal (at $1.06 \mu\text{m}$), which would be confined to it by the higher loss of the surrounding region. This hypothesis is to be correlated with our observation that in $250 \mu\text{m}$

fibers lasers, the signal state of polarization (SOP) was a function of mirror alignment. When the fiber laser was aligned to its lowest threshold, the signal and pump SOP were identical. When the cavity alignment was intentionally spoiled, the signal SOP was altered (e.g., to a 1:10 linear polarization, down from 1:100 in the best alignment case). This indicates that the fiber laser may actually operate in two different states, the first one being the guided state, and the second one the unguided state. In the second state the signal would be more strongly aware of the outside part of the fiber and suffer more loss (higher threshold) and polarization alteration through scattering. These two operating states were also correlated to the signal transverse mode profile, which was circular when the mode was guided, and more elliptical (up to $\sim 1:2$ ellipticity) when the mode was "unguided". These observations make us believe that in these particular fibers, loss-guiding is probably the dominant guiding mechanism.

4. Guided Fiber Lasers

Another area of interest was the demonstration of guided laser action in Nd:YAG fibers with a large aspect ratio. This was performed with fibers of array #4 which, with an average fiber diameter ranging from $78\text{ }\mu\text{m}$ to $81\text{ }\mu\text{m}$ and a length of 11.8 mm, have an aspect ratio of ~ 150 .

With a cavity mode of a high reflector and a 1% output coupler, only two of the five fibers (#4-1 and #4-5) were successfully brought to oscillation. Again we noticed a definite correlation between the measured laser threshold (i.e. the fiber loss) and the quality of the pump mode coming out of the fiber. Fiber laser #4-1 had a threshold of about 54 mW (absorbed power). The pump mode quality was not nearly as good as that of fiber #4-5, which exhibited a threshold of only 3.5 mW. In both cases the output was a single transverse mode (fundamental). The signal polarization was again identical to the pump

polarization when the cavity was well aligned.

Characterization of fiber laser #4-5 led to a number of very interesting conclusions. First we noticed that despite its low threshold, it had a very small slope efficiency (200 μ W of output at $P_{abs} \approx 50$ mW, or $s \approx .5\%$). It indicates a high single-pass loss, on the order of 60% ($\pm 15\%$). Since this loss was offset by only pumping the fiber with about 3.5 mW, it also means that this fiber provides a very large round-trip gain per unit pump power, approximately 14%/mW, or .6 dB/mW. This was confirmed by measurement of the pump and signal mode radii, $W_p = 16 \mu$ m and $W_s = 14.6 \mu$ m, respectively. The calculated pump mode effective area is then $A_p^* = 7.4 \times 10^{-6} \text{ cm}^2$, corresponding to an expected gain of precisely 13%/mW, as measured. These results are consistent with a value of $\sigma = 2.3 \times 10^{-19} \text{ cm}^2$ as before, although the fibers of array #4 originated from Bell Telephone Laboratories. Although the fiber is relatively lossy, it also provides a good mode confinement and a high gain factor.

Prior to mounting, the fibers were cut into 12 to 13 mm length pieces and their diameter measured on a traveling-stage optical microscope (resolution $\approx .5$ -1 μ m). Each fiber was scanned along its length and lows and highs of its diameter (which occurred every 300-600 μ m) were recorded (25 to 35 data points per fiber). We show in TABLE 10 the characteristic diameter variations of each fiber: average diameter $\bar{\phi}$, average diameter variation $\Delta\phi/\bar{\phi}$, and maximum diameter variation $(\phi_{max} - \phi_{min})/\bar{\phi}$.

The measured value of $W_s = 14.6 \mu$ m corresponds to a Rayleigh range in Nd:YAG of $z_R = 1.15$ mm, much shorter than the fiber half length (~ 6 mm). The signal therefore appears to be guided by the fiber. Note also that the pump mode was barely guided ($z_R \approx 2.84$ mm). With an average core radius for fiber #4-5 of $a = 39.9 \mu$ m, the expected signal radius is $.645 \times a \approx 26 \mu$ m, larger than

TABLE 10
DIAMETER DATA OF FIBER ARRAY #4

Fiber #	$\bar{\phi}$ (μm)	$\Delta\phi/\phi$	$(\phi_{\text{max}} - \phi_{\text{min}})/\bar{\phi}$
4-1	80.2	6.7%	21.9%
4-2	78.6	6.5%	19.1%
4-3	80.6	9.6%	40.1%
4-4	77.9	5.4%	16.0%
4-5	79.8	7.2%	28.3%

the measured value. Again we find that aperturing by the thinnest sections of the fiber is probably responsible for the unusually small signal mode size. This provides, however, a clear demonstration of laser action in a guided fiber laser in which the guiding mechanism is provided by the fiber aspect ratio. It also confirms our general impression that the main source of loss in fiber lasers is propagation loss (crystal bulk and/or surface quality).

SECTION V

LASER-DIODE-PUMPED FIBER LASERS

As mentioned earlier, pumping Nd:YAG fiber lasers with cw laser diodes operating in the 810 nm region offers a number of interesting features and advantages. First, Nd:YAG presents a strong absorption band in the 800-820 nm region (Figure 31) and laser excitation via this pump band can be performed with shorter fibers, and therefore lower loss cavities. Second, the pump photon energy is only 25% larger than the signal photon energy, and high laser energy conversion efficiencies are expected. Finally, the size of the pump source is matched to that of the fiber laser, and device miniaturization is possible.

Until recently, the major restriction encountered in pumping Nd:YAG lasers with laser diodes was their low power (10-15 mW) and out-of-band wavelength (< 825 nm). Although in principle GaAlAs diodes can be made to emit anywhere between 800 nm and 860 nm by controlling their Al-doping, most manufacturers still do not supply wavelength-tailored diodes on a routine basis. However, for the purpose of the present work, we were able to purchase laser diodes from Hitachi with emission wavelengths specified to 810-820 nm and output powers up to 15 mW. Also, the Palo Alto Xerox Research Center generously loaned us several diodes specifically fabricated for Nd:YAG laser pumping applications.

The availability of these diodes made possible the demonstration of low-threshold LD-pumped Nd:YAG fiber lasers. We report below the results of this work. Data on laser diode characterization, LD-to-fiber optical coupling, and LD-pumped Nd:YAG bulk and fiber laser operation are presented.

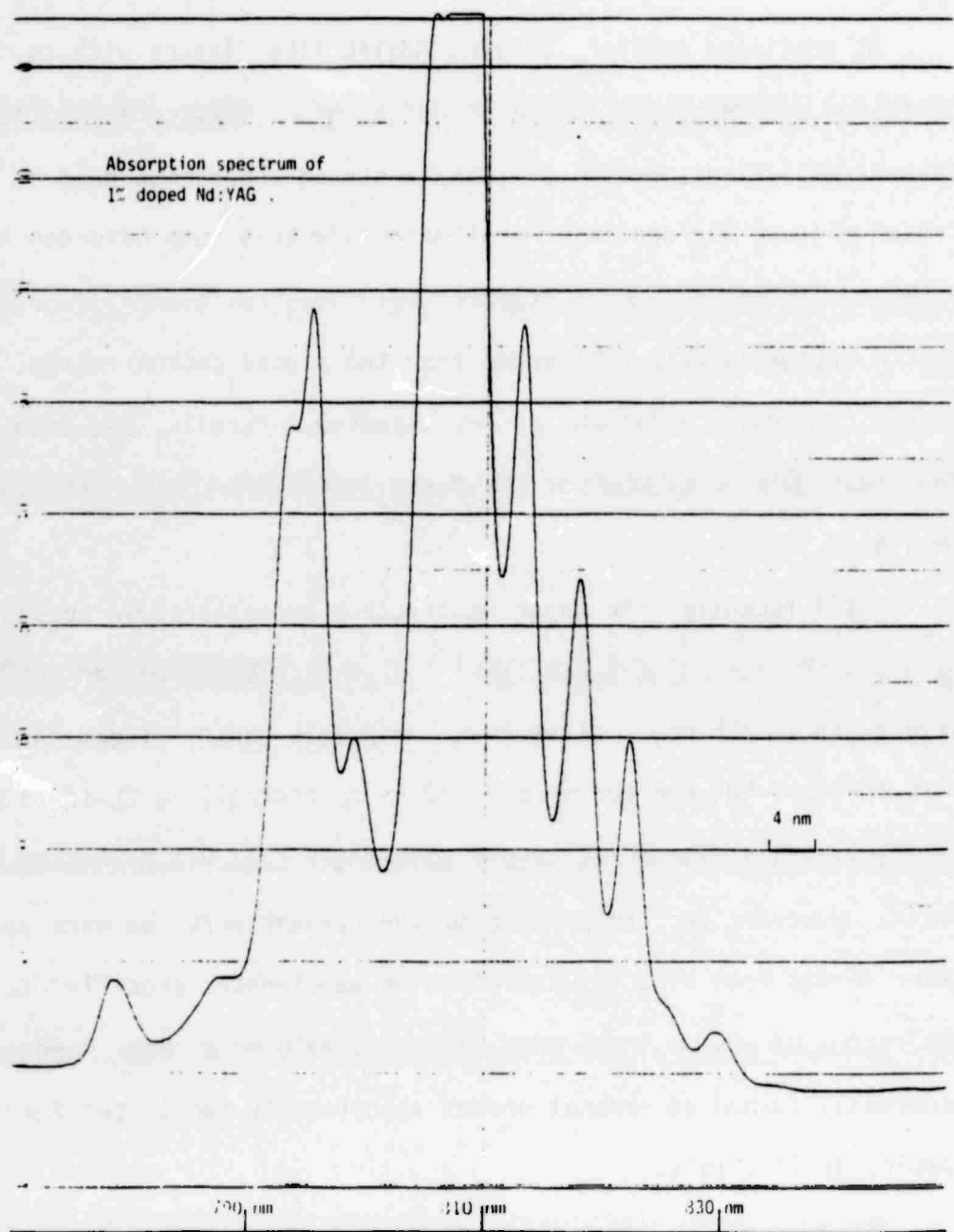


Figure 31--Absorption Spectrum of ~1% Doped Nd:YAG in the 810 nm Region, measured on a Perkin-Elmer Model 330 Spectrophotometer (Resolution ~.7 Å). Sample Thickness is 6 mm. Full Vertical Scale represents ~100% Absorption.

A. LD CHARACTERIZATION

In the course of this work, a total of 6 laser diodes emitting in the 820 nm region were available. Two of these diodes were manufactured by Hitachi (HLP-1400). The other four laser diodes, on loan from another research group in the Ginzton Laboratory, were provided by the Palo Alto Xerox Research Center. In this section we describe the characteristics of the two diodes that were actually used in fiber laser pumping experiments, namely one of the single-stripe Hitachi laser diodes (Hitachi #2) and one of the multiple-stripe Xerox diodes (#X-2).

1. Hitachi Laser Diodes

We show in Figure 32 the output power versus current characteristics of Hitachi #1 provided by the manufacturer. A typical threshold of oscillation for these diodes is $I_{th} \approx 60-70$ mA, with a maximum output power of approximately 15 mW. This particular diode was selected for its lasing wavelength of about 815 nm at 10 mW of output, well matched to the absorption of Nd:YAG (see Figure 31).

The Hitachi diodes were operated with a custom made power supply designed and fabricated by Ginzton Laboratory technicians, which includes a power supply and a mother board to eliminate current spikes that may be harmful to the diode junction. Our own measurements with Hitachi #1 indicated a similar threshold to that specified by the manufacturer, but a maximum output power of only 11-12 mW (versus 15 mW specified) at a maximum current of 137 mA. The laser wavelength, measured with a ~ 4 Å resolution grating monochromator, was found to vary from 814 nm at threshold to 817 nm at full current. This corresponds to a $\delta\lambda/\delta i$ of .5 Å/mA typical for this type of device.

Hitachi Laser Diode Test Data

Type HLP-1400 Serial No 2E0587

Temperature 22 °C

Hitachi, Ltd.
Electronic Devices Group
Hitachi, Ltd.
Tokyo, Japan

Date MAY 11, 1982

Tested by S. Ishii

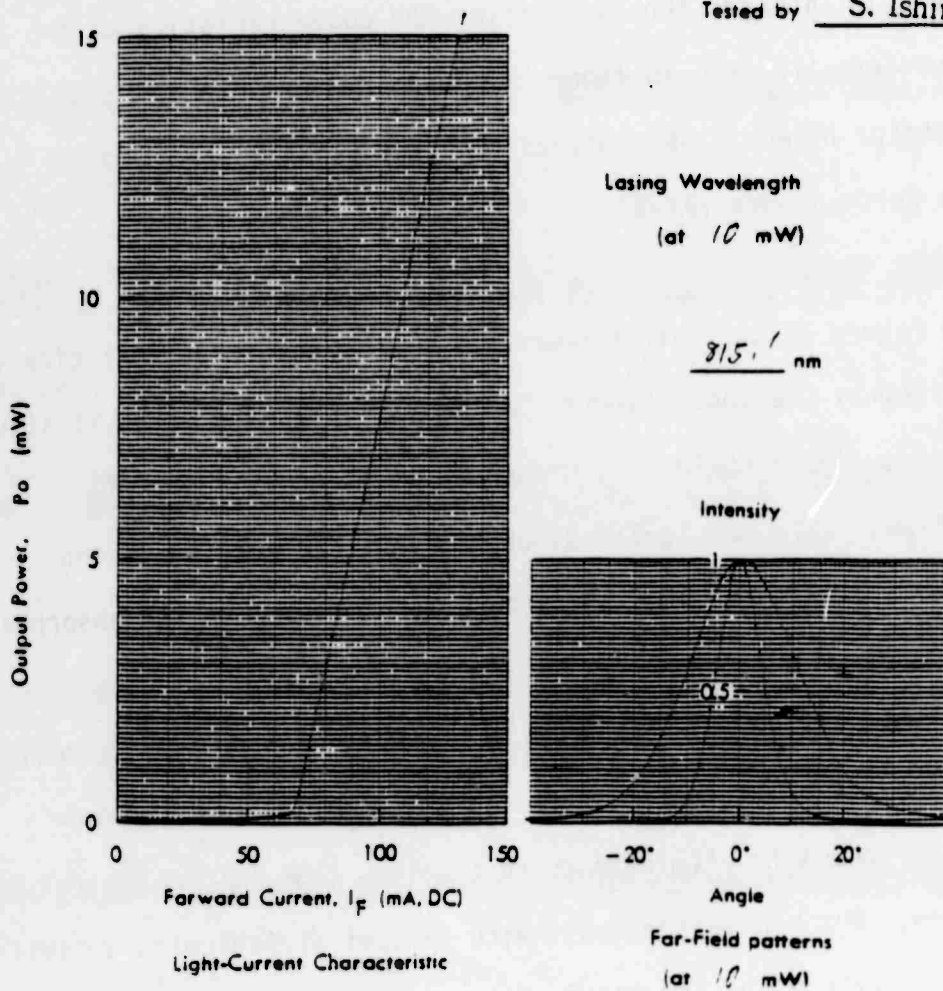


Figure 32--Characteristics of Laser Diode HLP-1400 provided by Manufacturer.

The second Hitachi diode (Hitachi #2), on loan from Hitachi Corporation as a back-up unit, was found to emit about 25% more power (14-15 mW) at a slightly longer wavelength (~ 817 -821 nm). Because of its higher maximum output power it was preferred to Hitachi #1 for laser pumping experiments.

2. Xerox Laser Diodes

As mentioned earlier, two types of cw laser diodes were loaned to us by the Palo Alto Xerox Research Center. The type of interest here is a new experimental laser diode recently developed at Xerox and not yet commercially available. They are multiple-stripe diodes made of a linear array of approximately 10 gain-guided lasers on ~ 10 μm centers (Reference 20). Such devices have been shown to emit as much as 2.5 watts per facet (Reference 21). By operating these lasers simultaneously in a phase-locked manner, near single-lobe far-field patterns have been observed which should yield high coupling efficiency to small core optical fibers (Reference 22).

The device reported here was of the same type but was not phase-locked. Its output power curve is shown in Figure 33. A maximum cw output of ~ 165 mW was obtained with a forward current of 730 mA, as measured by the manufacturer. The threshold of oscillation was reached with a forward current of about 250 mA. At this relatively low output power (this particular diode could be operated up to 400 mW per facet) it is believed that the diode lifetime could be extended from 100 hours (at 400 mW) to 1000 hours or more, suitable for extensive characterization and measurements.

Operation of this diode in our laboratories was delayed toward the end of this contract by unforeseen difficulties in the design and fabrication of its power supply. The requirements on this supply are actually quite demanding as it must deliver nearly 1 ampere of cw current with little transient spiking.

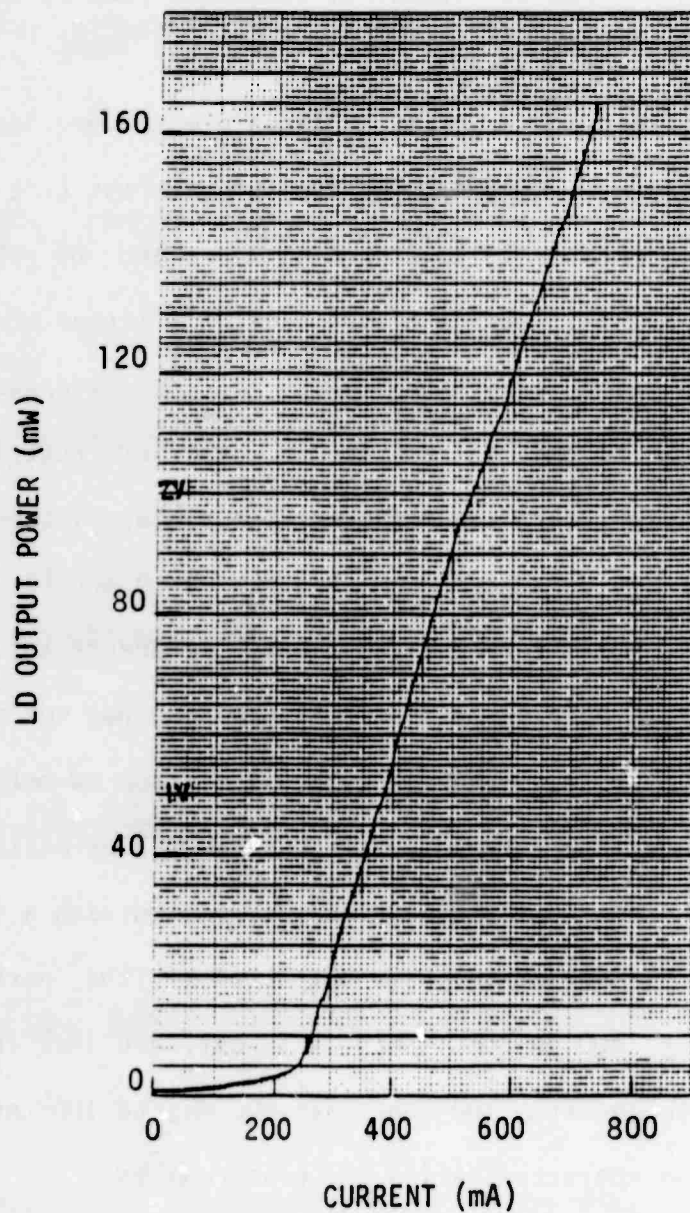


Figure 33--Power versus Current Curve for High-Power Laser Diode Array #X-2 (from Xerox Research Center, Palo Alto, California).

Initial tests showed that the laser diode had to be mounted on a separate holder to avoid damage from the heat generated by the regulating circuitry (which is placed in the same holder as the laser diode for the lower power Hitachi diodes). These difficulties were, however, successfully solved and the diode routinely operated before the end of this contract.

Observation of the output mode pattern of this diode (labeled #X-2 in the following) showed a series of vertical lines, each of which corresponds to the output of one of the lasers in the array. Diffraction in the vertical direction (i.e., perpendicular to the plane of the array) was very strong as a result of the small size of the junction in this direction. The threshold of oscillation was found to be ~ 280 mA, while the maximum output power after a 5 minute warm-up was about 120-140 mW at ~ 780 mA.

B. LD-TO-OPTICAL FIBER COUPLING

The coupling of a laser diode beam into an optical fiber was investigated for a variety of configurations to optimize the amount of absolute power launched into crystal fiber lasers. In their present configuration the fiber lasers operated with external mirrors do not lend themselves well to direct butt-coupling, and most of our efforts were concentrated toward a suitable imaging of the diode output facet on the input end of a fiber. The laser diode output was thus first recollimated into a nearly parallel beam before being focused to a small spot size and coupled into the fiber. In these and in following measurements, the laser diode was mounted on an aluminum block for mechanical stability. Recollimating optics were mounted on the same block, together with all required micro-positioners. The entire holder, approximately $3 \times 5 \times 5$ inches, could then be positioned anywhere on the

optical bench like any ordinary laser. Results obtained with both types of diodes are described below.

1. LD #H-2

The use of Selfoc lenses as collimation and focusing optics was particularly attractive because of their small size and potential for miniature systems. Using a miniature x-y-z stage mounted on the holder described above to position a single high-numerical aperture Selfoc lens (Reference 22) in front of the laser diode junction, the LD output beam was recollimated without significant loss of power. However, when using either a low or high numerical aperture Selfoc lens to approximately recollimate the laser diode output beam, two difficulties arise. First the spot size of the approximately recollimated beam is very small, estimated at 100-200 μm . To focus this beam to a $\sim 40 \mu\text{m}$ spot for fiber laser excitation, a relatively short focal length lens is required to make up for the small recollimated beam, on the order of a few millimeters. This focal length does not leave enough working distance between the lens and the input fiber end (the mirror gimbal mount is 30 mm thick). Slightly defocusing the Selfoc lens does expand the recollimated beam (and allows one to use slightly longer focal length lenses). However, because of the small diameter of the Selfoc lens ($\leq 1 \text{ mm}$) it also reduces the fraction of diode power captured by the Selfoc. The second problem is that the recollimated beam shows a series of concentric rings surrounding the brighter central spot due to the strong geometric aberration of our Selfoc lenses. The poor quality of the beam is expected to be detrimental to fiber launching efficiency.

The Selfoc lenses used in these measurements were acquired several years ago. Recent reports on progress in Selfoc lens technology indicate that new

generations of lenses have much better overall quality and properties (Reference 23). In particular, laser beams have been focused to $\sim 1 \mu\text{m}$ spot sizes using lenses with reduced geometric aberration. Consequently, we believe new Selfoc lenses should be more adapted to the problem at hand. The working distance problem will be eventually taken care of in future fiber laser designs by either implementing smaller mirror gimbals, or bonding the mirrors directly onto the ends of the fiber laser.

As an alternative solution we replaced Selfoc lenses by microscope objectives, which yielded a greatly reduced ring structure in the recollimated beam. Optimization of the recollimated power was achieved by using objectives with increasing power and numerical aperture (N.A.). A large area silicon detector, calibrated against a Spectra Physics 404 power meter, was used for power measurements. For each measurement the microscope objective was carefully aligned to provide a beam collimated at infinity. Results are summarized in TABLE 11 and Figure 34. As expected, the amount of total power carried by the collimated beam increases with the objective numerical aperture, converging to an asymptotic value corresponding to maximum diode-to-objective coupling efficiency. This value is essentially reached for a N.A. of .5, corresponding to the maximum divergence angle of the diode output beam ($\sim 30^\circ$). The maximum measured coupling efficiency is about 86%. The residual 14% is probably due to Fresnel loss in the objective. In the case of the 40x and 60x objectives, the recollimated beam was slightly diverging because the front face of the objectives could not be brought close enough to the diode. The divergence angle was, however, small enough to be of no consequence for further focusing. Figure 34 shows the actual collimated optical power at full diode current. Over 12 mW of collimated power was thus

TABLE 11
 RECOLLIMATION MEASUREMENT DATA FOR LASER DIODE #H-2
 (HITACHI HLP-1400)

Objective Power	N.A.	P_{out}/P_{inc}	Beam Divergence
5x	.10	27.9%	Collimated
10x	.30	67.7%	Collimated
20x	.40	70.3%	Collimated
20x	.50	75%	Collimated
40x	.65	79.7%	Slightly divergent
44x	.66	85%	Collimated
60x	.85	86%	Slightly divergent

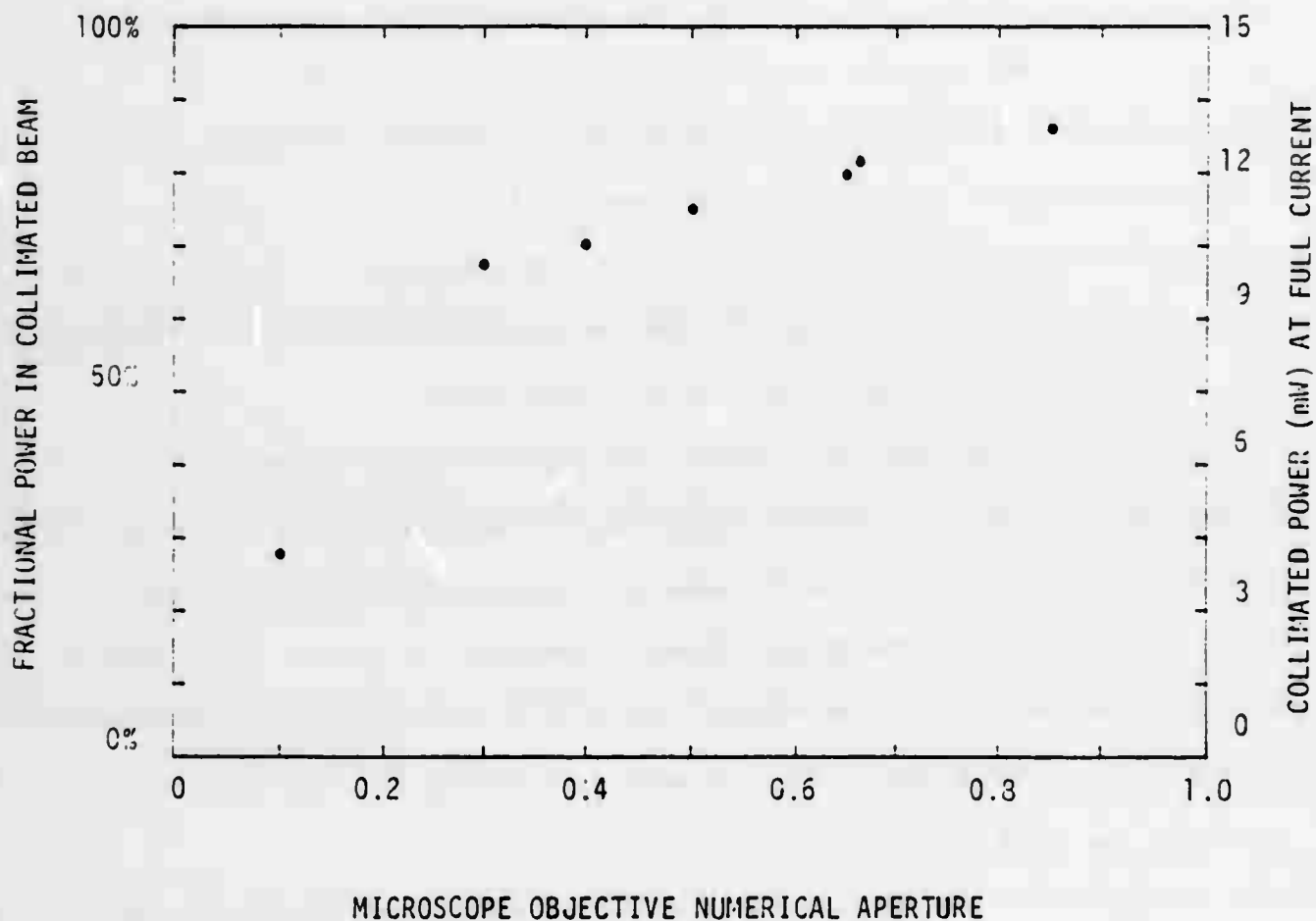


Figure 34--Absolute and Relative Power carried by Collimated Laser Diode Beam as a Function of the Objective Numerical Aperture (Hitachi HLP 1400 Diode).

available with microscope objectives.

A number of additional optics were tested to attempt optimizing the recollimation while implementing different optics. A highly multimoded plastic core fiber was used to capture the laser diode beam. The fiber used, two feet in length and surrounded by a flexible jacket, had a 1 mm diameter core and a N.A. of .5. The measured fiber output power at full diode current was about 10.5 mW, i.e. similar to that obtained with a 20x microscope objective, as expected. The output power was essentially uniformly distributed in a $\sim 20^\circ$ angle circular cone. Although this configuration does not recollimate the diode beam, it may have some interesting applications with large area laser diodes. It may also provide a simple solution to the problem of bringing the diode beam to the single crystal fiber.

Attempts at implementing a single high refractive index, short focal length lens ($n \approx 1.8$, $f \approx 2\text{-}5$ mm) to recollimate laser diode beams were not successful so far. Although such lenses captured a large fraction of the diode power, the recollimated beam showed a series of concentric rings similar to those observed with Selfoc lenses. Again this was due to lens geometrical aberrations, although the lenses used were specified by the manufacturers as having a low level of aberration.

The conclusion of these tests is that the highly diverging output beam of laser diodes requires optics specially corrected for aberration for proper recollimation. Observation shows that even the cheaper brands of microscope objectives introduce relatively little ring structure to the laser beam as compared to a single good quality lens, whereas quality objectives yield very clean recollimated beams. Aberration-corrected multiplets seem to be a good solution to the problem. It should be noted here that such special optics do

not necessarily occupy much more volume than miniature optics such as Selfoc lenses. For example, the effective size of the optics involved in a 60x objective is typically on the order of 2 mm in diameter by 8 mm in length. Such a small size is definitely compatible with miniature fiber laser dimensions.

Measurements on coupling to a Nd:YAG fiber were done using a 20x objective to recollimate the pump beam. Coupling to fibers of array #7 ($\phi \approx 85 \mu\text{m}$, see TABLE 6) was optimized when focusing the recollimated beam with a ~ 20 mm focal length lens, yielding 85% coupling efficiency. Longer focal length lenses, which are required because of the minimum working distance (~ 30 mm) imposed by the mirror mounts, also gave high coupling efficiencies by making the recollimated beam slightly divergent. By modifying the beam divergence, the focused spot size could be greatly varied. With an 80 mm focusing lens and an adequate divergence, collimation was adjusted to produce a $\sim 14 \mu\text{m} \times 56 \mu\text{m}$ focused spot, as measured with an imaging diode array. Under these conditions the launching efficiency into the crystal fibers was near 100% (except for Fresnel loss). This method was widely used in fiber laser tests to optimize the focused spot size of the pump within the fiber.

The absorption coefficient of either Nd:YAG bulk crystals or fibers at the laser diode wavelength (at full current) was found to be about $1\text{-}1.4 \text{ cm}^{-1}$. We observed that the sample transmission varied with the amount of power reflected by the optics and fed back into the laser diode cavity. The feedback probably scans the few longitudinal modes across the laser diode gain curve (typically 15 Å wide). Since the absorption peaks of Nd:YAG in the 800 nm region are quite sharp (see Figure 31), a small shift in laser

frequency results in a significant variation in absorption. By modifying the feedback power, the absorption coefficient was observed to become as large as $\sim 6 \text{ cm}^{-1}$.

Several methods were proposed to stabilize the LD wavelength. One is to use the output beam from the second diode facet to monitor the wavelength by temperature tuning, or feedback tuning. A second one is to temperature bias the diode so that its central frequency lies at the top of a broad and strong absorption peak (say 98%, with $\Delta\lambda$ of say 50 Å). Then a variation in laser frequency (at most $\sim 15 \text{ Å}$) will cause only a small variation of the absorption (say, down to 90%), and a 10% stable fiber laser output. A laser diode emitting at room temperature at $\lambda = 808 \text{ nm}$ would satisfy these conditions without requiring temperature tuning. This could be easily achieved by mounting the diode on a thermoelectric cooler. We could also reduce or eliminate feedback by using lenses with a round, rather than flat, front surface, or by using optics AR-coated at 810 nm. Although such methods were not implemented under this program, the wavelength stability of this type of LD was fairly stable under normal operating conditions. As will be seen in SECTION V-C, optical feedback was not detrimental to fiber laser operation.

2. LD #X-2

Recollimation of the laser beam emitted by the high-power laser diode from Xerox (#X-2) was performed with microscope objectives. The power recollimated with a 44x, .66 N.A. objective was about 140 mW at full current, or an efficiency of about 98% as with single-stripe diodes. However, because of the relatively large size of the emitting area ($\sim 100 \mu\text{m}$ long) coupling into small core fibers is difficult. In fact, the spatial incoherence of this

source prohibits efficient coupling into fibers with cores much smaller than 100 μm .

Coupling tests were performed with a 200 μm core diameter, .3 N.A. glass fiber with polished ends. The LD beam was recollimated and then focused with two objectives, O_1 and O_2 , respectively. We show in TABLE 12 the maximum power measured at the fiber output end (at full diode current) for different objective combinations. The coupling efficiency refers to the fractional amount of light transmitted by the second objective (O_2) that is actually coupled into the fiber. The divergence of the recollimated beam had to be adjusted in each case to optimize the transmitted power, so that in general a fair amount of power was apertured by the second objective and lost. This explains why the overall coupling efficiency (from LD to fiber output) was relatively low, at best 27%.

TABLE 12
COUPLING DATA FOR LASER DIODE #X-2

O_1/O_2	$P_{\text{out,max}}$ (mW)	Coupling Efficiency
10x/10x	< 10	< 10%
44x/20x	31.5	39%
20x/20x	34	47%
20x/44x	30	45%
20x/5x	27.5	42%

The maximum coupling efficiency was achieved when the two objectives had identical focal length. This result was expected since, in principle, this imaging system has a magnification of unity. The image of the diode emitting area formed on the fiber input end then has the same size as the diode junction ($\sim 100 \mu\text{m} \times .5 \mu\text{m}$). The reason why the 20x/5x and 20x/20x combinations give essentially the same result was, however, not clearly understood. Our results are however compatible with the $\sim 50\%$ coupling efficiency observed by Scifres and co-workers by butt-coupling a similar LD to a $100 \mu\text{m}$ core .3 N.A. fiber (Reference 20).

Finally the absorption coefficient of Nd:YAG at the laser diode wavelength at maximum current was measured to be about 1.75 cm^{-1} . This suggests that the diode wavelength is not quite, but fairly well, optimized to the peak of absorption of Nd:YAG. Small amounts of feedback were also found to modify the laser wavelength, although to a lower extent than the single-stripe LD from Hitachi.

C. LD-PUMPED FIBER LASERS

In this section we report measurements performed on LD-pumped Nd:YAG fibers, using the single-stripe diode from Hitachi (Sections 1 through 4) and the multiple-stripe diode from Xerox (Section 5).

1. Fiber Lasers

Measurements on Nd:YAG fiber lasers pumped with Hitachi LD #H-2 ($\lambda_{p2} \approx 820 \text{ nm}$) were performed on fibers of array #2 ($\sim 230 \mu\text{m}$ in diameter, 4 mm in length). The highly-diverging output beam of the diode was recollimated with a 20x microscope objective, so that the available pump power was about 75% of the emitted power, or $\sim 11 \text{ mW}$ at full diode current. The

fiber array was placed in a laser cavity made of two flat mirrors (HR and $T_1 = 1\%$), as done during previous measurements (see SECTION IV-A-1).

To facilitate laser cavity and pump beam alignment, the fiber was co-pumped with the beam of a cw argon-ion laser ($\lambda_{p1} = 514.5 \text{ nm}$) using the arrangement shown in Figure 35. The recollimated laser diode beam is focused with a lens L_2 (focal length f_2) and launched into the selected fiber through the high-reflecting mirror. The argon laser beam, after proper optical isolation, is fed into the fiber through the output coupling mirror using a lens L_1 ($f_1 = 98 \text{ mm}$) . The output beam from the fiber laser ($\lambda_s = 1.064 \text{ }\mu\text{m}$), recollimated by the lens L_1 , is diverted towards an infrared camera and TV monitor with a dichroic filter ($T \approx 80\%$ at 514.5 nm , $R \approx 99.5\%$ at $1.064 \text{ }\mu\text{m}$).

Before introducing the fiber in the cavity the two pump beams are carefully positioned to be coaxial. This alignment is refined after placing the fiber in the pump path. Cavity alignment then proceeds as follows. The mirrors and fiber are first aligned to yield minimum threshold under the pumping action of the argon laser alone. In a second step, the spatial alignment and launching efficiency of the laser diode beam are refined by using both pump beams and observing the reduction in argon-laser threshold power caused by the presence of the laser diode beam. The argon-laser power is thus gradually reduced until laser action is obtained with the laser diode pump alone. The optical alignment is then adjusted for maximum fiber laser output power (or lowest threshold).

Using this procedure, laser oscillation under the pumping action of the laser diode alone was observed in several fibers of array #2, although most subsequent measurements were performed in fiber #2-11. By repeating the

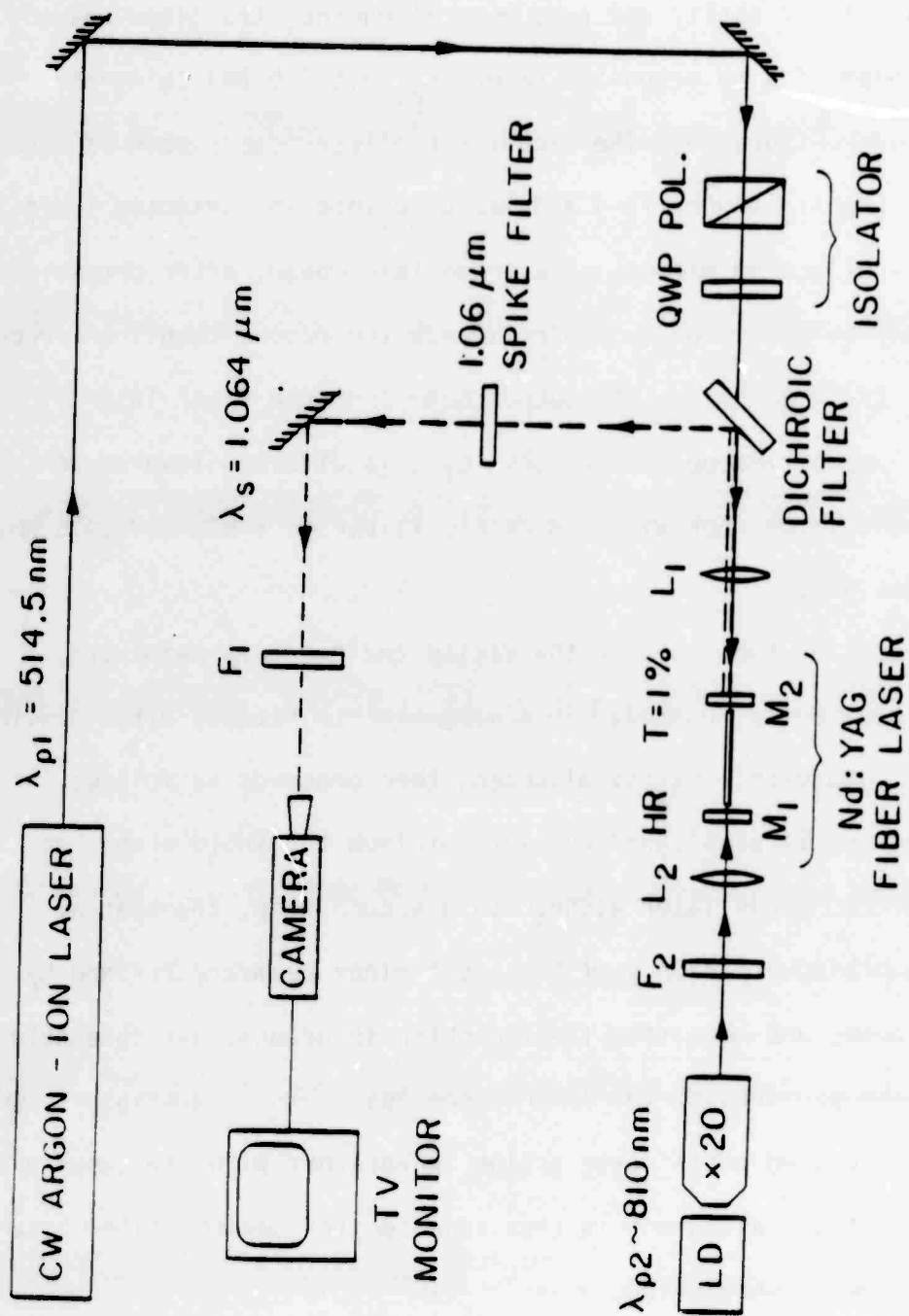


Figure 35--Experimental Arrangement used to Pump Nd:YAG Fiber Lasers with a Laser Diode and/or an Argon-Ion Laser.

alignment with different focusing lenses (L_2) the focal length which gave the best results was found to be $f_2 = 45$ mm (this value depends, of course, on the degree of recollimation of the laser diode beam).

For the purpose of fiber laser characterization, the pump power incident on the fiber was varied using a neutral density attenuator rather than current control. The reasons for this choice are two-fold. First, a diode current change induces a pump wavelength shift and a variation of the fractional amount of pump power absorbed by the fiber. Second, in the setup used for these measurements, current control was achieved by means of a trim potentiometer placed in the same unit as the laser diode itself, so that adjustment of the current also spoiled the optical alignment. The current was thus set at its maximum value and a variable neutral density wheel was placed in the path of the pump beam. This wheel has a variable optical density which increases linearly along its perimeter from zero to $\sim 2-3$. By rotating the wheel about its axis, the pump power could thus be varied without upsetting the optical alignment.

The lowest observed threshold was $P_{th,abs} = 3.9$ mW, corresponding to a pump power incident on lens L_2 of 6.9 mW. The estimated fractional power absorbed by the fiber was $\sim 56\%$ of the power launched into the fiber, corresponding to an absorption coefficient $\alpha_{abs} \approx 2.1 \text{ cm}^{-1}$.

The output power dependence on the pump power was obtained by measuring the output power from the fiber laser downstream from the $1.064 \text{ }\mu\text{m}$ spike filter (see Figure 35) while the pump power was increased. The output power was displayed on a chart recorder as the optical density wheel was slowly rotated with a DC motor. A typical output curve is shown in Figure 36. It shows a very nearly linear growth of the output power with increasing pump

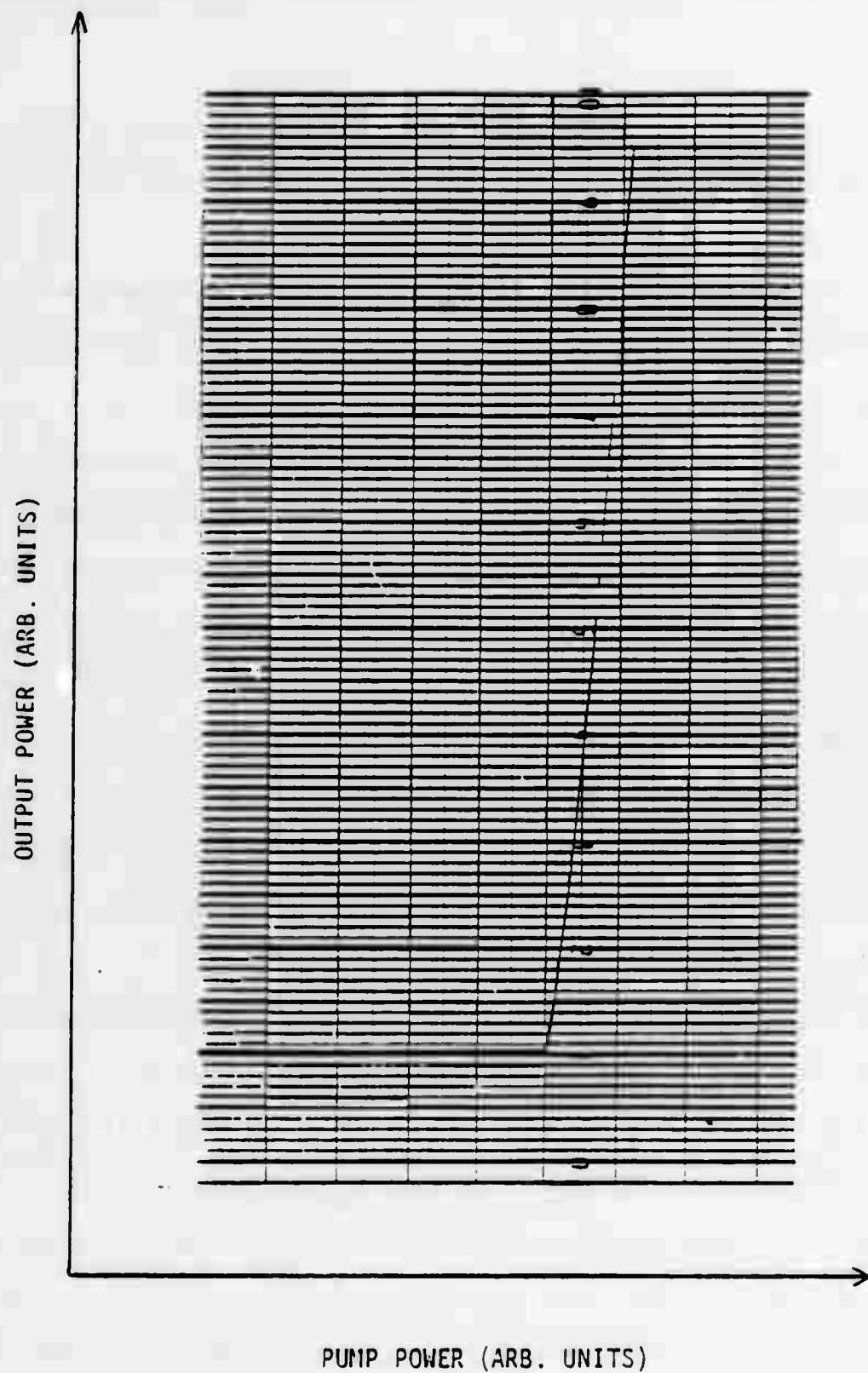


Figure 36--Output Power Curve of Fiber Laser #2-11 pumped with a Single cw Laser Diode.

power. These curves were calibrated by performing individual absolute measurements of the threshold and maximum output power. Figure 37 shows an expanded version of the response curve of Figure 36 after proper calibration. In this particular measurement the absorbed pump power at threshold was 4.2 mW, and the maximum fiber laser output power was .2 mW. The slope efficiency, measured from Figure 37 was 9.5% (with a $T_1 = 1\%$ output coupler). The value of the round-trip cavity loss δ_0 inferred from this efficiency, given by [Eq. (25)], is $\delta_0 \approx 8.1\%$. Assuming a value of $2.2 \times 10^{-4} \text{ cm}^2/\text{watt}$ for the gain coefficient κ (compatible with 1.38×10^{-4} at 514.5 nm), we obtain an effective pump mode area $A_p^* = 2.3 \times 10^{-5} \text{ cm}^2$.

Note that from these results we can extrapolate that with a 5% output coupler the threshold would be about 6.3 mW, with a slope efficiency up to 27%. Using a laser diode emitting 50 mW and the same experimental arrangement, the maximum fiber laser output power would be about 5 mW. This suggests that at least a few milliwatts of power at 1.064 μm should be obtainable from these fiber lasers when implementing the high-power diodes from Xerox.

2. Comparison between LD and Argon Laser Pumping

Comparison between the operation of a given fiber laser pumped at $\lambda_{p1} = 514.5 \text{ nm}$ and $\lambda_{p2} = 820 \text{ nm}$ yielded important information on the efficiency of laser diode pumping. From our theoretical model alone we expect the laser threshold to be proportional to A_p^*/λ_p , and its slope efficiency to be proportional to λ_p (see SECTION III-B). Therefore for a given fiber

LD-PUMPED FIBER LASER OUTPUT

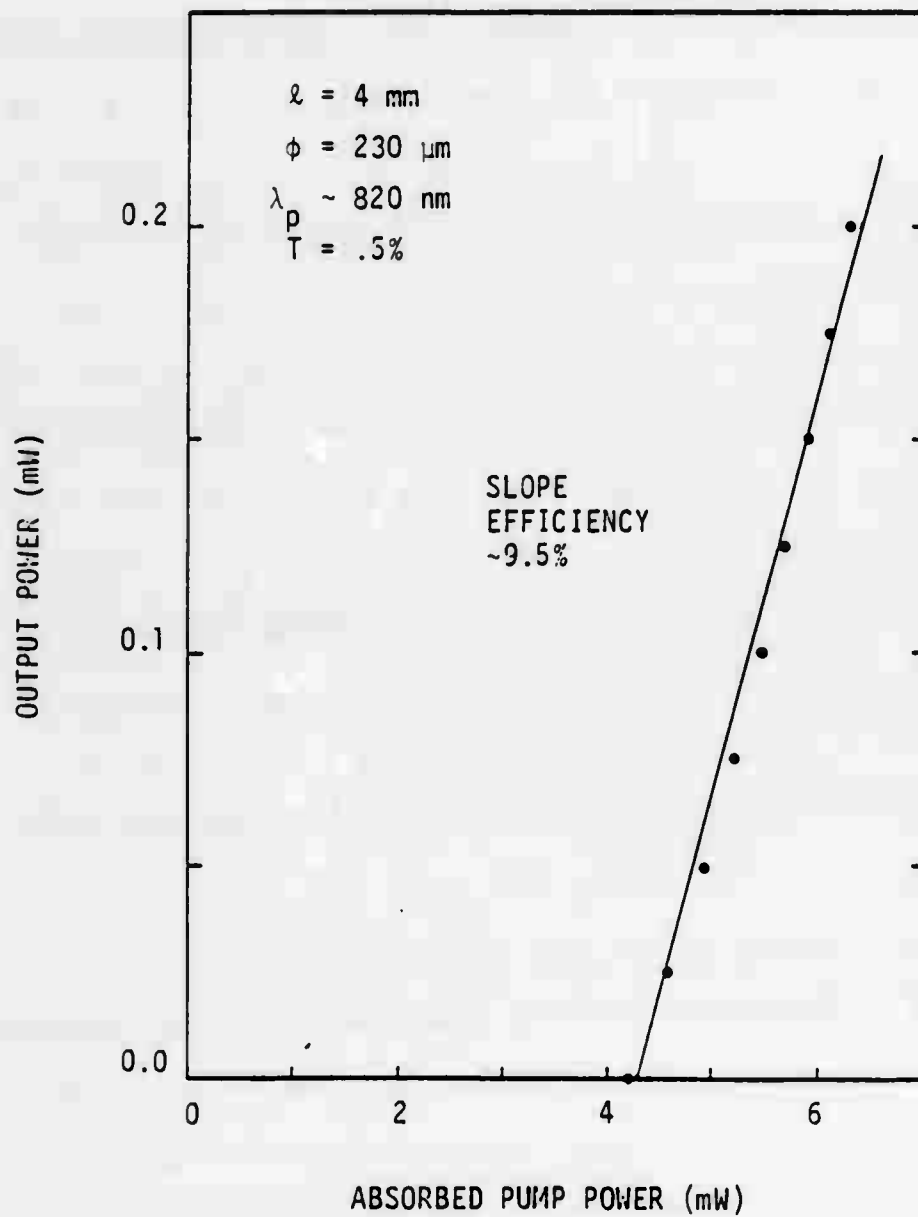


Figure 37--Same as Figure 36, after Calibration.

laser, the ratio of the thresholds when pumped with λ_{p1} and λ_{p2} should be

$$R_{th} = \frac{P_{th,1}}{P_{th,2}} = \frac{\lambda_{p2}}{\lambda_{p1}} \cdot \frac{A_{p1}^*}{A_{p2}^*} = 1.59 \frac{A_{p1}^*}{A_{p2}^*} \quad (54)$$

while the ratio of slope efficiencies should be

$$R_s = \frac{s_1}{s_2} = \frac{\lambda_{p1}}{\lambda_{p2}} \sim .63 \quad (55)$$

Threshold measurements repeatedly indicated that the ratio of thresholds was significantly smaller than the maximum anticipated value of 1.59 [see Eq. (54)]. This suggested that the laser diode effective pump mode area A_{p2}^* was not optimized to its minimum possible value, which prompted a systematical investigation of the optimum focal length for the focusing lens L_2 (see Figure 35). However, even with the optimum lens ($f_2 \sim 45$ mm in our particular experiment arrangement) R_{th} was still measured to be in the range of .65 to .81.

This discrepancy was attributed to the astigmatism of the laser diode beam. In essence, the astigmatism between the parallel (parallel to the plane of the diode junction) and the perpendicular (perpendicular to the junction) directions results in dissimilar focusing properties in these two directions, which in turn prevents simultaneous optimum beam focusing in both directions. Astigmatism affects pump focusing in two ways. First, because of wavefront curvature astigmatism the locations of the two waists W_{\parallel} and W_{\perp} inside the crystal or fiber no longer coincide. Second, because of astigmatism in the beam dimensions, those two waists cannot both have the same minimum value.

The magnitude of the first effect was estimated by using Gaussian mode propagation theory. Although an exact calculation is made difficult by our lack of knowledge of the diode beam characteristics, the study of reasonable extreme cases shows that this effect is fairly small. For typical diode parameters (waist radii of 2-5 μm in one direction, and 10-100 μm in the other direction), and for the parameters of our own experiment, we found that the distance Δ between the waist locations inside the laser material is in the range of 0-3 mm. This value is smaller than the pump Rayleigh range (or fiber length) and is not expected to significantly affect the pump-to-signal mode overlap and laser operation.

Analysis of the second effect, developed in APPENDIX F, shows that the minimum achievable pump spot size $\bar{A}_{p,\text{opt}}$ is increased by astigmatism in the beam dimension in a predictable manner. It depends on the pump astigmatism $x = W_{\perp}/W_{\parallel}$ as follows:

$$\bar{A}_{p,\text{opt}} = \frac{\pi(1+x^2)}{2x} \sqrt{\frac{\lambda_p^2 L^2}{3\pi^2 n^2}} \quad (56)$$

i.e., it is minimum for $x = 1$ (circular mode) and increases when x departs either way from this value.

For the fiber lasers tested, $L = 4 \text{ mm}$ and $n = 1.82$, while the laser diode astigmatism was visually estimated to be $x = 1/4$. The calculated optimum pump waists are then $W_{1,\text{opt}} = 14.4 \mu\text{m}$ [Eq. (F-7)] and $W_{2,\text{opt}} = 37.5 \mu\text{m}$ [Eq. (F-6)]. Taking the signal mode radius to be $W_s = 31 \mu\text{m}$, as measured previously in fibers of array #2 (see Section IV-B-3), we obtain from Eq. (F-9) the value of $R_{th} = .80$.

This result compares well with our measurements, which indicated values between .65 and .81. The scatter in our measurements is probably due to a residual misalignment of the fiber laser cavity with respect to one of the pump beams. The similarity of theoretical and experimental results is, however, good enough that we are confident we understand the mechanism involved here.

The value of A_p^* calculated from this mode is $A_p^* = \pi/2(31^2 + 37.5^2) \times 10^{-8} = 3.87 \times 10^{-5} \text{ cm}^2$ for this particular laser. It agrees well with the value derived from laser measurements ($A_p^* = 2.3 \times 10^{-5} \text{ cm}^2$). This simple model of pump beam astigmatism is therefore quite satisfactory.

The fiber laser slope efficiency ratio R_s was also observed to follow theoretical predictions. In the particular example of the laser characterized in Figures 36 and 37, the slope efficiency was about 4-5% when pumped with 514.5 nm, versus $\sim 9.5\%$ when pumped at ~ 820 nm. Again the slight difference between this experimental value $R_s = .47$ and the theoretical value of .63 [Eq. (55)] is probably due to a residual cavity misalignment. This result provides an experimental demonstration of the greater energy conversion efficiency of Nd:YAG fiber lasers when pumped via the ~ 810 nm absorption band.

3. LD-Pumped Bulk Nd:YAG Lasers

To obtain a useful comparison with fiber laser performance, we also investigated the characteristics of a laser diode-pumped bulk Nd:YAG laser. Crystal #4 was used for these measurements (see TABLE 4). This crystal, doped with .9% of neodymium, is 2 x 6 mm in area and 4 mm thick. The two faces perpendicular to the laser direction (crystal thickness) were polished and left uncoated for laser operation. The crystal was placed in a cavity made of

two $R = 10$ cm mirrors, namely a high-reflector and a .5% transmitter. The same experimental arrangement described earlier (Figure 35) was also used for laser tests.

Following the alignment procedure outlined earlier, laser action was obtained very easily in this crystal. The threshold was brought down to as low as $P_{th,abs} \approx 1.5$ mW, corresponding to 4.7 mW of pump power incident on lens L_2 . The average measured value of the crystal absorption coefficient at the laser diode wavelength at full current was about 1.9 cm^{-1} .

Figure 38 shows the output power curve of this laser when operated with a .5% transmitter. In this particular measurement, alignment was somewhat less than optimum, with a threshold $P_{th,abs} = 2.1$ mW. The maximum output power at $1.064 \text{ }\mu\text{m}$ was .8 mW at maximum pump power ($P_{abs} \approx 4.6$ mW), corresponding to a slope efficiency of 33%. The laser cavity total round-trip loss calculated from these data is $\delta_0 = 1.2\%$. Subtracting mirror transmission (.5% and .1%) we obtain a single-pass crystal loss of about .3%, including residual Fresnel loss at the uncoated crystal faces.

In a second set of measurements, a 1% transmission output coupler was used as a better match to the crystal loss. The mirror curvature was flat ($R = \infty$) while the high reflector was unchanged ($R = 10$ cm). The threshold was then $P_{th,abs} = 1.7$ mW, and the maximum output power 1.63 mW at 4.1 mW of absorbed pump power (Figure 38). The slope efficiency was thus about 63%, compared to the maximum achievable efficiency of $.82/1.064 = 77\%$. In this configuration, over 80% of all absorbed pump photons were transformed into coherent output photons. At maximum output power the $1.064 \text{ }\mu\text{m}$ beam had the same linear polarization as the pump laser, as expected. It was also running in the fundamental spatial mode, with no observable astigmatism (as

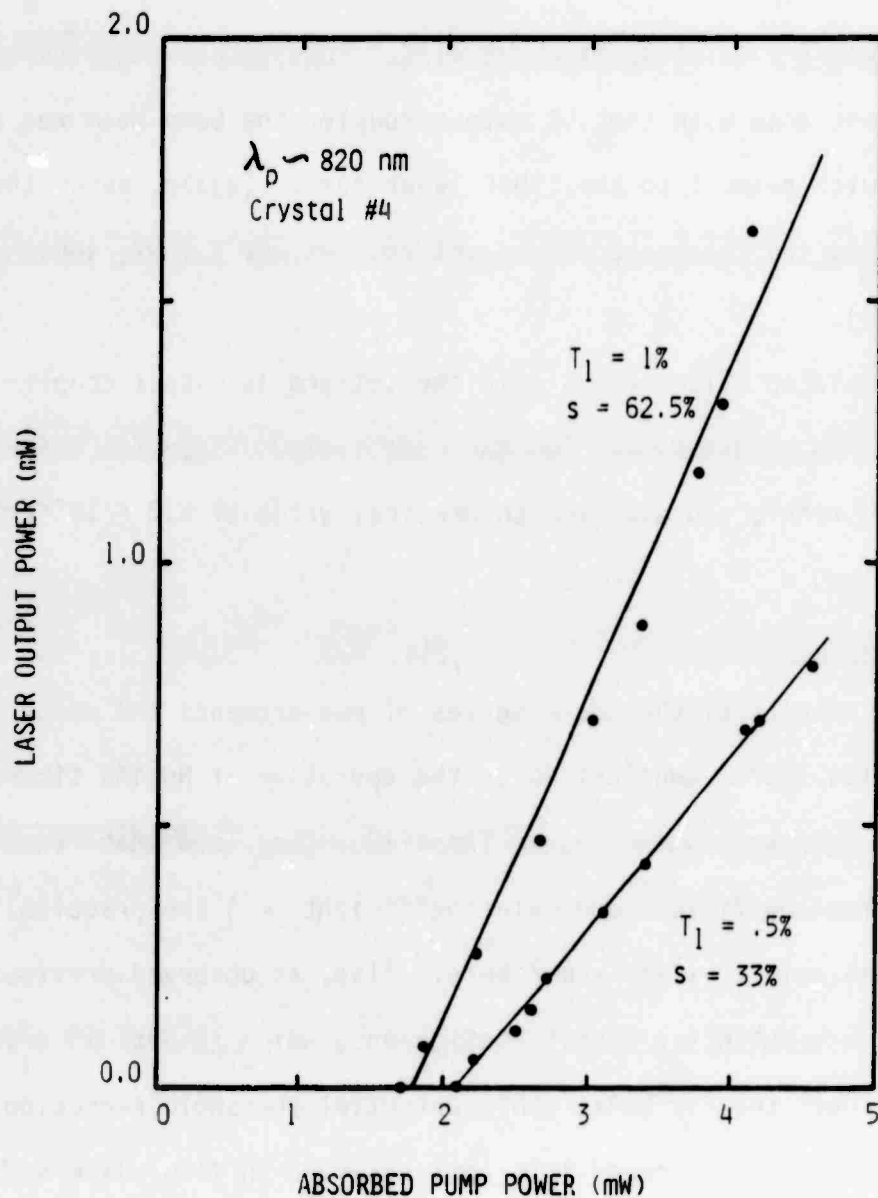


Figure 38--Output Power Curves of a Miniature Nd:YAG Laser (Crystal #4) pumped with a Single cw Laser Diode.

anticipated, the mirror curvature eliminates astigmatism by focusing the signal beam equally well in all directions). Higher order modes were also observed by offsetting the cavity with respect to the pump beam.

The cavity loss inferred from the laser efficiency is $\delta_o = 1.23\%$, or a single-pass crystal loss of about .12%. This figure suggests that in the measurement done with the .5% output coupler the pump beam was not perfectly aligned with respect to the fiber laser cavity (again, under the best conditions, the threshold with a .5% coupler was 1.5 mW, versus 2.1 mW in Figure 38).

Calculated values of A_p^* in the .5% and 1% output coupler lasers are $7.9 \times 10^{-5} \text{ cm}^2$ and $6.0 \times 10^{-5} \text{ cm}^2$, respectively. These two values agree well with each other, and with the theoretical value of $6.3 \times 10^{-5} \text{ cm}^2$ ($W_s \approx 51 \text{ } \mu\text{m}$, $W_p \approx 37.5 \text{ } \mu\text{m}$).

4. Discussion

The results of the above series of measurements and comparison between them yields useful conclusions on the operation of Nd:YAG fiber lasers. Measured data are summarized in TABLE 13. They show that laser parameters (absorption coefficient and gain coefficient κ) are practically identical for Nd:YAG bulk crystals and fibers. Also, as observed previously, the fiber provides a substantial signal confinement, which results in a lower value of A_p^* in fibers than in bulk. This potential threshold reduction is however offset by the higher round-trip loss observed in fiber lasers, on the order of 10 to 30 times larger than in bulk. We refer the reader to the next section of this report for further discussion on the subject of fiber loss.

TABLE 13
MEASURED PARAMETERS OF BULK AND FIBER Nd:YAG LASERS
($\lambda_p \sim 820 \text{ nm}$)

LASER TYPE	α_{abs}	κ (cm^2/W)	A_p^* (cm^2)	δ_o (dB/cm)
BULK (crystal #4)	1.9 cm^{-1}	$4 \pm 2 \times 10^{-5}$	$\sim 7 \times 10^{-5}$.013 - .033
FIBER (#2-11)	2.1 cm^{-1}	$\sim 4.2 \times 10^{-5}$	$\sim 3 \times 10^{-5}$.40

Finally we should point out that both bulk and fiber lasers showed quite stable output powers when operated with a laser diode. Minor amounts of optical feedback from the fiber laser optics into the laser diode provided a convenient means of shifting the laser diode wavelength and of optimizing it to a peak of absorption of Nd:YAG. After several hours of continuous operation at full diode current the fiber (or bulk) laser output was essentially unchanged. Any noticeable drift from one day to the next was due to a gradual misalignment of the laser cavity. This misalignment is expected to disappear in future fiber laser cavities in which the mirrors will be directly bonded onto the fiber ends.

5. LD-Array-Pumped Lasers

Using the experimental setup described in Figure 35, laser action was observed in crystal #4 pumped with a laser diode array (#X-2). The laser cavity was made of an HR and a .5% output coupler, both with a radius of curvature of 10 cm. Various combinations of recollimating and focusing optics O_1/O_2 were tested. The best results were obtained when the LD beam was recollimated with a 44x objective (O_1) and focused into the crystal with a 45 mm lens (O_2).

Threshold was reached at a current of 390 mA, or a pump power incident on lens O_2 of 31 mW. To optimize the pump spot size in the crystal the beam incident on lens O_2 was made slightly diverging, so that this lens transmitted only half of the incident power. Using the measured absorption coefficient of 1.4 cm^{-1} , the absorbed power at threshold was estimated to be 5.5 mW. At full current the maximum Nd:YAG laser output power was 3.4 mW, corresponding to a slope efficiency of 17.5%.

As the diode current was increased from its threshold value (the current control knob of this power supply is mechanically uncoupled from the laser diode) the Nd:YAG laser output power was observed to increase and vanish a few times before finally increasing steadily to its maximum current value. These cancellations were attributed to a shift of the diode wavelength which occurs as the current is increased and the junction temperature rises. As the pump wavelength scans the absorption spectrum of Nd:YAG, the fractional absorbed pump power P_{abs} varies greatly and fluctuates from above to below the threshold value P_{th} . This effect is, however, not serious for practical applications of fiber lasers since laser power control can be achieved by other means, for example externally.

Comparison of the laser operation of crystal #4 pumped with a single-stripe diode or with a diode array yields interesting conclusions. First the threshold is about 3.7 times higher when pumped with the array. Reference to Eq. (56) suggests that the astigmatism of the array is probably responsible for most of the threshold increase. In physical terms, the outermost lasers of the diode array produce beams which are focused at a large angle to the Nd:YAG laser axis, and to a large extent the power they carry does not contribute to the Nd:YAG laser gain. The threshold increase indicates an astigmatism $x \approx 1/16$ for the diode array, in agreement with direct measurements. Also, the slope efficiency is lower than observed with the single-stripe diode pump (17.5% versus 33%). Again this is due to the large astigmatism of the pump beam, as shown in APPENDIX F (off-axis LD beams are focused at a large angle and overlap poorly with the signal beam).

Laser action in Nd:YAG fibers of array #2 pumped with the diode array has not been observed so far, although some cooperative effect with the 514.5 nm pump beam was observed. We believe this situation is due to several reasons. First, for reasons exposed earlier, the pump beam could not be focused tightly enough, and a large fraction of the available pump power was not coupled into the fiber (see SECTION V-B-2). Second the fractional coupled power has a very strong astigmatism, as described above. Finally these measurements were performed at the end of this contract and more extensive tests were precluded by time constraints.

However, we believe the present situation can be improved by at least partially correcting the astigmatism of the diode array beam. Initial attempts at correcting the astigmatism of single-stripe diodes with cylindrical lenses are in fact encouraging (this correction was successfully

achieved at the Xerox Research Center (Reference 24). Also, the use of phase-locked arrays should allow much tighter focusing. Finally, the implementation of fiber lasers with bonded mirrors will enable us to use shorter focal length lenses to focus the pump beam and couple efficiently into crystal fibers.

SECTION VI

FIBER LASER LOSS ANALYSIS

Comparison of the results obtained with bulk and fiber lasers have shown throughout this work that two major differences exist between these lasers. First, mode confinement, and consequently the gain per unit pump power, is much greater in fiber than bulk devices. Second, the round-trip cavity loss is several times larger in fiber than in bulk lasers. These two differences were in general such that fiber lasers were not as efficient at converting pump photons into signal photons as bulk lasers. During the second half of this contract a significant effort was therefore devoted to the investigation of the origin of this higher loss. A number of potential loss mechanisms were identified, which can be divided into three main categories. The first category, referred to in the following as optics-related mechanisms, includes the mechanisms related to the various optical surfaces encountered by the optical signal and their respective alignment. The second category incorporates all material-related mechanisms, in particular the potential differences in structure and laser properties that may exist between Nd:YAG fibers and bulk crystals. The last category includes fiber-related mechanisms, i.e., loss mechanisms resulting from less than ideal waveguide properties.

Extensive efforts were made to characterize each of these mechanisms and estimate their relative magnitude. This effort was quite successful, and led to the identification of what we believe are the two dominant loss mechanisms in the fiber lasers described here. The first one is aperturing of the signal mode by the fiber. The second mechanism is residual crystal bulk defects in larger diameter fibers. We report in this last section the series of observations and measurements that led to these conclusions.

A. OPTICS-RELATED LOSS MECHANISMS

1. End-Face Scattering

Imperfections in the polishing of the end-faces of the fiber or in its AR-coating can introduce signal loss by distorting the phase-front of the optical signal, which then cannot constructively interact with itself. This was observed in fiber array #1 which was the first array fabricated by our polishing method and showed a higher degree of end-face imperfections in earlier work. After a second polishing, the fiber end quality turned out to be more uniform, and the fiber ends showed better edge definition. As a result, most of the lasers of this array exhibited improved performance.

2. Mirror Defects

Mirror surface defects and coating quality, which can introduce loss through scattering or less than ideal reflectance, were thought for some time to be a significant source of loss. However, by interchanging miniature mirrors and curved mirrors in several fiber lasers no differences in operating characteristics were noted. We believe all mirrors used had as good a quality as could be.

In subsequent arrays, end polishing was carefully controlled by visual observation before placing the fibers in a laser environment. By placing a drop of index-matching liquid ($n \approx 1.5 - 1.7$) between each fiber end and mirror in different non-AR-coated fiber lasers, we observed in general no measurable improvement in laser performance. These results clearly indicated that in most cases (a) the mirror reflectivity is not affected by the liquid, (b) as described earlier a careful cavity alignment can essentially phase-match Fresnel reflections to the main reflections, (c) the end-faces of the fibers do not contribute to much scattering (it would otherwise be reduced by

the liquid matching effect, which would show up as a reduced threshold).

It is worth noting here that it was our impression throughout this work that the use of liquids was not adequate for the kind of power levels at which lasers were routinely operated. Most liquids vaporize in a few seconds under the impact of 100 mW or more of pump power ($\lambda = 514.5$ nm). Also, because of the relatively high threshold and incident pump power, thermal instabilities developing within the liquid often prohibited lasing action. The only improvement observed (in fibers of array #2) was a greater mechanical stability and ease of adjustment, as expected. This advantage is however relatively minor compared to the new problems introduced by the presence of a liquid in the optical cavity.

3. Cavity Alignment

A less than ideal cavity alignment can significantly reduce the signal build-up. An important aspect of cavity alignment also involves the alignment of the pump and signal beams, which must be coaxial to take full advantage of the available optical gain, as shown earlier. Any relative offset or tilt will result in a lower gain (higher threshold) and lower slope efficiency, i.e., a lower apparent round-trip loss (see APPENDIX D). Similarly, fiber ends should be parallel to each other and perpendicular to the fiber axis in order to minimize additional losses due to odd incidence angles at the mirrors and fiber ends. We noticed that non-parallel fiber ends and fiber tilts introduce significant additional loss - if any because tilting the mirrors to compensate for odd angles prevent bringing the finite-size mirrors as close to the fiber ends as can be. Also, bends in the crystal fiber are expected to introduce coupling of the signal mode to higher order modes in a guided configuration, and some degree of mode clipping in an unguided configuration.

However, we believe that our fiber processing and mirror alignment procedure is good enough that such effects are negligible in the present configurations of the fiber lasers, as demonstrated by the high performance of bulk lasers processed and aligned in a similar manner.

4. Mode Coupling

The different intensity distributions of the guided fiber mode and the unguided spatial mode (between the mirrors and the fiber ends) existing in the cavity make coupling from one to the other at the fiber-air (or liquid) interface less than unity. In this case loss can result from scattering into other modes. Analysis of LP_{01} -to- TEM_{00} Gaussian mode coupling shows that this effect can amount to 1% per pass (4% per round-trip). This effect may actually not be so disastrous in the case of thin mirror-to-fiber spacings because of evanescent coupling.

The situation is more favorable in guided fibers supporting Gaussian modes (waist radius W_0). The loss mechanism is then associated with the change in waist radius and curvature of the signal mode as it travels from the fiber end to the mirror and back. Theoretical analysis then shows that in the case of flat (or nearly flat) mirrors, this loss can be kept to a minimum by reducing the fiber end-to-mirror spacing below an adequate value. As a useful result we reproduce here the approximate form of the coupling loss experienced by the signal mode at each mirror:

$$\Delta T = \left(\frac{\lambda_s h}{\pi n W_0^2} \right)^2 = \left(\frac{h}{Z_R} \right)^2 \quad (57)$$

where h is the fiber end-to-mirror spacing, n is the index of the medium between fiber and mirror, and $Z_R = \pi n W_0^2 / \lambda_s$ is the signal Rayleigh range

(outside of the fiber).

For example, in an unclad fiber of diameter $d = 100 \mu\text{m}$, the guided mode radius is approximately $W_0 = 32 \mu\text{m}$, and losses are brought below $\Delta T = .1\%$ (.2% on a round-trip) by making the fiber-to-mirror spacing smaller than $h \approx 100 \mu\text{m}$ (assuming air is in this spacing).

In all our measurements fiber-to-mirror spacings were made quite small, often to the point where the mirror was contacting the fiber holder. We therefore believe coupling losses were quite small. Again the fact that high-performance bulk lasers were demonstrated with similar spacings confirms this belief.

3. MATERIAL-RELATED LOSS MECHANISMS

1. Solarization

A potential material-related loss mechanism is solarization of the fiber material under the impact of ultraviolet radiation (Reference 25). Solarization of the laser material from exposure to the uv fluorescence light from the argon-ion laser tube or from the uv lamp during epoxy curing would induce crystal damage essentially irreversible at room temperature. This mechanism seems however rather unlikely, since it generally occurs in Nd:glassess but is minimal in Nd:YAG. In bulk Nd:YAG lasers pumped with flash lamps, no significant crystal damage due to solarization is visible after hundreds of hours of operation, although flash lamps emit a considerable amount of ultraviolet light. Although this uv light is generally filtered before reaching the YAG rod to reduce heating effects, a flash lamp-pumped rod probably receives a far greater amount of uv radiation than our samples do during epoxy curing.

2. Pump Quantum Efficiency

It was also suggested that 500 nm pump photons may have a lower pumping efficiency than longer wavelength (such as ~ 810 nm) photons, but our own measurements in 514.5 nm pumped miniature Nd:YAG lasers rule out this possibility. In these bulk lasers we observed a slope efficiency as high as 43.6%, i.e., a photon conversion efficiency of 90%, which indicates that the pumping efficiency of 514.5 nm photons in Nd:YAG is at least as high as 90%. However, we should mention that we observed that the pumping efficiency of 488 nm photons (also from an argon-ion laser) may be as much as 50% smaller than that of 514.5 nm photons. This is to be correlated to other authors' observations that the blue lines of cw krypton lasers ($\lambda \sim 470$ nm) were not nearly as efficient as the 752.5 nm line for pumping Nd:YAG (Reference 25).

3. Nd-Concentration

The important issue of the actual concentration of Neodymium present in CMR-grown Nd:YAG fibers was raised early in this work. This concentration plays an important role in the laser overall performance as it affects simultaneously the crystal quality, the material absorption coefficient, its fluorescence lifetime and stimulated emission cross-section. In cw YAG lasers the optimum concentration of Nd is approximately 1%, although slightly lower concentrations are sometimes preferred as they yield better optical quality crystals. This value provides a good compromise between low threshold and efficient pump absorption. In general, low-threshold operation is achieved for Nd-concentrations between .5 at.% and 1.4 at.%. At a concentration of $\sim 2\%$ the combined effect of poorer crystal quality and lower gain per unit pump power results in a threshold approximately 10 times higher (Reference 12).

Although other authors have shown that the concentration of Nd in Nd:YAG fibers is essentially unaffected by successive regrowths of the fiber (Reference 4), it was still interesting to attempt verifying this fact for CMR-grown fibers. Three methods were used for this purpose, namely mass-spectroscopy, fluorescence lifetime measurements and fluorescence spectra measurements.

(a) Mass-spectroscopy Analysis

A selection of fibers with different diameters was sent to an outside facility for mass-spectroscopy measurements. However, during the vaporization stage the fibers sprang out of their crucible and were lost. Only the larger diameter source rod yielded any useful result, not yet communicated to us. Further attempts will be made using crushed fibers to avoid the loss of fiber. This method should yield very accurate data, with an absolute error smaller than .1%.

(b) Fluorescence Lifetime

The second method relies on the measurement of the fluorescence lifetime of excited Nd-ions, which becomes concentration dependent through quenching for Nd-concentrations larger than $\sim 1\%$. This lifetime was measured by exciting the fiber with low power ~ 4 msec pulses from an argon-ion laser (at $\lambda = 514.5$ nm) at a repetition rate of ~ 1 kHz. The fluorescence emission of the fiber is collimated with a microscope objective, filtered and detected with a germanium detector and displayed on an oscilloscope. A typical trace is shown in Figure 39(a). The upper trace is the pump pulse, the lower trace the fluorescence pulse. Figure 39(b) (concluded) shows the fluorescence tail (just after the pump pulse has been turned off), decaying exponentially as expected.

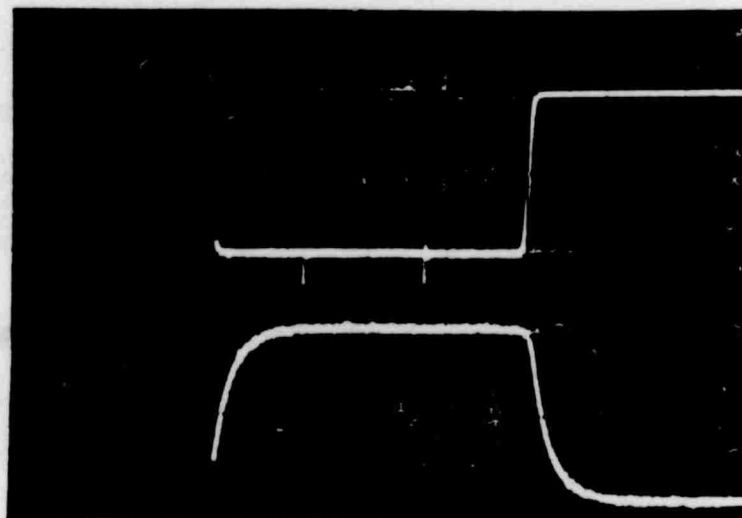


Figure 39(a)--Upper Trace: Pump Pulse fed into Single Crystal Fiber. Lower Trace: Fiber Fluorescence. Horizontal Scale: 1msec/div.

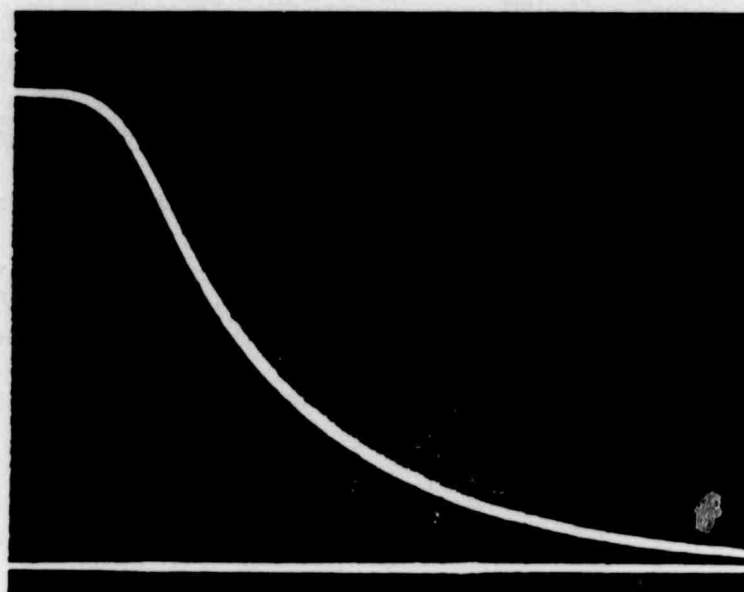


Figure 39(b)--Typical Decay of the Fluorescence emitted by a Fiber after Pump Turn-off (Fiber #3-4). Horizontal Scale: 100 μ sec/div.

In early measurements the pump pulses were produced by mechanically chopping the argon laser beam, which produced pulses with falltimes of 40-50 μsec , large compared to the fluorescence lifetime of Nd:YAG ($\tau_f \sim 230 \mu\text{sec}$). Measurements were repeated in which the mechanical chopper was replaced by an acousto-optic beam deflector for greater absolute accuracy. The detection system was also upgraded to a response time of $\sim 1 \mu\text{sec}$. The fluorescence lifetime τ_f was retrieved from fluorescence curves by fitting each individual curve to an exponential function $\exp(-t/\tau_f)$. Repeated measurements with this improved system showed a good reproducibility. Also, the oscilloscope time scale was checked to be accurate to better than 0.4%. The estimated error on the measured value of τ_f was $\pm 4 \mu\text{sec}$.

We summarize in TABLE 14 results obtained with fibers from several arrays, including BTL- and CMR-grown fibers, and bulk samples. The following remarks can be made from these results. First, BTL-grown fibers have about the same τ_f as bulk Nd:YAG. Second, some CMR-grown fibers show a lower fluorescence lifetime than expected, close to 210 μsec . A possible interpretation proposed earlier was that the concentration may increase with decreasing fiber diameter, as suggested by selected data points (Figure 40; Nd-concentrations were inferred from τ_f using published results (Reference 12). Since three growth iterations are required to go from a 1 mm source rod to a 100 micron diameter fiber, it suggests that the Nd-concentration increases by about 16% per growth. This figure is unusually high, and higher than the maximum value predicted by our fiber growth specialists ($\leq 10\%$). This hypothesis was further tested using Nd:YAG fibers of various diameters (50 μm , 100 μm , and 250 μm) grown successively from the same 500 μm ground

TABLE 14
SUMMARY OF FLUORESCENCE LIFETIME MEASUREMENT RESULTS

Origin	Fiber Number	Diameter (μm)	τ_f ($\pm 4 \mu\text{sec}$)
Bulk	Crystal #4		235
BTL	9-1	~ 65	236
BTL	9-4	~ 65	233
BTL	9-5	~ 65	226
BTL	9-7	~ 65	230
BTL	4-1	80	230
BTL	4-2	79	228
BTL	4-3	81	233
BTL	4-5	80	233
CMR	1-1	93	210
CMR	1-4	107	210
CMR	1-6	98	199
CMR	1-11	84	207
CMR	2-3	223	215
CMR	2-5	234	218
CMR	2-6	243	211
CMR	2-13	228	212
CMR	7-1	78	236
CMR	7-2	80	233
CMR	7-3	90	233
CMR	7-4	86	231
CMR	7-5	87	231
CMR	Grown	~ 500	220
CMR	from	~ 250	230
CMR	the same	~ 100	237
CMR	parent	~ 50	221

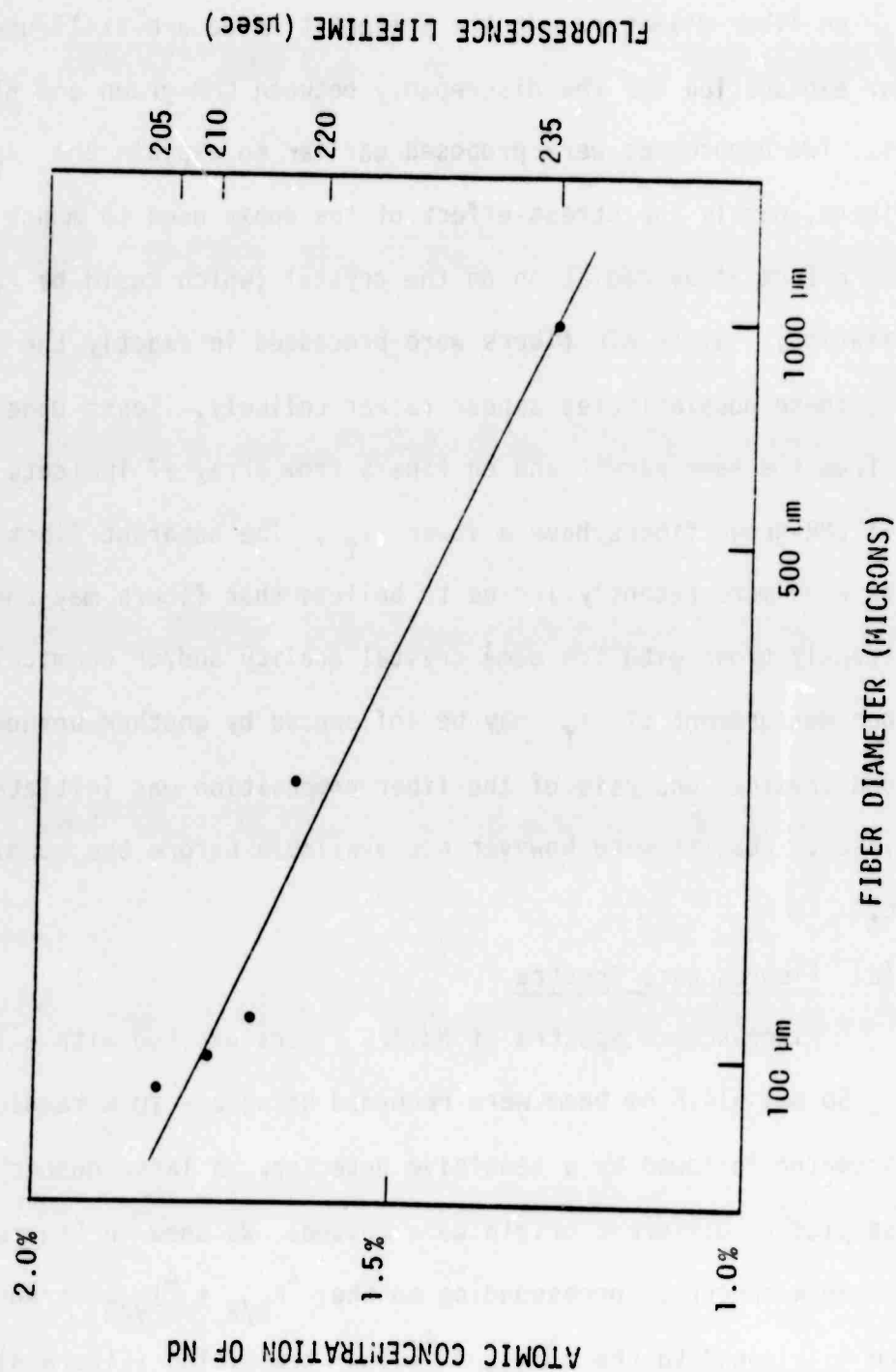


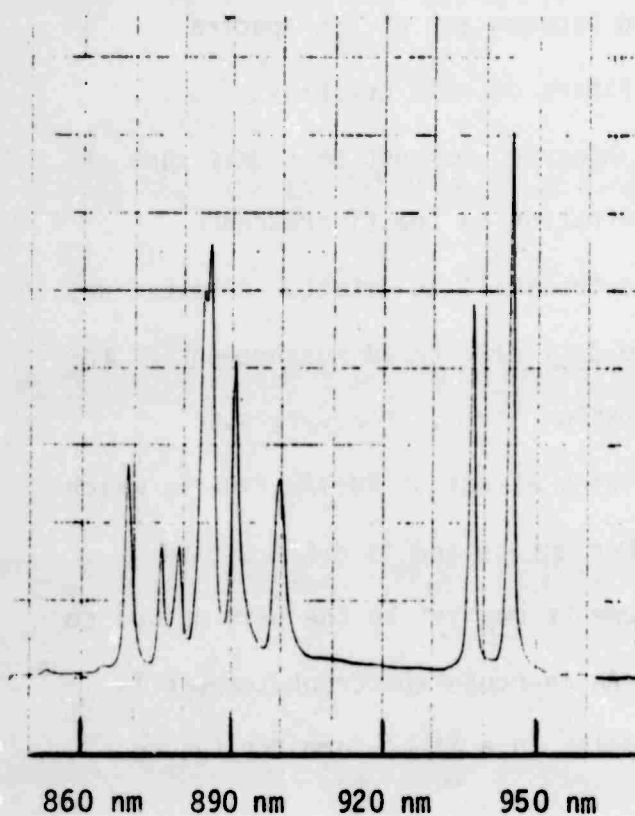
Figure 40--Nd-Concentration Measurements for In-House grown Nd:YAG Fibers.

source rod. They indicate that at least for some fibers τ_f is not strongly dependent on fiber diameter (see bottom of TABLE 14).

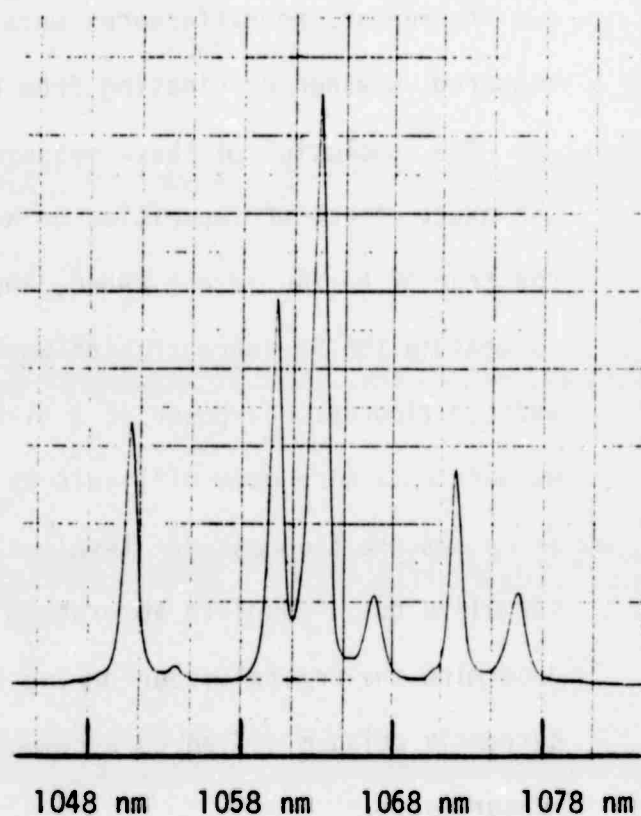
The results of these measurements are inconclusive as to the dependence of τ_f on fiber diameter. At the present time we are still unable to provide a clear explanation for the discrepancy between CMR-grown and BTL-grown Nd:YAG fibers. Two hypotheses were proposed earlier to explain the τ_f reduction in CMR fibers, namely the stress-effect of the epoxy used to mount the fibers, and the effect of uv radiation on the crystal (which could be related to solarization). Since BTL fibers were processed in exactly the same way as CMR fibers, these possibilities appear rather unlikely. Tests done on fibers grown from the same parent and on fibers from array #7 indicate however that not all CMR-grown fibers have a lower τ_f . The apparent fluctuations in our results have more recently led us to believe that fibers may not be consistently grown with the same crystal quality and/or chemical purity, or that our measurement of τ_f may be influenced by another unknown parameter. A second chemical analysis of the fiber composition was initiated to finalize this issue. Results were however not available before the submission of this report.

(c) Fluorescence Spectra

Fluorescence spectra of Nd:YAG fibers excited with a low power ($P_{abs} \leq 50$ mW) 514.5 nm beam were recorded using a ~ 10 Å resolution monochromator followed by a sensitive detector. A large number of fibers and bulk samples of different origin were tested. We show in Figure 41 typical fluorescence spectra, corresponding to the ${}^4F_{3/2} \rightarrow {}^4I_{9/2}$ transition (Figure 41(a)) and to the ${}^4F_{3/2} \rightarrow {}^4I_{11/2}$ transition (Figure 41(b)) (concluded). Comparison with published spectra shows no noticeable difference



(a)



(b)

Figure 41--Fluorescence Spectra of Nd:YAG Fiber #2-7 excited with ~40 mw at 514.5 nm. (a) ${}^4F_{3/2} \rightarrow {}^4I_{9/2}$ Transition ($\lambda \sim 900$ nm), (b) ${}^4F_{3/2} \rightarrow {}^4I_{11/2}$ Transition ($\lambda \sim 1060$ nm).

other than slightly broader fluorescence peaks in our spectra due to our instrument-limited resolution (Reference 26). After calibration, values of splitting ratios computed from these spectra for the various transitions of interest agreed well with published data. However, within the resolution of our instrument, no differences were noticed between any of the spectra measured, whether originating from Nd:YAG fibers or bulk crystals.

The conclusion of these measurements, however, may not be significant as the exact effect of impurities or Nd-concentration on the fluorescence spectrum of Nd:YAG is not known, and may be too small to detect. A better way to measure the Nd-concentration would be to do a calibrated measurement of the emitted fluorescence power at a given excitation level. However, such measurements were made difficult by the guiding effect of Nd:YAG fibers, which increases the fluorescence level at the fiber output and is difficult to normalize out. Absolute absorption measurements may yet be the best method to determine the crystal fiber doping level. An in-house spectrophotometer is currently being modified to accommodate samples in a fiber form for future measurements.

(d) Discussion

These measurements have failed to give a definite figure for the doping level of the Nd:YAG fibers used in this work, although they seem to indicate that no anomaly exists. The absorption and laser characteristics of Nd:YAG fibers agreed so well with the characteristics of bulk Nd:YAG throughout this work that we believe the compositions of the fibers and of their bulk parents are very similar. We expect that future absorption and mass-spectroscopy analysis will confirm this point.

C. FIBER-RELATED LOSS MECHANISMS

1. Evidence of Aperturing

Several types of waveguide imperfections may be responsible for a loss increase in fiber lasers. The first one, mentioned earlier in this report, is surface scattering arising from microscopic ripples on the surface of the fiber. This is expected to become a major effect in smaller diameter fibers in which the signal is guided by the fiber outer surface. A second effect is bulk scattering due to fiber crystal defects of various origins. These two major scattering mechanisms define what we may call a lower-loss path through a given fiber (as we shall see, bulk defects are in general not uniformly distributed within the fiber) surrounded by higher-loss regions. Since these lower-loss regions are smaller than the fiber itself, some degree of signal aperturing occurs which induces signal diffraction and represents a loss mechanism. This aperturing effect also provides mode confinement, as described earlier (see SECTION IV-B).

Our experimental results clearly indicate that signal aperturing was present in all the fiber lasers tested under this program. The following arguments support this statement.

(1) All fiber laser cavities were made of a flat-flat mirror configuration, which is essentially an unstable resonator. In this type of resonator, signal confinement is generally provided by the finite transverse size of the optics. In our case it had to be provided by the finite transverse dimension of the gain medium, i.e., of the Nd:YAG fibers.

(2) In all fiber lasers, and even in the largest diameter fibers, a strong mode confinement was observed. The mode size was always smaller than predicted on the grounds of total internal reflection (TIR) at the fiber/epoxy interface alone.

(3) As the aspect ratio of the fiber is increased, aperturing of the signal in the cavity becomes stronger. The signal becomes more strongly aware of the fiber surface, near the fiber ends at first, then towards the center of the fiber, and signal loss due to fiber surface imperfections increases. This interpretation is consistent with our experimental measurements, as shown in Figure 42 where the measured round-trip loss of a few fiber lasers was plotted versus their aspect ratio ($\lambda_p = 514.5$ nm). The lowest loss fibers were ~ 250 μ m in diameter and 4 mm long (aspect ratio of 16). The highest losses were observed in ~ 80 μ m in diameter, 12 mm long fibers (aspect ratio of 150).

(4) Conversely, as the fiber diameter was reduced the fiber gain per unit pump power was observed to increase, which also reflects a stronger mode confinement.

(5) In the Nd:YAG fiber lasers developed at BTL a few years ago, signal aperturing (and signal guidance) was deliberately avoided by using (i) curved mirrors with radii of curvature on the order of a few fiber lengths (a few centimeters), and (ii) small aspect ratios (≤ 100) (Reference 5).

(6) Signal aperturing or guiding also explains why higher order transverse modes were never observed in our fiber lasers, even when pumped several times above threshold, whereas they were easily obtained in bulk lasers. Just like in other types of lasers, mode discrimination occurs in fiber lasers as a result of differential modal loss introduced by signal aperturing. Note that in the unguided fiber lasers developed at BTL, higher order modes were observed by misaligning the optical cavity (Reference 5).

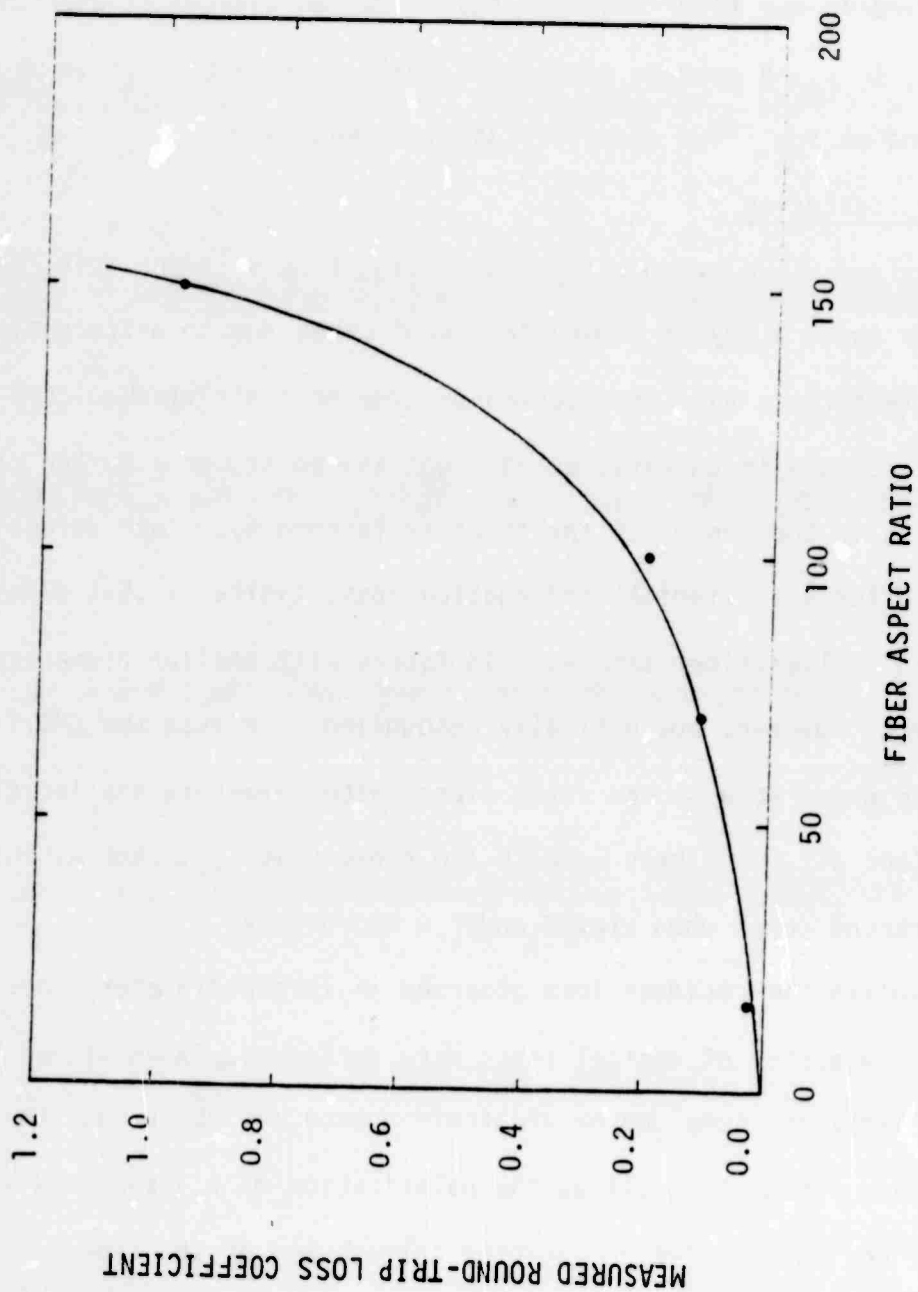


Figure 42--Experimental Evidence of the Cavity Loss Increase with Fiber Aspect Ratio in 514.5 nm pumped Fiber Lasers.

(7) Fibers are expected to exhibit different levels of scattering, which explains why the characteristics of fiber lasers in a given array were observed to vary from fiber to fiber.

For these reasons we strongly believe that signal diffraction (or scattering) due to aperturing is responsible for a major part of the residual loss observed in our fiber lasers. Again the two classes of aperturing mechanisms, bulk and surface scattering, have different relative magnitudes which depend on the fiber diameter, as discussed below.

2. Fiber Scattering

Burrus and Stone noted early that Nd:YAG fibers larger than 250 μm grown faster than about 5 mm/min showed "cracked" cores due to differential thermal expansion (Reference 4). Observation of some of their cracked-core samples under a microscope in back-reflected light indeed showed a darker region of core defects in the center of the fiber (Reference 6). Such defects were responsible for a substantial propagation loss, typically .5-1 dB/cm as measured in earlier fiber samples. In fibers with smaller diameters such defects were, however, not optically recognized. Because the CMR fibers are customarily grown at a slower rate, fibers with diameters smaller than $\sim 300 \mu\text{m}$ (and all the fibers used in the present work) do not exhibit any visible cracked cores when viewed under a microscope.

To explain the residual loss observed in larger diameter fiber lasers (array #2), a number of optical tests were performed. When viewed between crossed polarizers, some degree of birefringence was observed. This birefringence was quite small as the polarization of a laser beam was essentially unaltered after propagation through any of the fibers. Direct measurements of the transmission loss of these fibers were also performed.

Such apparently simple measurements are in fact relatively inaccurate, as they involve the detection of small losses and are easily influenced by other parameters such as the state of the fiber end and the exact Fresnel loss at each fiber end, which is not always accurately known. However, they indicate a typical fiber excess loss of a few percent for fibers of array #2. This loss increases with wavelength, as expected for a scattering phenomenon.

By shining a visible laser through a given fiber and projecting a magnified image of the fiber end on a screen, we found more recently that the focused laser beam, approximately 50 μm in diameter, would not propagate uniformly through the fiber. The fibers appeared to be cracked at several places varying from fiber to fiber, so that in most of them the beam could propagate with little loss only through a single area of the fiber. At the present time we are unable to provide a definite explanation for the sequence of events that led to this condition. Inspection of other fiber arrays showed similar defects in other fibers, although most of them exhibited a clear "window". By polishing a fiber array (array #16) several hundreds of microns below its initial surface and periodically inspecting its surface, it was found that some of the bulk defects are located near the polished surface. These defects may therefore occur during the fiber end processing, possibly when the fibers are cut prior to mounting or prior to polishing. This operation is normally done with a diamond saw, which may induce cracks in the fiber near the cut. This hypothesis is currently being checked by polishing and inspecting additional arrays.

D. SUMMARY

The conclusion of these observations is that of all the loss mechanisms possibly involved in fiber lasers, the dominant one is signal aperturing. Aperturing is caused by residual bulk defects in larger diameter fibers, possibly caused by fiber processing. In smaller diameter fibers it is caused by the fiber surface itself, whose surface irregularities scatter the signal into higher order modes and radiation modes. This result emphasizes again the importance of controlling the diameter of crystal fibers at growth, as well as preserving their crystal quality throughout the processing operations.

SECTION VII

CONCLUSIONS

Under this contract significant progress was made on the development of Nd:YAG single crystal fiber lasers with a high degree of optical confinement. To the best of our knowledge it provides the first demonstration of such lasers in a guided form. Using in-house grown fibers, it led to the operation of state-of-the-art cw fiber lasers with a maximum output of nearly 10 mW at 1.064 μm in a fundamental and linearly polarized mode. It also showed that Nd:YAG lasers pumped with laser diodes at ~ 820 nm can exhibit energy conversion efficiencies in excess of 60%. As expected, the pump-to-fiber coupling efficiency was improved by using a laser diode as a pump source instead of an LED, and further improvements are anticipated.

The excellent pointing stability and mode quality of these fiber lasers make them particularly attractive for single mode fiber applications. We believe this work has helped to pave the way to the development of a large number of other crystal fiber devices made of materials intrinsically less efficient than Nd:YAG, which should greatly benefit from a guided fiber geometry.

To take full advantage of the guiding properties of a fiber configuration, signal confinement must be provided by a mechanism stronger than spatial diffraction. In particular, if total internal reflection is to be the main guiding mechanism, fibers with large aspect ratios should be used. This work made a significant contribution in this direction, pointing out in particular the importance and means of reducing signal propagation loss in crystal fibers.

Future work on single crystal fiber devices will concentrate on the reduction of scattering loss in fibers. The development of clad crystal fibers, now well underway, should yield significant progress in this direction. Also, an improved growth station, in development at the Ginzton Laboratory at Stanford University for the last 18 months, is now available for routine crystal fiber growth.⁽⁸⁾ Preliminary results indicate excellent fiber diameter control, on the order of 1% or better, and considerable loss reduction is anticipated. Future efforts will also address (1) the optimization of the optical coupling between laser diode beams and optical fibers; (2) the correction of the astigmatism of LD-beams; (3) further miniaturization of fiber lasers; and (4) further crystal fiber diameter reduction, now in progress with the recent demonstration of state-of-the-art 15 μm Nd:YAG fibers. These efforts are expected to soon yield improved laser performance and to promote the study of new types of cw and pulsed fiber lasers as well as other fiber devices.

APPENDIX A

EXPANSION OF THE OVERLAP INTEGRAL $J_1(S_1)$

For simplicity the overlap integral [Eq. (10)] may be written in the condensed form

$$J_1 = \int \frac{r_0 s_0}{1 + A s_0} dv \quad (A-1)$$

where $A = c\tau_f S_1/n_1$ is the normalized signal photon density, and is proportional to the laser output power.

Near threshold $A \sim 0$ an expansion of the denominator of Eq. (A-1) yields

$$\frac{1}{J_1} \approx \frac{1}{J_0} + \frac{A}{J_0^2} \int r_0 s_0^2 dv \quad (A-2)$$

where $J_0 = J_1(A = 0)$ is the modal overlap integral at threshold. Therefore the quantity $(1/J_1 - 1/J_0)$ grows linearly with A .

Far above threshold ($A \rightarrow \infty$) we can expand the denominator of J_1 [Eq. (A-1)] in a series of $1/As_0$ terms. Since the mode distribution s_0 necessarily has zeros the quantity As_0 vanishes at places across the laser section, and this expansion may not be legitimate. However in the regions where the expansion validity breaks down the numerator of J_1 also vanishes. The contribution of such regions to the integral is negligible, and the expansion is actually quite accurate. A straightforward calculation leads to

$$\frac{1}{J_1} = \frac{I_2}{\eta_p} + \frac{A}{\eta_p} . \quad (A-3)$$

Here I_2 is an overlap integral involving only the mode profiles r_0 and s_0 , while η_p is the fraction of pump power carried by the active region [Eq. (24)]. Again $1/J_1$ grows linearly with A .

Consequently, both near and far from threshold derivations lead to the same A -dependence. Near threshold the dominant term is $1/J_0$ [Eq. (A-2)], while far above threshold it is A/η_p [Eq. (A-3)]. In the general case the overlap integral [Eq. (A-1)] may therefore be written as

$$\frac{1}{J_1} \approx \frac{1}{J_0} + \frac{A}{\eta_p} . \quad (A-4)$$

Comparison with the exact form of J_1 for typical examples shows that higher order terms in A are actually negligible (see Sections III-C and III-D) and Eq. (A-4) is accurate in most practical situations.

APPENDIX B

CALCULATION OF GAUSSIAN MODE SPATIAL OVERLAP INTEGRALS

In cylindrical coordinates (r, ϕ, z) with the z -axis along the fiber axis, the normalized distribution function of the fundamental Gaussian mode (TEM_{00}) is (for the signal)

$$s_{00}(r, z) = \kappa_s e^{-2r^2/W_s^2} \quad (B-1)$$

where W_s is the mode waist radius (function of z) and κ_s a normalization constant such that s_{00} is normalized to unity over the cavity volume

$$\kappa_s = \frac{2}{\pi l W_s^2} \quad (B-2)$$

where l is the length of the cavity.

Similarly, for the pump the distribution is taken in the form

$$r_0(x, y, z) = r_p e^{-\alpha_a z} e^{-2r^2/W_p^2} \quad (B-3)$$

for an end-pumped laser. α_a is the absorption coefficient of the laser material at the pump wavelength λ_p . Normalization of $r_0(x, y, z)$ to unity gives

$$\kappa_p = \frac{2}{\pi W_p^2} \cdot \frac{\alpha_a}{(1 - e^{-\alpha_a l})} \quad (B-4)$$

Evaluation of the filling factor F_{0000} requires the computation of $J_1(0)$ [Eq. (12)] using r_0 and s_0 defined above. A straightforward calculation yields

$$J_1(0) = \frac{2}{\pi l (\bar{W}_S^2 + \bar{W}_P^2)} \quad (B-5)$$

where for simplicity W_p and W_s were replaced by their respective average value \bar{W}_p and \bar{W}_s (averaged along the crystal length).

For F_{0100} , the signal mode involved is TEM_{01} , described by

$$s_{01}(r, \phi) = \frac{8r^2}{\pi l W_s^4} \cos^2 \phi e^{-2r^2/W_s^2} \quad (B-6)$$

Computation of the filling factor using Eqs. (B-3), (B-6), and κ is again straightforward and yields

$$J_1(0) = \frac{2}{\pi l} \frac{\bar{W}_P^2}{(\bar{W}_P^2 + \bar{W}_S^2)^2} \quad (B-7)$$

APPENDIX C

LP_{nm} FIBER MODES

Since the fiber numerical aperture is assumed to be small, the fiber modes are taken to be of the LP-type, described for example by Marcuse (Reference 11). In an (x,y,z) orthogonal coordinate system whose z-axis points along the fiber axis, the optical field of an LP-mode is either x- or y-polarized. Each set of modes (x- or y-polarized) has nonvanishing components [(E_x,H_y) or (E_y,H_x)] which are described analytically by a set of two expressions, valid in the core and in the cladding respectively, and involving Bessel functions (Reference 11). For the purpose of evaluating modal overlap integrals only the mode power density is required, given by

$$s_{\nu\mu}(r,\phi) = \frac{1}{2} E_{x_{\nu,\mu}} H_{y_{\nu,\mu}}^* \quad (C-1)$$

It can be easily shown that the mode power density is the same for the x- and y-polarized LP_{νμ} modes, and can be expressed analytically as

$$s_{\nu\mu}(r,\phi) = \begin{cases} c_{\nu\mu} J_{\nu}^2(\kappa r) \begin{matrix} \cos^2 \nu\phi \\ \sin^2 \nu\phi \end{matrix} & \text{for } r < a \end{cases} \quad (C-2a)$$

$$\begin{cases} c_{\nu\mu} \frac{J_{\nu}^2(\kappa a)}{\kappa_{\nu}^2(\gamma a)} \kappa_{\nu}^2(\gamma r) \begin{matrix} \cos^2 \nu\phi \\ \sin^2 \nu\phi \end{matrix} & \text{for } r > a \end{cases} \quad (C-2b)$$

where a is the fiber core radius, γ , κ and β the transverse and longitudinal propagation constants, J_{ν} the Bessel function of order ν , K_{ν}

the modified Bessel function, and $c_{\nu\mu}$ a normalization constant such that the power P carried by each mode is a constant. Note that each $LP_{\nu\mu}$ mode (except $\nu = 0$) can have either a cosine or sine azimuthal angle dependence.

In the present work, the power density is normalized to the cavity volume rather than its cross section as is more customarily done. Any z -dependence of $s_{\nu\mu}$ must therefore be included to compute $c_{\nu\mu}$. For simplicity we assume the single-pass gain is small, so that the signal intensity is practically constant along the fiber length. This assumption could be avoided by introducing the exact z -dependence of the signal, but it can be shown that it only slightly changes the result while considerably complicating calculations. With this approximation the signal normalization coefficient is

$$c_{\nu\mu} = \frac{2\gamma_s^2}{k \pi e_\nu V_s^2} \frac{1}{|J_{\nu-1}(\kappa_s a) J_{\nu+1}(\kappa_s a)|} \quad (C-3)$$

where the s -subscript refers to signal quantities, V_s is the fiber V-number at the signal wavelength [Eq. (40)], and e_ν is a coefficient resulting from the azimuthal integration, equal to

$$e_\nu = \begin{cases} 2 & \text{for } \nu = 0 \\ 1 & \text{for } \nu \neq 0 \end{cases} \quad (C-4)$$

In an end-pumping configuration the pump power is expected to be relatively strongly absorbed as it travels down the fiber, so that the pump power density shows a non-negligible z -dependence. Calling α_a the absorption coefficient of the laser material at λ_p , the pump power density

is given by

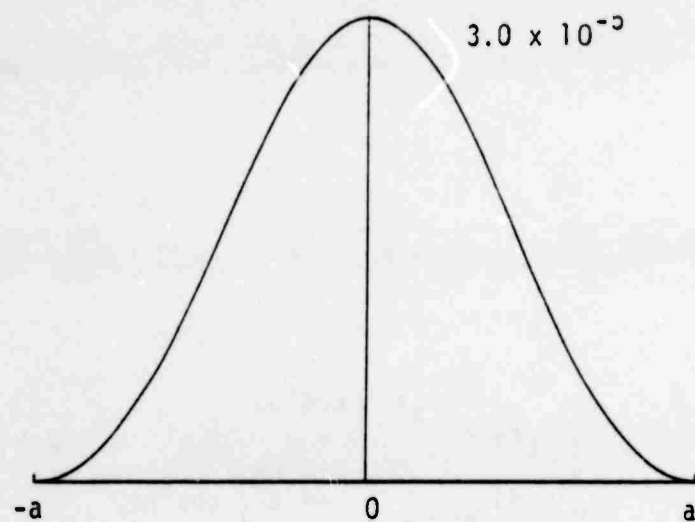
$$r_{nm}(r, \phi, z) = \begin{cases} c_{nm} J_n^2(\kappa_p r) e^{-\alpha_a z} \begin{cases} \cos^2 n\phi \\ \sin^2 n\phi \end{cases} & r < a \\ c_{nm} \frac{J_n^2(\kappa_p a)}{K_n^2(\gamma_p a)} K_n^2(\gamma_p r) e^{-\alpha_a z} \begin{cases} \cos^2 n\phi \\ \sin^2 n\phi \end{cases} & r > a \end{cases} \quad \begin{matrix} (C-5a) \\ (C-5b) \end{matrix}$$

The normalization constant is now

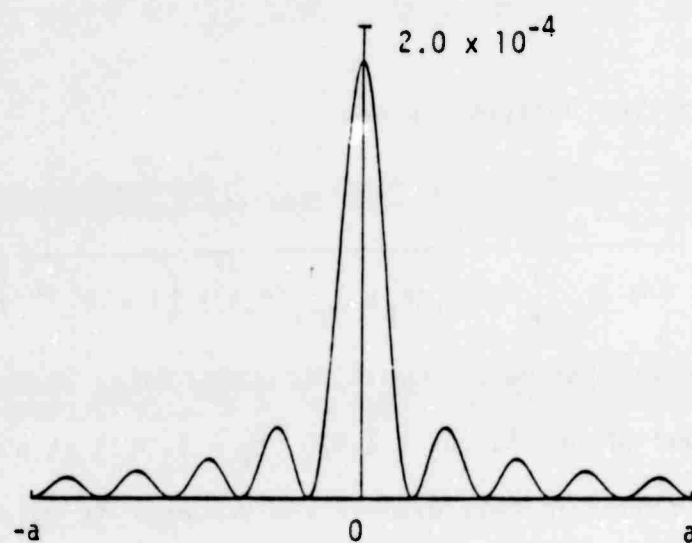
$$c_{nm} = \frac{2\gamma_p^2}{\pi e_n V_p^2} \frac{1}{|J_{n-1}(\kappa_p a) J_{n+1}(\kappa_p a)|} \frac{\kappa_a}{\left(1 - e^{-\alpha_a L}\right)} \quad (C-6)$$

We show in Figure C-1 the power density of a few fiber modes in a 50 μm diameter core fiber of Nd:YAG ($n_1 = 1.820$, $n_2 = 1.815$) at a signal wavelength of 1.064 μm . Note that in this example the V-number is relatively large (~ 40), the fiber can support a large number of modes (approximately $V^2/2 = 800$) (Reference 16), and the low order mode distributions are essentially independent of the signal wavelength.

LP₀₁



LP₀₅



LP_{0,30}

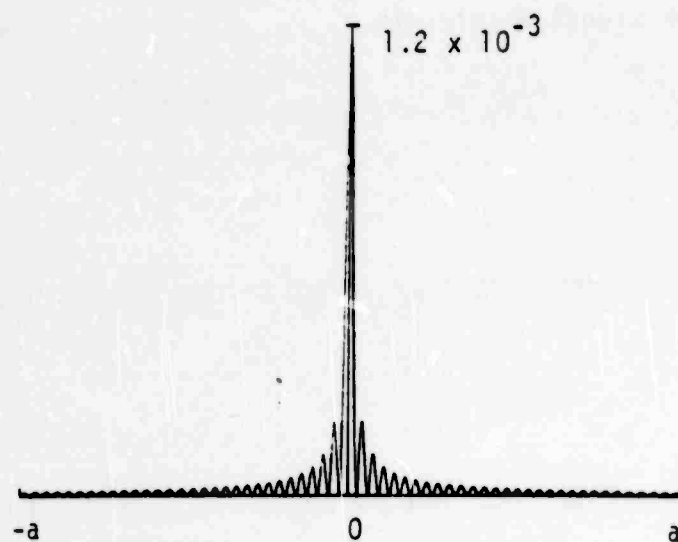


Figure C.1--Intensity Radial Profiles of a Few LP-Modes (Far from Cut-Off).

APPENDIX D

EFFECT OF A RELATIVE PUMP OFFSET IN FIBER LASERS

We consider an end-pumped laser in which the pump and signal mode axis are either offset or tilted relative to each other, and aim at an estimate of the quantitative effect (and maximum tolerances) of such misalignments on the laser output power characteristics.

1. Mode Alignment

For simplicity we only consider the most relevant case of single fundamental mode laser operation and fundamental pump mode. A lateral offset Δ , possibly a function of the position z along the active medium, is assumed for the pump mode. The power densities of the signal and pump modes are respectively taken in the form

$$s(x,y,z) = \kappa_s \exp \left(-2 \frac{(x^2 + y^2)}{w_s^2} \right) \quad (D-1)$$

$$r_0(x,y,z) = \kappa_p \exp \left(-2 \frac{(x - \Delta)^2 + y^2}{w_p^2} \right) \quad (D-2)$$

where κ_s and κ_p are normalization constants and w_s and w_p are the signal and pump mode waist, respectively. It is understood that in the following these waists are to be replaced (1) by their respective average values (\bar{w}_s and \bar{w}_p) calculated along the length of the active medium whenever the modes diffract significantly within the interaction region, (2) by the mode waists in the case one of the modes is guided (the Gaussian approximation is then quite accurate).

2. Effect on the Threshold

To calculate the theoretical threshold we must evaluate the simple mode overlap $J_1(0)$ (see Eq. (12)). After a straightforward and exact calculation we find that the effective pump mode area is

$$A_p^* = \frac{\pi(w_p^2 + w_s^2)}{2} e^{+ 2 \Delta^2 / (w_p^2 + w_s^2)} \quad (D-3)$$

As expected, in the absence of offset ($\Delta = 0$) this result is identical to our earlier result. The effect of an offset may be better understood by writing Eq. (D-3) in terms of a relative variation of threshold:

$$\frac{\Delta P_{th}}{P_{th}} = e^{+ 2 \frac{1}{(\alpha + 1)} \left(\frac{\Delta}{w_p} \right)^2} - 1 \quad (D-4)$$

where $\alpha = (w_s/w_p)^2$ as defined earlier. This increase in laser threshold is plotted versus offset for a few values of α in Figure D-1. It shows that in practical situations ($\alpha \approx 1/2 - 2$), a (constant) offset of half a pump waist radius ($\Delta/w_p = 50\%$) results in a threshold increase of about 25%. For a typical pump waist of 20 μm , this result indicates an offset tolerance of 10 μm . The threshold should therefore not be too critically dependent on a constant offset (independent of z).

Solving the exact problem of an angular tilt between the two beams is difficult. The offset Δ is then a function of z , and integration of the overlap integral is complicated by the presence of a Gaussian term in z . As a convenient approximation we shall assume an offset in the form

$$\Delta = \theta z \quad (D-5)$$

where θ is the relative angle between the mode axes, and replace Δ in Eq. (D-4) by its average value $\theta l/2$, where l is the active medium length. This approximation is valid when the gain (dependence $e^{-\alpha_a z}$) does not vary much across the gaussian term, i.e. when the tilt angle is larger than

$$\theta > \theta_0 = \sqrt{2} \frac{W_p}{\alpha_a} \quad (D-6)$$

which, for a typical W_p of 20 μm and absorption coefficient $\alpha_a \approx .6 \text{ cm}^{-1}$, equals $\theta_0 \approx 5 \text{ mrd}$. For angles smaller than θ_0 the overlap depends very little on θ . With this approximation we find that

$$\frac{\Delta P_{th}}{P_{th}} = e^{\frac{1}{2(1+\alpha)} \left(\frac{\theta l}{W_p} \right)^2} - 1 \quad (D-7)$$

This dependence is shown in Figure D-1 for $W_p = 20 \text{ microns}$ and $l = 4 \text{ mm}$. The right side of the plots ($\theta \geq 5 \text{ mrd}$) is more accurate, while the $\theta < 5 \text{ mrd}$ region is probably accurate within a factor of two. Although a constant offset does not significantly spoil the laser threshold, a tilt

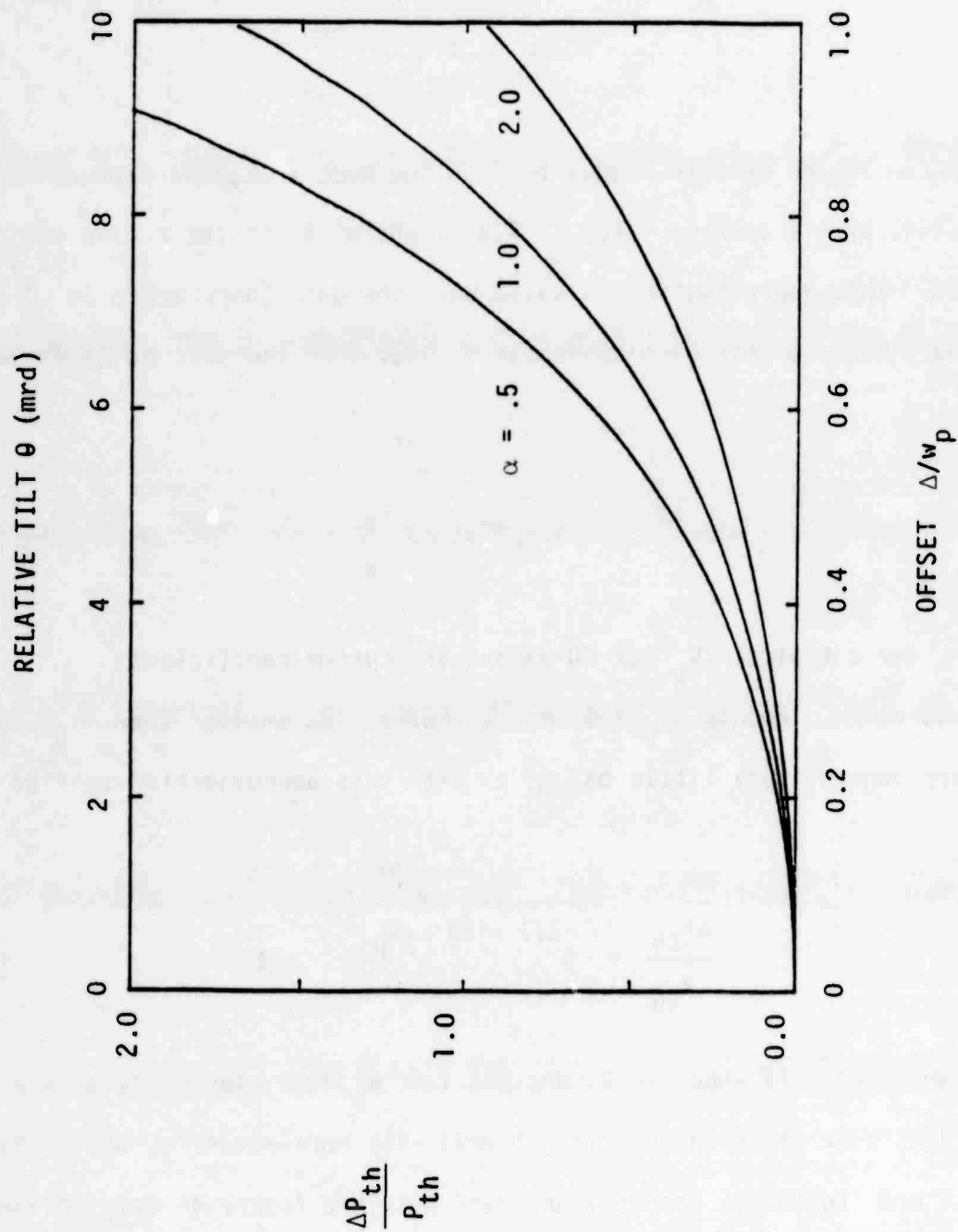


Figure D.1--Effect of an Offset on a Tilt between Pump and Signal Modes on the Laser Threshold.

induces a relatively large threshold increase. A misalignment of .5 degree results in most practical cases in a 100% increase in the threshold. We believe this figure is relatively exact (to within 20%) despite the approximation made. The tolerance on the beam angular alignment is therefore quite tight, and a 1/2 degree angle seems to be the upper limit of tolerable misalignment. This requirement can be quite drastic when using non-guiding lasers.

3. Effect on the Slope Efficiency

To estimate the effect of a relative offset on the laser slope efficiency the second type of overlap integral, which involves a saturation term, must be evaluated. Since it now involves a denominator to account for signal saturation, the integral cannot be solved in a closed form. On the other hand, the use of a computer would be rather lengthy. To derive an order-of-magnitude estimate of this integral we assume that the offset Δ/W_p is large. We can then expand the denominator to first order. This approximation is necessary only far above threshold. Near threshold the following holds for any value of Δ . The overlap integral can then be calculated, and the laser slope efficiency is found to be

$$s = \frac{T_1}{\phi_0} \frac{h\nu_s}{h\nu_p} g_\alpha(\Delta) \quad (D-8)$$

where $g_\alpha(\Delta)$ is the offset function

$$g_\alpha(\Delta) = \frac{\alpha(\alpha + 2)}{(\alpha + 1)^2} e^{-\frac{4}{(\alpha + 1)(\alpha + 2)} \left(\frac{\Delta}{W_p}\right)^2} \quad (D-9)$$

The slope efficiency is proportional to $s_0 = (T_1/\delta_0)(h\nu_s/h\nu_p)$, as found earlier. Note that this result only applies to large Δ , and that for $\Delta = 0$ $g_\alpha(0)$ is not unity as would be expected. However, in the far-from-threshold limit it is easy to show that the slope efficiency is independent of Δ . Thus, far above threshold, $s = s_0$. We can therefore extend the definition of $g_\alpha(\Delta)$ to

$$g_\alpha(\Delta) = \begin{cases} 1 & \text{for } \Delta/W_p \ll 1 \\ \frac{\alpha(\alpha + 2)}{(\alpha + 1)^2} \exp \left\{ - \frac{4}{(\alpha + 1)(\alpha + 2)} \left(\frac{\Delta}{W_p} \right)^2 \right\} & \text{for } \Delta/W_p \gg 1 \end{cases} \quad (\text{D-10})$$

We show in Figure D-2 the normalized slope efficiency s/s_0 versus offset for a few values of α . Solid curves are computed from Eq. (D-9). Dashed curves are extrapolated to the small-offset region. In a typical situation ($\alpha \approx 1$) the efficiency is reduced by 20% for an offset of $\Delta/W_p = 50\%$.

Again the influence of a tilt may be estimated by replacing in Eq. (D-9) the offset Δ by its average value $\theta \ell/2$. The resulting dependence is shown in Figure D-3 for $W_p = 20 \mu\text{m}$ and $\ell = 4 \text{ mm}$. Again the tolerance on angle is rather tight. A tilt angle of 10 mrd ($.6^\circ$) reduces the slope

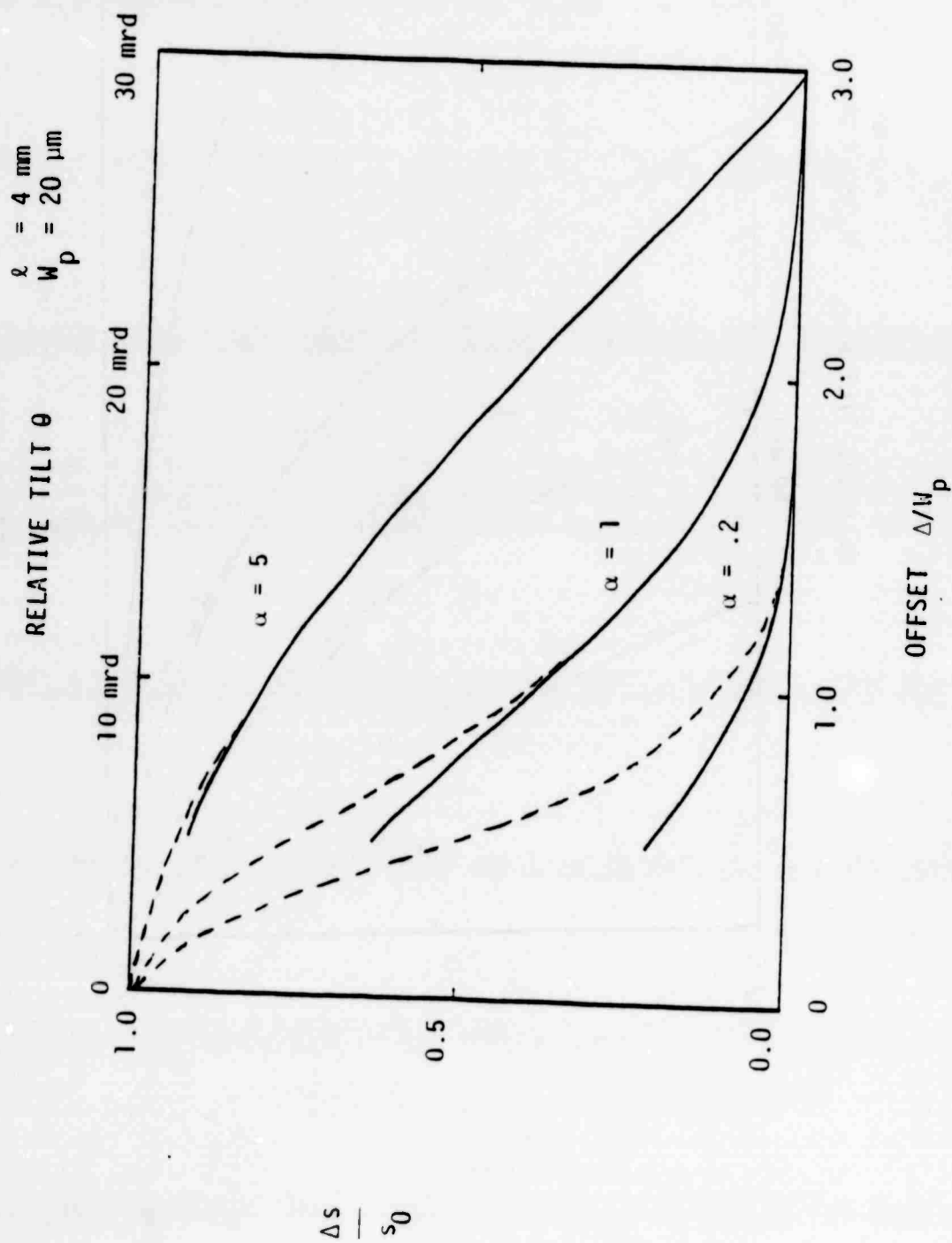


Figure D.2--Effect of an Offset or a Tilt between Pump and Signal Beam on the Laser Slope Efficiency.

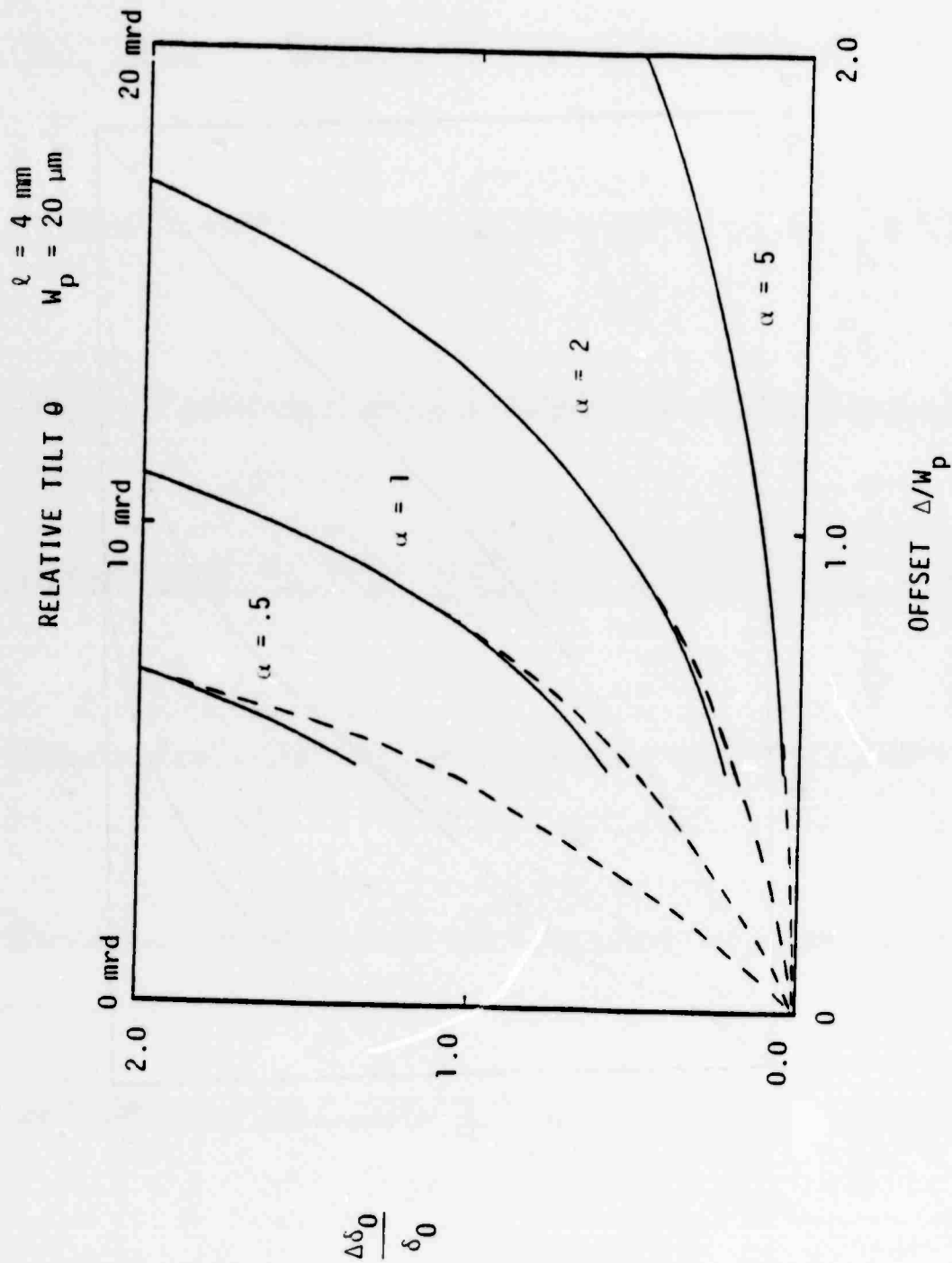


Figure D.3--Effect of an Offset or Tilt between Pump and Signal Beam on the Measured Cavity Round-Trip Loss.

efficiency by a factor of two. Although this result may be pessimistic by as much as a factor of two, it shows that alignment is critical for the laser efficiency. A 1/2 degree angle seems to be again the tolerable upper limit.

Since in practice the measurement of the slope efficiency of this type of laser is the most accurate way to obtain the cavity round trip loss δ_0 , we show in Figure D-3 the error $\Delta\delta_0/\delta_0$ in loss estimation due to an offset or a tilt (again for $W_p = 20 \mu\text{m}$, $z = 4 \text{ mm}$). In other words, the apparent cavity loss indicated by the slope efficiency measurement will be $\delta_0 + \Delta\delta_0$. Again we find the error to be critically influenced by an angular misalignment. Typically, an added loss $\Delta\delta_0/\delta_0$ of 50% is expected with an angle error of 6 mrad ($.3^\circ$). The estimated loss is wrong by a factor of two for an angle of 1/2 degree.

APPENDIX E

GUIDING MECHANISMS IN FIBER LASERS

We present here a brief summary of the possible guiding mechanisms present in a fiber laser and the magnitude of their respective effects in terms of a real or equivalent index gradient Δn .

1. Cladding

The core/cladding interface can provide a guiding effect if $n_1 > n_2$, where subscripts 1 and 2 refer to core and cladding respectively. This condition is currently satisfied, with $n_1 = 1.816$ and $n_2 \approx 1.5$ (epoxy). This guiding mechanism can be by far the strongest one, as it can readily provide a significant index gradient. Again, in order to reduce the scattering effect of the core surface defects, this gradient can be lowered to any desirable level by a proper choice of cladding material.

2. Index Gradient

An index gradient may exist across the fiber cross section, as a result of a gradient of impurity concentration occurring during the growth and cooling of the fiber. In the case of Nd:YAG fibers, the concentration of Nd^{3+} is expected to be higher on the fiber axis than on the fiber edge. In 1 at.% Nd doped YAG, the index of refraction at $1.064 \mu\text{m}$ is 1.1×10^{-3} larger than in undoped YAG. Insofar as our fibers are approximately 1% doped, this figure is also the maximum possible index change. Measurements of index profiles should determine the magnitude of the gradient.

3. Gain-Guiding Effect

The presence of a gain spatial profile in the laser suggests the possibility of gain-guided modes. We show in Figure E-1 typical profiles in a 50 μm core radius Nd:YAG fiber ($n_1 - n_2 = 5 \times 10^{-3}$) pumped with, and oscillating on, LP_{01} modes. The n -parameter is the number of times above threshold the laser is running. $G(r)$ is the gain per unit length, averaged along the fiber length and normalized to the loss per unit length. At threshold ($n = 0$) the gain profile is the same as the pump profile. Above threshold saturation flattens the gain profile, which rapidly converges to an asymptotic rectangular shape as $n \rightarrow \infty$.

Near threshold the near-quadratic gain radial distribution makes it convenient to use the standard results of quadratic gain media. It is possible to show that the waist W of the gain-guided mode in such medium is given by

$$\frac{W}{a} = \left(\frac{4.42 \lambda}{\gamma_0 n^2 a^2} \right)^{1/4} \quad (\text{E-1})$$

where a is the fiber core radius (active part), n its refractive index, and γ_0 the unsaturated gain per unit length at linecenter. We can define an equivalent index gradient Δn by comparing this situation with the case of a step-index fiber with $V = 2\pi a / \lambda \sqrt{2n\Delta n}$, for which, in the limit of moderately large V ,

$$\frac{W}{a} \approx .64 + \frac{1.55}{\sqrt{3/2}} \quad (\text{E-2})$$

which yields a complex but useful relation between Δn and γ_0 .

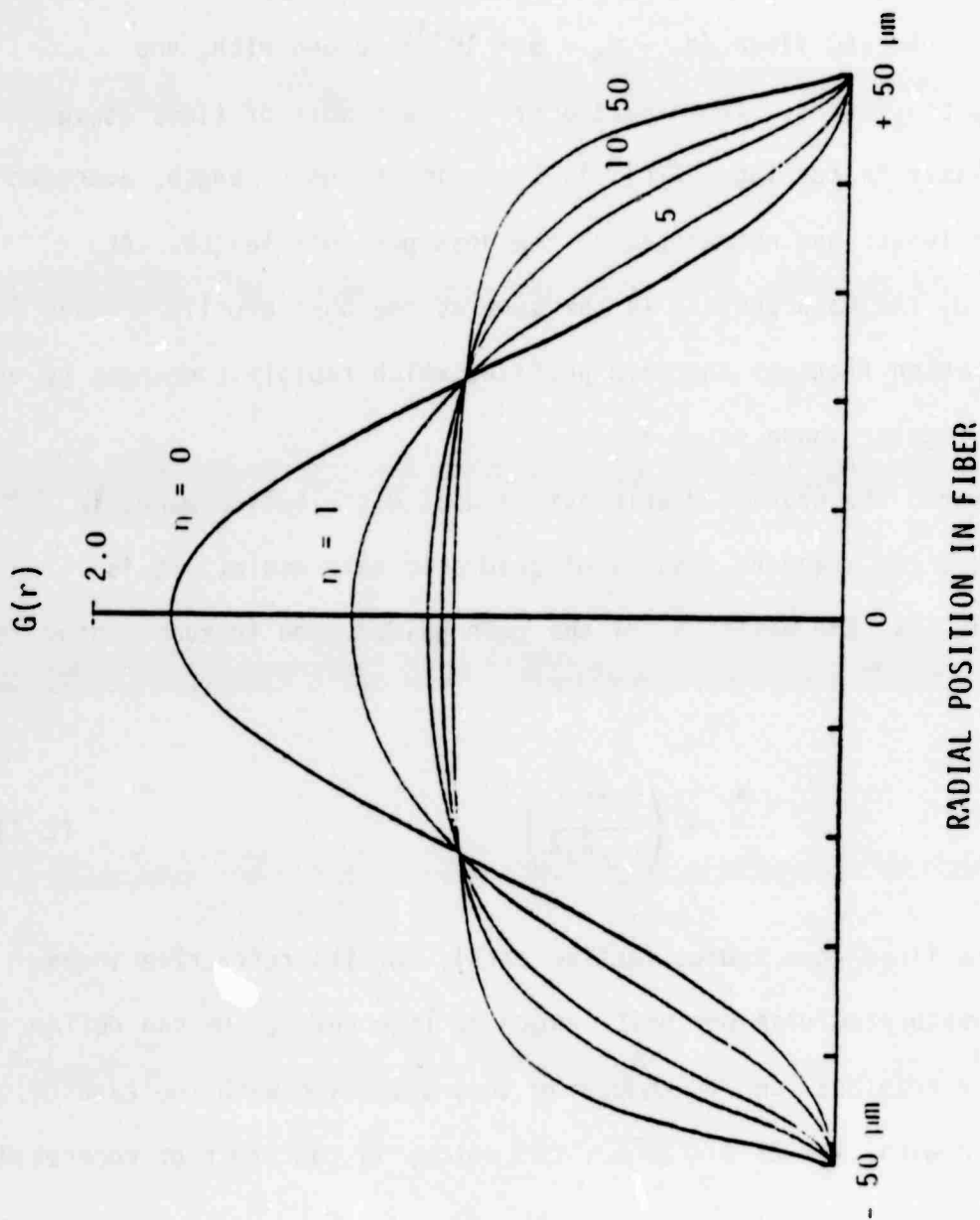


Figure E.1--Normalized Gain Profile in a Nd:YAG Fiber Laser at increasing Levels of Saturation (η_1 = Number of Times above Threshold). Fiber Parameters are $a = 50 \mu\text{m}$, $\eta_1 - \eta_2 = 0.005$ (LP₀₁ Pump and Signal Modes).

Applying this result to our fiber lasers, which have a gain of approximately $\gamma_0 = .1 \text{ cm}^{-1}$ at threshold, and $a \approx 50 \text{ } \mu\text{m}$, we find $W/a = 2.75$, which indicates a very weak guiding effect. The equivalent Δn computed from (E-1) and (E-2) is $\sim 2 \times 10^{-6}$.

Above threshold the quadratic component of the gain profile decreases (see Figure E-1). However, since the overall gain profile doesn't change significantly (only a reduction of the on-axis gain by a factor of 2) Eq. (E-1) is probably still valid provided γ_0 is replaced by the saturated gain. Since W/a varies as $\gamma_0^{-1/4}$, the resulting correction factor is thus negligible ($\leq 20\%$) and the above result probably holds to a good approximation.

4. $\chi'(\nu)$ -guidance

Associated with the gain lineshape $\chi''(\nu)$ (imaginary part of the susceptibility $\chi(\nu)$) is the real part $\chi'(\nu)$. For a homogeneously-broadened laser $\chi(\nu)$ has a complex Lorentzian distribution $\tilde{g}(\nu)$, whose two components $\chi'(\nu)$ and $\chi''(\nu)$ are shown in Figure E-2. $\chi'(\nu)$ can be related to an index variation $\Delta n(\nu)$ equal to

$$\Delta n(\nu) = \frac{\chi'(\nu)}{2n} \quad (\text{E-3})$$

while χ' and χ'' are also related (Kramers-Kronig relations). It is easy to show that

$$\Delta n(\nu) = \frac{\lambda}{4} \gamma_0 (\nu - \nu_0) g(\nu) \quad (\text{E-4})$$

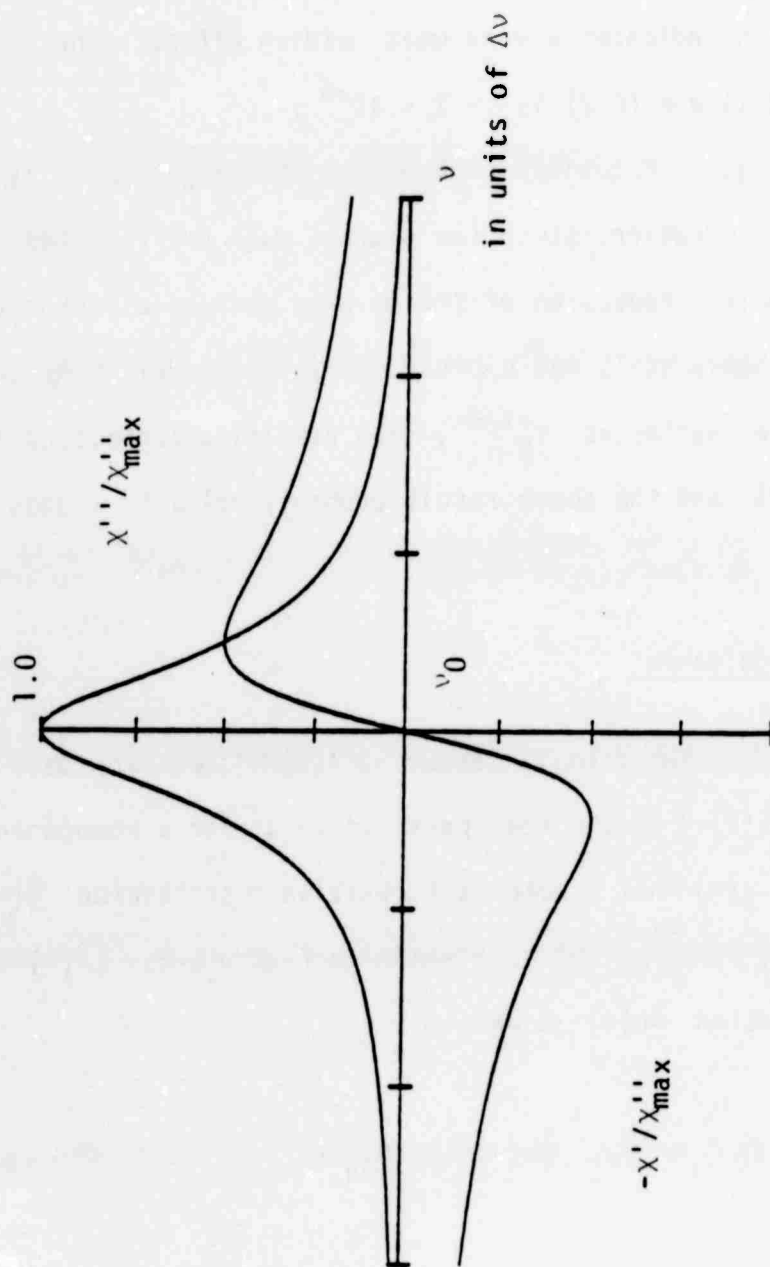


Figure E.2--Plots of the Real and Imaginary Parts of the Susceptibility $\tilde{\chi}(v)$ of a Gain Medium (Unsaturated).

where $g(\nu)$ is the imaginary part of the Lorentzian distribution. From Figure E-2 $\Delta n(\nu)$ takes on optimum values at $\nu = \nu_0 + \Delta\nu/2$ (nonguiding) and $\nu_0 - \Delta\nu/2$ (guiding) which is equal to $\Delta n_{\max} = \gamma_0 \lambda / 8\pi$ (at threshold). Again, using $\gamma_0 = .1 \text{ cm}^{-1}$, one obtains $\Delta n_{\max} \approx 4 \times 10^{-7}$.

This mechanism provides negligible guidance. Also, only the longitudinal mode(s) near $\nu_0 - \Delta\nu/2$ would be guided. With temperature drift the laser output would be expected to be unstable.

5. Thermal Lensing

It has been shown that the temperature gradient $\Delta T(r)$ in a laser rod (or fiber) in which the heat Q is uniformly generated is

$$\Delta T(r) = \frac{Q}{4K} (a^2 - r^2) \quad (\text{E-5})$$

where K is the heat conductivity of the material and Q is related to the dissipated power P_d and the rod dimensions (a and l) by

$$Q = \frac{P_d}{\pi a^2 l} \quad (\text{E-6})$$

In a 50 μm radius, 8 mm long Nd:YAG fiber we find $\Delta T/P_d = .7^\circ\text{C}/\text{watt}$. In a fiber laser with $P_{th} = 5 \text{ mW}$ pumped 30 times above threshold, ΔT is smaller than $.1^\circ\text{C}$.

The effects of this temperature gradient, however small, are two-fold: first, thermal lensing, second, stress-induced birefringence (next section) can exist. The index gradient induced by $\Delta T(r)$, known to provide a guiding action (thermal lensing), is

$$\Delta n_T(r) = - \frac{0}{4K} \left(\frac{dn}{dT} \right) r^2 \quad (E-7)$$

For an 8 mm long Nd:YAG fiber with $P_d = 300 \text{ mW}$, the amplitude of this gradient is about 1.5×10^{-6} .

6. Stress-Induced Birefringence

The temperature gradient existing in a fiber laser generates internal stresses which induce index birefringence. This effect has been quantified, and can be quite large in high-power solid state lasers. However, because the pump power involved in a fiber laser is small, it is negligible in our case. With $P_d = 300 \text{ mW}$ we find that the gradient amplitude induced by thermal stresses is 3.3×10^{-7} .

7. Index Nonlinearity

To first order the index change to nonlinearity is

$$\Delta n_{NL}(r) = \gamma I(r) \quad (E-8)$$

where γ is the nonlinear coefficient of the laser material, and $I(r)$ the total intensity distribution. Using the same parameters as before ($a = 50 \text{ } \mu\text{m}$, $P_p = 300 \text{ mW}$) we find a gradient amplitude of 10^{-9} . This constitutes by far the least significant effect.

8. Summary

We summarize in TABLE E-1 the magnitude of the (real or equivalent) index gradient expected for the above guiding mechanisms, together with some of their basic characteristics. Note that these values were calculated in a worst case of unusually high power levels for fiber devices ($P_p \approx 300 \text{ mW}$).

TABLE E-I
MAGNITUDE OF THE INDEX GRADIENT PROVIDED BY THE GUIDING
MECHANISMS PRESENT IN A HOT FIBER LASER CAVITY
($P_p = 300 \text{ mW}$, $a = 50 \text{ } \mu\text{m}$, $l = 8 \text{ mm}$)

Mechanism	Δn	Intensity Dependent	ν -Dependent
Cladding	0-.8	No	No
Gradient	$< 1.1 \times 10^{-3}$	No	No
Gain Guiding	2×10^{-6}	Somewhat	Yes
χ' Guiding	$< 4 \times 10^{-7}$	Somewhat	Yes
Thermal Lensing	1.5×10^{-6}	Yes	No
Stress Induced	3.3×10^{-7}	Yes	No
Nonlinearity	$\sim 1 \times 10^{-9}$	Yes	No

EFFECT OF PUMP ASTIGMATISM ON LASER CHARACTERISTICS

To qualitatively estimate the effect of the astigmatism in beam dimensions of a pump beam (such as produced by a laser diode) on a fiber laser threshold, we used the results of the Gaussian mode overlap theory presented in SECTION III-C. In the following we call W_{\perp}^0 and W_{\parallel}^0 the waist radii of the laser diode beam at the emitting facet of the junction in directions \perp and \parallel to the junction, respectively. After recollimation and focusing, the beam waist radii are transformed into W_{\perp} and W_{\parallel} , respectively, near the focal plane of lens L_2 (and inside the fiber laser). Since only spherical optics are used, the beam astigmatism $x = W_{\perp}^0/W_{\parallel}^0$ remains uncorrected throughout the beam path, and

$$\frac{W_{\perp}}{W_{\parallel}} = \frac{W_{\perp}^0}{W_{\parallel}^0} = x \quad (\text{F-1})$$

Along the fiber length the two waists vary according to the Gaussian beam diffraction law. Following our earlier results, the average waist radius in each direction along the fiber laser is given by [Eq. (33)]

$$\begin{cases} \langle W_{\parallel}^2 \rangle = W_{\parallel}^2 (1 + \epsilon_{\parallel}) \\ \langle W_{\perp}^2 \rangle = W_{\perp}^2 (1 + \epsilon_{\perp}) \end{cases} \quad (\text{F-2})$$

where ϵ_{\perp} and ϵ_{\parallel} are the diffraction terms

$$\epsilon_{\perp} = \frac{\epsilon_2}{W_{\perp}^2} \quad (F-3)$$

and ϵ_2 a constant of the waist radius

$$\epsilon_2 = \frac{\lambda_{p2}^2 L^2}{3\pi^2 n^2} \quad (F-4)$$

Here L is the fiber length and n the fiber material refractive index. The average pump mode area is therefore

$$A_{p2} = \frac{1}{2} \left(\frac{\pi}{2} \langle W_{\parallel}^2 \rangle + \frac{\pi}{2} \langle W_{\perp}^2 \rangle \right) \quad (F-5)$$

Its minimum value (optimum threshold), computed by letting $dA_{p2}/dW_{\parallel}^2 = 0$ and using Eqs. (F-1) through (F-5), is given by

$$A_{p,2,opt} = \frac{\pi}{2} \sqrt{\epsilon_2} \frac{1+x^2}{x} \quad (F-6)$$

For the circularly symmetric argon beam, we find by letting $x = 1$ and replacing λ_{p2} by λ_{p1} :

$$A_{p,1,opt} = \pi \sqrt{\epsilon_1} \quad (F-7)$$

where ϵ_1 is defined similarly to ϵ_2

$$\epsilon_1 = \frac{\lambda_{p1}^2 L^2}{3\pi^2 n^2} \quad (F-8)$$

Inserting Eqs. (F-6) and (F-7) in $R_{th} = P_{th,1}/P_{th,2}$ [Eq. (54)] we find that

$$R_{th} = \frac{\lambda_{p2}}{\lambda_{p1}} \frac{\left(\bar{w}_s^2 + \frac{\sqrt{\epsilon_1}}{2} \right)}{\left(\bar{w}_s^2 + \sqrt{\epsilon_2} \frac{1+x^2}{x} \right)} \quad (F-9)$$

where \bar{w}_s is the average signal waist radius along the fiber laser.

Equation (F-9) shows that in the absence of astigmatism ($x = 1$), diffraction is stronger for the diode beam than for the argon laser beam ($\lambda_{p2} > \lambda_{p1}$ and $\epsilon_2 > \epsilon_1$) and contributes to lowering the ratio of thresholds R_{th} . Astigmatism ($x \neq 1$) makes matters worse by increasing the minimum achievable beam area. Note that a change in astigmatism direction is not expected to modify the magnitude of this effect. This fact is reflected in the invariance of Eqs. (F-6) or (F-9) under a change of x into $1/x$.

REFERENCES

1. R.A. Bergh et al., "Overview of fiber-optic gyroscopes," J. of Lightwave Technology, to be published.
2. L.F. Stokes et al., "Sensitive all-single-mode-fiber resonant ring interferometer," J. of Lightwave Technology, Vol. LT-1, No. 1, 110-115, March 1983.
3. S.A. Newton et al., "Single mode fiber recirculating delay line," Proceedings of SPIE, Vol. 326, 108-115, January 1982.
4. C.A. Burrus and J. Stone, "Single-crystal fiber optical devices: A Nd:YAG fiber laser," Appl. Phys. Lett., Vol. 26, No. 6, 318-320, March 1975.
5. J. Stone and C.A. Burrus, "Self-contained LED-pumped single-crystal Nd:YAG fiber laser," Fiber and Integrated Optics, Vol. 2, No. 1, 19-46, 1979.
6. M. Digonnet and H.J. Shaw, "Fiber ring laser gyro amplifier," Final Technical Report, No. AFWAL-TR-81-1067.
7. Litton Industries, Inc.
8. M. Fejer et al., "Growth and characterization of single crystal refractory oxide fibers," Proceedings of SPIE, Vol. 320, 50-55, January 1982.
9. Status Report, "Fiber Optics Research Program," Prepared for Litton Systems Inc., by the Edward L. Ginzton Laboratory, Stanford University, Stanford, CA (June 1983).
10. Lens Bond Optical Cement, No. UV-71 or UV-74, Summers Laboratories, Inc, Fort Washington, PA.
11. D. Marcuse in Theory of Dielectric Optical Waveguides, Quantum Electronics, Principles and Applications, (Academic Press, 1974).

12. A.A. Kaminskii in Laser Crystals, Springer Series in Optical Sciences, Vol. 14, 1981.
13. SF57 Schott Glass.
14. Ken'ichi Kubodera and Kenju Otsuka, "Single-transverse-mode $\text{LiNdP}_4\text{O}_{12}$ slab waveguide laser," J. Appl. Phys., Vol. 50, No. 2, 653-659, February 1979.
15. W. Koechner in Solid State Laser Engineering, Springer Series in Optical Sciences, Vol. 1, (Springer-Verlag, 1976).
16. D. Gloge, "Weakly guiding fibers," Appl. Opt., Vol. 10, 2252-2258, October 1971.
17. D. Marcuse, "Gaussian approximation of the fundamental modes of graded-index fibers," J. Opt. Soc. Am., Vol. 68, No. 1, 103-109, January 1978.
18. CVI Laser Corp., Albuquerque, NM.
19. EG&G Powermeter Model 460-1A.
20. D.R. Scifres et al., "High power coupled multiple stripe quantum well injection lasers," Appl. Phys. Lett., Vol. 41, No. 2, 118-120, 15 July 1982.
21. D.R. Scifres et al., "Phase-locked (GaAl)As lasers," IOOC '83, Tokyo, Japan, June 1983.
22. Selfoc lens No. SLW-20-1/4 (high NA) and SLS-20-1/4 (low NA).
23. Technical Digest of Selfoc '82 Conference, Palo Alto, California, May 1982.
24. Gary Sitt, Palo Alto Xerox Research Center, private communication.
25. John Stone, Bell Telephone Laboratories, private communication.
25. H.G. Danielmeyer, in Progress in Nd:YAG Lasers, Laser 4, Levine and De Maria (Marcel Dekker, Inc.).